USING SINGLE VIRION FUSION ASSAY TO STUDY INFLUENZA VIRUS ENTRY

A Dissertation

Presented to the Faculty of the Graduate School

of Cornell University

In Partial Fulfillment of the Requirements for the Degree of

Doctor of Philosophy

by

Hung-Lun Hsu

May 2018

Using single virion fusion assay to study influenza virus entry

Hung-Lun Hsu, Ph. D.

Cornell University [2018]

Understanding the mechanism of influenza virus entry is critical for effectively developing anti-viral drugs and vaccines. The entry of influenza virus is mediated by two proteins: hemagglutinin (HA) and neuraminidase (NA). During virus infection, HA first binds to sialic acid moieties on epithelial cell membranes, triggering engulfment of the virus into the cell via endocytosis. As the endosome matures during trafficking, the pH decreases in the micro-environment, which triggers the conformational change of HA that induces membrane fusion of the viral and endosomal membranes. Fusion allows the virus to release viral RNA into the cytosol of the cell. Single particle tracking (SPT) enables the study of viral binding and membrane fusion at the single-virion level to obtain high resolution measurements of each of these processes *in vitro*. SPT combines total internal reflection fluorescence (TIRF) microscopy with microfluidics and supported lipid bilayers, making it a very powerful tool for host-pathogen membrane fusion studies.

One concern about influenza is that the virus can mutate quickly via three mechanisms (i.e. error-prone RNA replication, influenza reassortment, and influenza recombination). Influenza virus mutation mechanisms may cause the emergence of new strains, some of which may lead to serious flu pandemics in humans. Understanding the fusion fitness of influenza strains at the single-virion level is crucial for the development of anti-viral fusion drugs which block genome transfer. However, high risk live influenza pandemic strains can be infectious and lethal to humans, which makes them a challenge to study in the laboratory environment

without significant safety protocols in place. To study the influenza pandemic virus, using a pseudovirus is the most common surrogate system for studying virus entry. However, before this work, no studies directly compared the entry processes of pseudoviruses with their wildtype particles. Here I use SPT to compare the fusion kinetics of influenza native virus and its pseudovirus analog and show that these particles do recapitulate the native behavior well. I will then show how I use pseudoviruses to mimic influenza reassortment and shed light on how influenza reassortment can infect virus entry. Next, I report results on SPT studies of virus entry of influenza virus H10N8 (JX346), a virus of concern because, although there have been only 3 confirmed cases, it was transmitted directly from chicken to human in 2014, with high lethality. Lastly, I will expand the SPT technique to study the inhibitory mechanism of an influenza antiviral drug, IFITM3. IFITM3 has been shown to be able to stop influenza virus entry at the fusion step, and lead to the failure of infection.

BIOGRAPHICAL SKETCH

Hung-Lun Hsu was born in Taipei, Taiwan to Li-Cheung Hsieh and Shu-Ming Hsu on April 1st, 1989. He went to Taipei Municipal Jianguo High School in Taipei, Taiwan. Hung-Lun went on to attend National Taiwan University in Chemical Engineering, and graduated in June 2011. In August 2012, he entered the M. Eng program in Chemical and Biomolecular Engineering at Cornell University, and received the M. Eng degree in 2013. After graduation, he transferred to the PhD program in the same department in August 2013, and he studied under Professor Susan Daniel.

I dedicate this dissertation to my fiancée, family, friends and all members of the Cornell community that supported me over the last six years.

ACKNOWLEDGEMENTS

First and foremost, I would like to thank my supervisor Professor Susan Daniel, and the members of my special committee, Professor Gary R. Whittaker and Professor Christopher A. Alabi. I also thank all the members of the Daniel Research Group past and present for their support and friendship, especially Dr. Donald Lee for the initial training. I also thank the Whittaker Group, especially Dr. Jean Millet and Dr. Marco Straus for training me and teaching me about virology. I thank my parents and sisters for always being there for me in my life. None of this would ever be possible without them. Lastly, special thanks for my fiancée, I-Ting Lin, for understanding and supporting my work. Grants and funding are acknowledged at the end of each chapter.

TABLE OF CONTENTS

1. Literature review

1.1. Membrane enveloped virus ……...1

1.2. Influenza virus entry……1

1.3. Influenza risk assessment tool (IRAT)……..…….3

1.4. Acid sensitivity and stability….……4

1.5. Studying virus hemifusion at the single-virion level……..…...5

1.6. Performing single-virion fusion assay on highly pathogenic virus……...6

2. Image restoration and analysis of influenza virions binding to membrane receptors reveal adhesion-strengthening kinetics

2.0. Acknowledgement……...9

2.1. Introduction……...……..9

2.2. Materials and Methods……..14

2.2.1. Producing lipid vesicles for SLBs……..……14

2.2.2. Measuring surface charges of vesicles and virus……...……15

2.2.3. Assembling the microfluidic device……...……15

2.2.4. Forming SLBs inside microfluidic channels……..……16

2.2.5. Storing X-31 viruses until use…….16

2.2.6. Labeling the viral membrane with R18…….…17

2.2.7. Determining the virus concentration and size……17

2.2.8. Setting the camera rate and experiment time…….17

2.2.9. Conducting SPT binding experiments…….…….…..18

2.2.10. Restoring images and tracking particles in SPT videos…….……..18

2.2.11. Defining a “binding event” via visual cues……..……19

2.2.12. Filtering biased binding events……20

2.3 Results and discussion……20

2.3.1. Establishing conditions for high-quality SLBs……..……20

2.3.2. Controlling for long-range nonspecific electrostatic binding…….22

2.3.3. Introducing STAWASP image restoration algorithm for SPT……24

2.3.4. Comparing the performance of STAWASP……....26

2.3.5. Applying STAWASP for real X-31 virus binding videos……28

2.3.6 Analyzing the binding frequency rate and rate parameter k_{on}…….30

2.3.7. Analyzing the binding residence time distribution and unbinding parameter k_{off}.……36

2.3.8. Bridging SPT and SPR data analysis……...……..41

3. Viral fusion efficacy of specific H3N2 influenza virus reassortant combinations at the single-particle level

3.0. Acknowledgement……...……..46

3.1. Introduction……...……46

3.2. Materials and methods……..…….…...51

3.2.1. Cells, plasmids, and viruses……...……51

3.2.2. Preparation of influenza pseudoparticles……...……52

3.2.3. Western blotting……...……...…52

3.2.4. Immunofluorescence assay…….53

3.2.5. Preparation of liposomes…….……...…….53

3.2.6. Fluorescent labeling of viruses…….……..……54

3.2.7. NA inhibition assay……...…….54

3.2.8. Preparation of glass surfaces for supported bilayers……..…54

3.2.9. Fabrication of microfluidic devices……55

3.2.10. Forming supported bilayers in microfluidic channels……..…...55

3.2.11. TIRF microscope configuration……...…….....55

3.2.12. Image processing……..56

3.3. Results…….……..56

3.3.1. Influenza pseudotyped particle production and infectivity assays…….…....56

3.3.2. Single-virion fusion experiments……..…….……....57

3.3.3. Incorporation of HA and NA in pseudovirions…….…..…...64

3.3.4. HA and NA expression in transfected cells…….…..….65

3.3.5. Effect of NA inhibition on hemifusion kinetics…….…..…..68

3.4. Discussion……..…….……..…69

4. Evaluating the pandemic potential of influenza A virus (H10N8) according to hemagglutinin (HA)-mediated membrane fusion attributes

4.1. Introduction……...72

4.2. Materials and Methods……..76

4.2.1. Cells plasmids and antibodies……76

4.2.2. H10 expression characterization……....77

4.2.3. Cell-cell fusion assay……...……..78

4.2.4. Preparation of influenza pseudoparticles……...……78

4.2.5. Liposomes used to prepare supported bilayers……...……79

4.2.6. Preparation of glass surfaces for supported bilayers…….....80

4.2.7. Fabrication of microfluidic devices……80

4.2.8. Forming supported bilayers in microfluidic channels……80

4.2.9. Fluorescent labeling of viruses……...……81

4.2.10. Single particle hemifusion assay: microscopy……...…..81

4.2.11. Single particle hemifusion assay: experimental execution……..…82

4.2.12. Single particle hemifusion assay: image processing……..…….82

4.3. Results……...82

4.3.1. H10 characterization and H10 sera testing…….82

4.3.2. Cell-cell fusion assay results……..84

4.3.3. H10N8 pseudotyped particle production and infectivity assay……..85

4.3.4. Single-particle hemifusion assay……88

4.3.5. Extent of fusion……..92

4.3.6. H10 acid stability……...……93

4.4. Discussion……...……..96

5. Conclusion & outlook……...……..……98

6. References……...……..……100

Appendix A……...……114

Literature Review

1.1. Membrane enveloped virus

Viruses are obligatory intracellular parasites, and they can be simply categorized based on whether it has a viral envelope covering its protein capsids [1]. An enveloped virus obtains its membrane from the plasma membrane of the infected cell or host during the process of leaving the host (called "budding") [2]. Together with the viral membrane, viral glycoproteins also are assembled into the viral envelope. The viral envelope may help viruses avoid the host immune system, and protect the viral cargo (e.g. RNA, polymerase). On the viral envelope membrane, there are glycoproteins that serve to identify and bind to the receptor sites on the host's membrane [3]. Also, the viral glycoproteins also are responsible for releasing the virus genome into the host cells [4].

Enveloped viruses include numerous pathogenic or lethal viruses, e.g. influenza virus (Orthomyxoviridae family) [5], Ebola virus (Filoviridae family) [6], severe acute respiratory syndrome (SARS) virus (Coronaviridae family) [7], human immunodeficiency virus (HIV) (Retroviridae) etc. However, not all enveloped viruses use the same pathway for entry. The major route of virus internalization is clathrin-mediated endocytosis, used by vesicular stomatitis virus (VSV) [8]. Another route is macropinocytosis, which is a non-selective uptake mechanism, used by Ebola virus [9-11] and human respiratory syncytial virus [12]. Some viruses, such as influenza virus, can use both routes to be internalized [13-15].

1.2. Influenza virus entry

Influenza A viruses are enveloped, single-stranded, segmented, negative-sense RNA viruses that infect a wide variety of bird and mammalian species. Moreover, humans, swine, and birds are the biggest influenza virus reservoirs in the world [16].

In order to target their host, influenza A viruses require hemagglutinin (HA). HA is a trimeric membrane-embedded glycoprotein that is a critical determinant of host tropism (e.g. humans, pigs, birds and horses), and mediates both binding to host cell surface sialic acid receptors and fusion of viral and host cell membranes [17-19]. Because of its crucial role in governing cell entry, tissue and host tropism, HA is also a key factor in regulating viral pathogenicity [20, 21]. On the other hand, influenza viruses require neuraminidase (NA) envelope glycoproteins for viral egress[22]. NA protein is a tetramer on the surface of virions and is responsible for catalyzing cleavage of terminal sialic acids [23, 24]. NA's functional role is critical for the release of progeny viral particles from infected cells at late stages of the infection cycle [25], and prevents virus from binding to the mucus overlying the human airway epithelium [26]. Influenza A viruses are divided into subtypes based on antigenic and amino acid sequence differences of the HA and NA surface glycoproteins, composed of 18 and 11 known subtypes, respectively. While different HA and NA combinations are found in circulating influenza viruses, aquatic birds can be infected by most subtypes, while humans are known to be infected by three main subtypes: H1N1, H2N2, and H3N2 [27]. The human H2N2 subtype is not currently circulating, but was responsible for the 1957 pandemic [28]. The avian H5N1 and H9N2 subtypes have been recognized for their pandemic potential in the human population[29]. The transition of receptor usage from avian-like α2,3-linked to human-like α2,6-linked sialic acids represents a critical step for avian viruses to acquire efficient replication and transmission capabilities in humans[30]. Furthermore, understanding the effects of switching combinations of gene segments that occur during reassortment, in particular those encoding HA and NA, is critical for uncovering the basis of emergence of influenza viruses with increased pathogenicity and for pandemic

preparedness [31].

During influenza virus entry, which occurs through the endocytic pathway, conformational changes of the HA are critical for virus fusion to occur [32]. HA is a type I transmembrane protein and represents a prototypical class I viral fusion protein that has been widely studied both structurally and functionally. HA is initially synthesized as an uncleaved precursor, HA_0, which is proteolytically processed by host cell proteases into two subunits, HA_1 and HA_2, linked by two disulfide bonds. The HA_1 subunit contains a globular domain with residues responsible for binding to sialic acids, while the core of the fusion machinery, the hydrophobic fusion peptide, is found within the membrane anchored HA_2 subunit [20, 33]. The proteolytic cleavage event is critical for activating the HA, as it allows for exposure of the fusion peptide. In the late endosome, the pH drops from pH 6.5-6 to pH 5-4.5 causing the HA_2 fusion domain to undergo major conformational changes. These changes expose the fusion peptide and enable it to be inserted into the target endosomal membrane. HA_2 then refolds, and pulls viral and endosomal membranes together, allowing for hemifusion to occur and ultimately leading to the opening of the fusion pore and release of the viral genome [17, 34]. In previous studies, we and others have successfully applied a single-particle tracking (SPT) methodology combining total internal reflection microscopy (TIRFM), microfluidics, and supported lipid bilayers to study influenza HA-mediated fusion kinetics using native viruses or HA-pseudotyped viral particles [35-38].

1.3. Influenza risk assessment tool (IRAT)

Influenza is the virus pathogen that causes flu, which causes 12,000 to 56,000 deaths each year. In the 2017-2018 season, because the selection of strains used to make flu vaccines was incorrect, more than 6% of people that visited clinics and

emergency departments had an influenza-like illness [39]. This is the highest level of activity since the deadly H1N1 influenza pandemic, which caused the 284,000 deaths worldwide in 2009. Because correct prediction the flu vaccine each is critical in disease control and prevention, the Influenza Risk Assessment Tool (IRAT) was developed by the Centers of Disease Control and Prevention (CDC) to evaluate the pandemic potential of newly emerging influenza viruses or the viruses that currently circulate in animals. IRAT builds a framework which weights 10 risk elements and the top three weighted elements are human infection, transmission (laboratory animals) and receptor binding [40]. The other 7 elements include genomic variation, antiviral treatment susceptibility/resistance, existing population immunity, disease severity and pathogenesis, antigenic relationship to vaccine candidates, and global distribution (animals). The 10 risk elements are scored from 1 to 10, and each score is weighted according to importance of two scenarios: emergence and public health impact. The emergence scenario is the risk for the virus to achieve sustained human-to-human transmission, and the public health impact scenario is the risk for the virus to significantly impact public health if it were to achieve sustained human-to-human transmission.

1.4. Acid sensitivity and stability

Although the IRAT has already covered most of the important factors for evaluating the pandemic risk of influenza virus, there is evidence that besides virus receptor binding properties, virus fusion properties might also play a role in pandemic potential [41]. Russier and colleagues showed changes in the HA acid stability of the pandemic influenza virus (pH1N1) during its inter-species transmission from swine to humans. The HA activation pH decreased significantly when it transmitted from swine (activating pH > 5.5) to early human cases (pH 5.5), which further decreased in

human isolates characterized later in the pandemic (pH 5.4-5.2). Because the human airway tissue constitutes an acidic environment (pH 5.5-6.9), human influenza viruses have been shown to increase their acid stability to successfully infect host cells [42, 43]. On the other hand, other than the obstacles that influenza viruses face in the macroenvironment, there are more issues during the endosomal escape process. During endosomal trafficking, HA requires acidification to trigger the conformational change of its fusion peptide to form a pore on the endosomal membrane to release viral RNA. However, the low pH environment might also deactivate HA, so endosomal escape fails. HA stability was defined as how long HA can maintain its fusogenicity while in an acidic environment by Costello et al. in 2015 [35]. Considering these scenarios, the acid sensitivity and acid stability might be worthy to be considered as features important for evaluating the risk of an influenza virus pandemic.

1.5. **Studying virus hemifusion at single-virion level.**

To better understand influenza virus entry and get virion-level information (HA acid stability and sensitivity), single-particle tracking (SPT) is an useful technique. Before SPT was invented and performed on studying virus-host entry kinetics, a similar but less sensitive technique, the bulk fusion assay was first reported in 1984. Hoekstra et al. utilized the self-dequenching fluorescence of a lipophilic fluorophore, octadecyl rhodamine B (R18) to detect the membrane fusion of biological membranes [44]. Bulk fusion then was used by Lowy et al. [45] and Loyter et al. [46] to investigate influenza viral membrane fusion and study the hemifusion kinetics with human erythrocyte membranes. Melikyan et al. further improved the bulk fusion technique by combining it with fluorescence microscopy, and they were able to observe the hemifusion and pore formation of retroviruses with 293T cell membranes

at the level of single particles [47]. The single-particle tracking technique finally became fully matured when Wessels et al and Floyd et al. used supported lipid bilayers to replace actual cell membranes, and utilized total internal reflection fluorescence (TIRF) microscopy to enhance the signal-to-noise ratio [37, 38]. In their study, they were able to quantify the hemifusion and pore formation kinetics from individual virions, and they further used an empirical equation, a cumulative gamma distribution equation, to fit the kinetics curves. The equation is shown below:

$$p_H = \int_0^1 \frac{k_H^N t^{N-1}}{\Gamma(N)} e^{-k_H t}\, dt$$

With the fitting, they were able to extract two parameters from the kinetics, *k* and N, where k_H is the hemifusion or pore formation rate constant, *t* is lag time, and *N* is an additional fit parameter, which they correlated to the number of steps or the number of HA trimers that must act concertedly to initiate fusion [37]. k_H and *N* are usually plotted as a function of pH to study the dependence of hemifusion and pore formation on pH acidification that occurs in a maturing endosomal environment. Costello et al. further expanded the SPT technique to study virus-like particles [36], coronaviruses [48], and different influenza strains [35]. In my thesis, I will present my effort in expanding the SPT technique to study a surrogate virus system for pathogenic viruses, a pseudovirus system.

1.6. **Performing single-virion fusion assays on highly pathogenic virus.**

Pseudotyped particles, also called pseudovirions or pseudoviruses, are enveloped virus particles derived from a parental virus, typically a rhabdovirus (e.g. vesicular stomatitis virus, VSV) or a retrovirus (e.g. murine leukemia virus, MLV) that forms a viral core that can incorporate the envelope glycoprotein of a heterologous virus (e.g. influenza HA, or coronavirus spike) in its membrane [49-51]. Such viral particles acquire the host cell tropism, virus entry, and fusion characteristics governed by the

heterologous envelope glycoprotein used. As such, they constitute a powerful tool to study enveloped virus entry. Also, because they contain a replication-defective genome, they are safe surrogates of highly pathogenic enveloped viruses. Pseudotyped particles have been used for many applications, such as quantification of viral entry using reporter genes (e.g. luciferase or green fluorescent protein, GFP), investigation of the viral entry process of highly pathogenic viruses or viruses that cannot be cultured, and for controlling the host cell tropism of gene delivery vectors.

For VSV pseudovirus production, Lawson et al. [52] and Whelan et al. [53] generated a recombinant virus in which the native fusion glycoprotein-encoding gene (G) is replaced by a GFP-encoding gene. Because they lack the essential glycoprotein-encoding gene, particles with such defective genome cannot undergo multiple rounds of infection [54]. This recombinant virus is used to infect mammalian cells expressing heterologous virus envelope glycoprotein such as HA by transfection. This results in the production of pseudotyped particles that bud from the plasma membrane. Such pseudotyped particles can then be used to infect target host cells for infectivity assays. The GFP gene contained in the pseudotyped particle genome is expressed in infected cells, allowing for easy readout of infectivity. Halbherr et al. used the VSV pseudotyping for studying influenza H5N1 and showed that the particles can be used for accurate detection of neutralizing antibodies against influenza viruses [55]. In the presence of neutralizing antibodies, influenza H5N1 pseudoviruses were unable to infect cells.

For MLV pseudovirus production, human embryonic kidney (HEK)-293T cells are co-transfected with a MLV gag-pol packing construct, a pTG-Luc transfer vector encoding a luciferase reporter, and a plasmid encoding the viral envelope glycoprotein of interest. The MLV structural proteins assemble and form pseudotyped particles

with the expressed envelope glycoprotein and containing the luciferase reporter gene. As such, luciferase activity in infected cells can be used as a measure of infectivity of the pseudotyped particles. **(Fig. 1)**. The MLV pseudovirus production system (**Fig. 1B**) has been optimized and reported to be successful in producing and studying influenza H9N2 viruses [56]. Additionally, both pseudovirus systems described here can incorporate HA and NA from different strains. As such, they are ideal for studying influenza virus reassortment, as we can express specific combinations of HA and NA of interest. One useful application of the pseudovirus systems is that they allow us to study emerging influenza strains safely, which will be shown in this thesis.

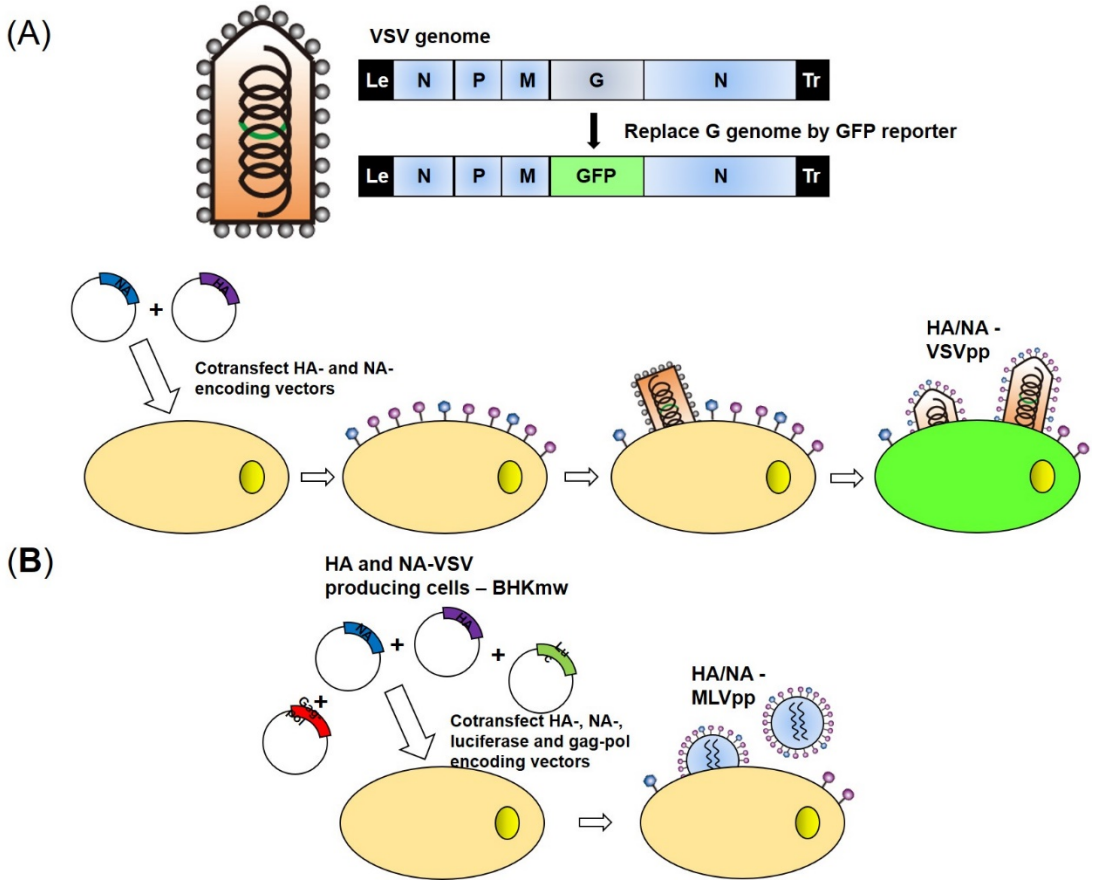

Figure 1. The cartoon shows the production of (A) VSV pseudoviruses and (B) MLV pseudoviruses. Both pseudoviral systems are designed so they can only undergo one infection cycle. Hence, the pseudoviruses are safer to use because they lack the ability

to replicate in the host cells.

CHAPTER 2

Image restoration and analysis of influenza virions binding to membrane receptors reveal adhesion-strengthening kinetics

Donald W. Lee, Hung-Lun Hsu, Kaitlyn B. Bacon, and Susan Daniel

School of Chemical and Biomolecular Engineering, Cornell University, Ithaca, New York, United States of America

2.0. Acknowledgement

This chapter has been accepted for publication in PLOS ONE as "Image restoration and analysis of influenza virions binding to membrane receptors reveal adhesion-strengthening kinetics" [57].

Author Contributions

SD conceived the project. S.D. and D.W.L. designed the experiments and wrote the manuscript. D.W.L. developed the algorithms and codes, performed final binding experiments, and analyzed the data. H.L.H. and K.B.B. measured the zeta potential of vesicles, prepared lipid samples, and optimized protocols. H.L.H. measured the virus concentration. All authors have given approval to the final version of the manuscript.

2.1. Introduction

Single-particle tracking (SPT) is a versatile technique for studying protein-protein binding interactions occurring at surfaces, particularly the binding of viruses to host cell membrane receptors [58-62]. Viral adhesion to host membranes is critical for viral infection, and dissecting this process is relevant for predicting virus emergence, determining susceptible hosts, or developing binding-inhibitory antiviral compounds.

SPT often deploys the use of imaging techniques such as total internal reflection fluorescence (TIRF) microscopy, which can track fluorescent virions within a 100-nm distance away from a surface (**Fig 2a**). The viral receptor can be loaded onto a flat substrate by tethering receptors to polymers attached covalently to the substrate [63], adsorbing lipid vesicles containing the receptor lipid or protein [64], or forming supported lipid bilayers (SLBs) containing membrane receptors [37, 61, 62, 65, 66]. The SLB option is advantageous because 1) the receptor type and surface density can be carefully controlled through bilayer preparation steps, 2) receptors are properly orientated in the membrane [67], 3) viral membrane fusion kinetics can be studied using the same assay [37, 38, 68-70], and 4) mobile lipids allow the virus to recruit receptors and form multivalent bonds. However, the SPT-SLB assay contains several technical challenges with experimental design, image processing, and binding kinetic data analysis that limit its adaptation as a standard analytical tool. To increase the utility of SPT-SLB assays, we explain the cause of and demonstrate solutions to these issues as we study of influenza virus binding to several types of α2,3 sialic acid (SA) glycolipids.

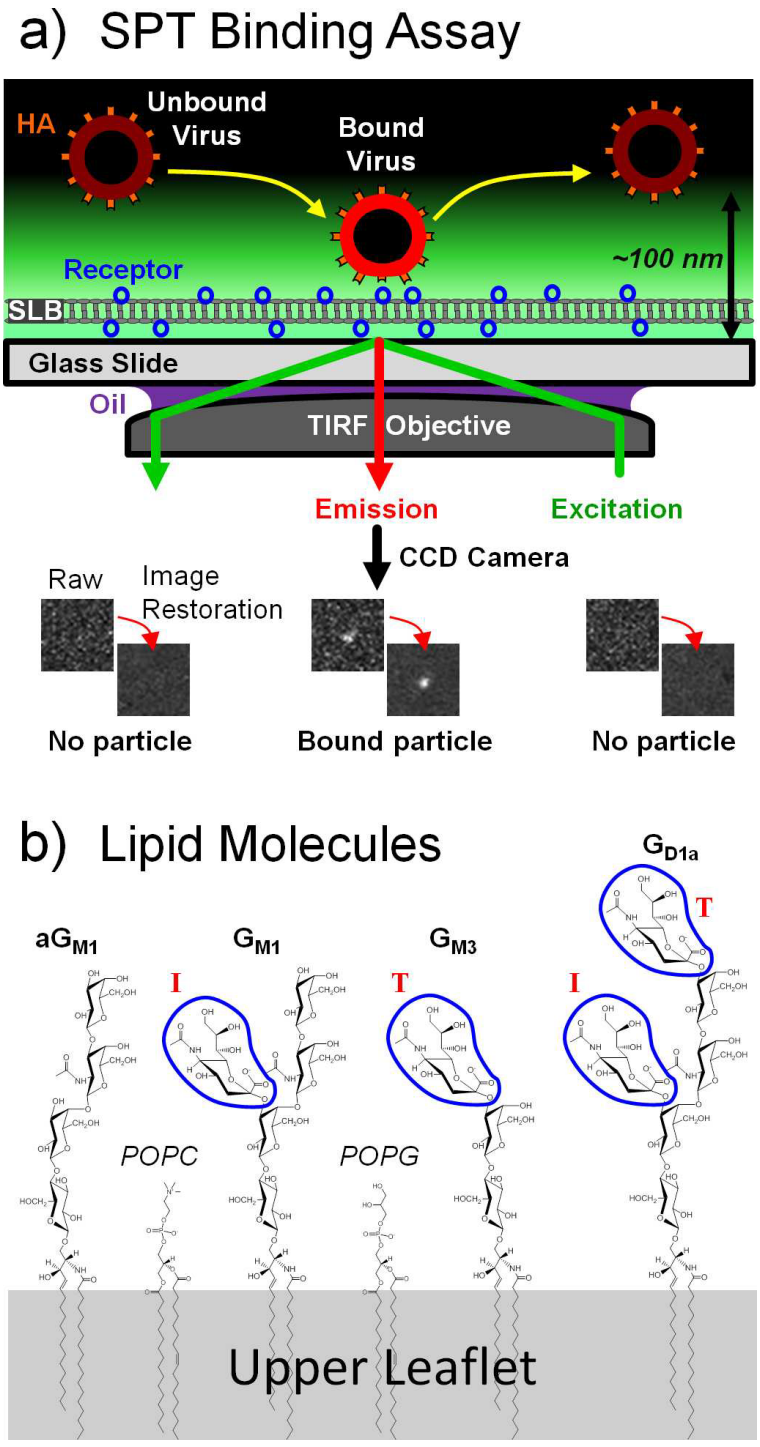

Figure 2. SPT binding assay and receptor structures. a) Setup of SLB on TIRF microscope. Evanescent field illuminates regions where SLB and virus interacts. b) Structure of the sialic acid receptors for X-31 tested here. The α2,3-linked sialic acid groups are circled by the blue perimeters. Following the notation by Suzuki et al. [71],

sialic acid groups are labeled as either being in the internal (I) or terminal (T) position.

One of the biggest barriers to using SPT for viral research is extracting particle information from images. Manually tracking particles is impractical, hence automated tracking software is needed and its proper performance is critical. Fluorescently labeled virions appear as white spots on a dark background, but often, dim particles exist that are only few pixels large and resemble bright shot noise. Dim particles are particularly detrimental to SPT binding studies because these are intermittently detected by the software and contribute many short, erroneous particle trajectories that skew the binding data. Increasing the particle fluorescence signal by using a more powerful excitation laser is not an effective solution to the problem because photobleaching destroys the signal before adequate data can be collected. Signal-to-noise ratios can be improved by developing better microscopy setups such as light sheet microscopy [72], using other dyes such as quantum dots [73, 74], or using dye-free strategies [75], but not all setups and samples can accommodate these improvement. Hence, developing image-processing techniques provides a means to benefit a broader range of studies with minimal changes to experimental procedures.

Typical SPT image analysis software usually performs the following three steps: image restoration, particle detection, and particle trajectory linking. While much effort has been invested in improving particle detection [76-82] and particle linking algorithms [78, 82-88], less effort has been focused on developing image restoration algorithms for SPT application [89]. Particle tracking software generally underperforms when the signal-to-noise ratio (SNR) is below 4 [78]. Most SPT studies use image restoration techniques originally designed for standard photographs

and videos [90-93], which do not adequately restore dim particles with features barely larger than that of shot noise pixels. To resolve the intermittent particle tracking errors, we developed and provide a SPT image restoration algorithm called STAWASP (Segmented Temporal Averaging While Avoiding Synced Pixels). This algorithm effectively uses both spatial and temporal information from the video pixels to stabilize particle intensities, preserve particle features, and remove substantial noise from videos.

Other challenges of SPT-SLB assays is customizing experiments for studying multivalent binding of viruses to receptor analogs, and interpreting the SPT binding/unbinding kinetic data. There are many experiment design choices to consider that affect the kinetic data, and we explain these choices in the context of designing experiments for studying influenza X-31 virus (H3N2 strain), which is a model for other enveloped viruses. Enveloped viruses are often labeled with membrane fluorophores since they do not interfere with protein functions and can be used in membrane fusion/dye-dequenching studies [36-38, 69, 70, 94]. Yet, quenched concentrations of membrane dye or inefficient labeling can generate substantial numbers of dim particles that are intermittently observable. Hence, tracking membrane-labeled X-31 virus serves as a useful test case for developing our image restoration algorithm and data analysis strategies.

A typical influenza virion surface contains roughly 400-500 hemagglutinin (HA) proteins [95] that govern the multivalent binding of the virus to sialic acid receptors on host cells. In this work, we measured the binding times of influenza viruses to SLBs that separately contained glycolipids aG_{M1}, G_{M1}, G_{M3}, or G_{D1a} (**Fig 1b**). Except for aG_{M1}, all glycolipids contain the α2,3 SA linkage but with different peripheral oligosaccharide structures. These structures serve to impart differences in binding

behavior that can be resolved when tracking stochastic binding events instead of ensemble-averaged binding events. We are also interested in counting the binding attempts made by viruses, which is not observable when using traditional binding assays that measure the change in collective adsorbed mass of viruses on a receptor-coated surface.

Generally, viruses bind better to SA at the terminal position [71, 96, 97], but SPR studies have shown that X-31 virus does not bind to G_{M3} even though it also has a terminal SA [64]. Contrary to this study, X-31 virus can infect chicken red blood cells that have been incubated with G_{M3} receptors [98]. We show that the flu virus does bind weakly to G_{M3}, observable with the experiment conditions and image restoration used in this work. Additionally, we show that binding residence time distributions reflect the adhesion-strengthening process via multivalent bonds that viruses use to stably bind to host membranes [99-102], and we present strategies to characterize these kinetics.

2.2. Materials and Methods

2.2.1. Producing lipid vesicles for SLBs

Supported lipid bilayers (SLBs) containing glycolipids are made from lipid vesicles. To make the lipid vesicles, 1-palmitoyl-2-oleoyl-sn-glycero-3-phosphocholine (POPC) and 1-palmitoyl-2-oleoyl-*sn*-glycero-3-phospho-(1'-*rac*-glycerol) (POPG) [Avanti Polar Lipids, Alabaster, AL] were separately dissolved in chloroform, while glycolipids monosialotetrahexosylganglioside (G_{M1}) [Avanti Polar Lipids, Alabaster, AL], monosialodihexosylganglioside (G_{M3}), disialoganglioside (G_{D1a}), and asialoganglioside (aG_{M1}) [Sigma-Aldrich, St. Louis, MO] were separately dissolved in a 2:1 chloroform to methanol solution. Glycolipids and POPC solutions were mixed

together to yield 1 mol % of glycolipids, while POPG was added when necessary to maintain the same anionic charge density across all lipid samples (equivalent to 2 mol % of monovalent anionic lipids). Lipids were dried under vacuum for 3 hours and rehydrated in MES buffer (1 mM MES, 150 mM NaCl, pH 7) such that the final lipid concentration was 1 mg/mL. Lipids were extruded 10 times using a 1-directional, 20-mL lipid extruder [Northern Lipids Inc., Burnaby, Canada] and a 50 nm pore-size polycarbonate membrane [GE Healthcare, Pittsburgh, PA] to yield 100 nm-diameter vesicles as determined by dynamic light scattering [Malvern Instruments, Worcestershire, UK]. Extruded lipids were collected in a new vial to ensure all lipids have passed the filter.

2.2.2. Measuring surface charges of vesicles and viruses

To ensure long-range electrostatic forces do not influence binding, the surface charges of the vesicles and lipid vesicles were measured using a zeta potential analyzer [Malvern Instruments, Worcestershire, UK]. Lipid vesicles at 0.25 mg/mL dilutions or X-31 virus (dye-labeled and unlabeled) at 0.008 mg/mL dilutions were added to zetacells (model DTS 1061) and subjected to light scattering measurements under an electric field. Triplicate measurements were performed at pH 7, 150 mM NaCl.

2.2.3. Assembling the microfluidic device

Virus binding experiments were performed inside a microfluidic device as shown elsewhere [70]. Glass coverslip slides (No. 1.5 thickness) [VWR, Radner, PA] were cleaned for 10 min using a piranha solution composed of 30 vol % hydrogen peroxide solution (contains 50 wt % H_2O_2) [Sigma-Aldrich, St. Louis, MO] and 70 vol% concentrated sulfuric acid [VWR, Radner, PA]. Glass slides were stored in deionized water until use. A polydimethylsiloxane (PDMS) [Dow Corning, Midland, MI] mold

of microfluidic channels (135 μm wide, 75 μm high, and 1.5 cm long) was prepared on top of a patterned, hydrophobic silica wafer produced at the Cornell Nanofabrication Facility (CNF). An air-dried glass slide and the PDMS mold were annealed together after a 30-second oxygen plasma cleaning step at 700 μmHg oxygen pressure. Tygon tubes (0.02" ID x 0.06" OD) [Saint-Gobain Performance Plastic, Worcester, MA] were attached to the microfluidic device such that one end is submerged into the loading solution and the other end is attached to a syringe pump [Harvard Apparatus, Holliston, MA]. The microfluidic device was setup on an inverted total internal reflection fluorescence (TIRF) microscope with a 100x oil immersion objective and 1.46 numerical aperture [Carl Zeiss, Oberkochen, Germany. Model Axio Observer Z1]. A 561 nm laser was shined at a 70° incidence angle to generate an evanescent wave that illuminates the virus within ~100 nm from the glass-water interface. The camera in the microscope is a Hamamatsu ImageEM C9100-13 (Hamamatsu Photonics, Bridgewater, NJ).

2.2.4. Forming SLBs inside microfluidic channels

SLBs that act as host membrane mimics were formed by rupturing lipid vesicle on hydrophilic glass surfaces [9, 49]. Lipid vesicle solutions at 1 mg/mL vesicle concentration were loaded into the microfluidic channels at a flow rate of 100 μL/min for 1 min. Vesicles were incubated in the channels for 4 hours to form high quality, high-quality bilayers . Excess vesicles were rinsed away by flowing MES buffer at a flow rate of 100 μL/min for 3 min.

2.2.5. Storing X-31 viruses until use

X-31 (H3N2/Aichi/68) influenza virus was obtained from Charles River [Charles River Laboratories, North Franklin, CT] at a protein concentration of 2 mg/mL, which comes in a frozen state. The stock virus solution was defrosted, aliquoted into 5 μL

volumes and stored at -80°C until used. An aliquot of virus was freshly thawed and used for each experiment. While this procedure requires viruses to undergo two thaw cycles that decreases viral infectivity relative to fresh virus, it is repeatable and out-competes the other option to store the virus liquid state until each use. The drop in infectivity for a 2nd thaw cycle has been reported to be from $10^{8.6}$ to $10^{7.0}$, whereas degradation over time at 0°C liquid state causes a larger drop in infectivity to $10^{6.5}$ [103]. The spherical morphology of virus was fairly well preserved after a 2nd thaw cycle, as confirmed in a separate EM study using the same virus batch [35].

2.2.6. Labeling the viral membrane with R18

To label the viral envelope with lipophilic fluorescent dye, 5 μL of the virus solution, 250 μL of MES buffer, and 4 μL of 0.01 mg/mL ethanol-dissolved octadecyl rhodamine B (R18) [Invitrogen, Carlsbad, CA] were mixed together in a vial. The mixed solution was gently sonicated in a water bath for 30 min at 25°C in the dark. Unincorporated R18 dye was filtered out using a G-25 sephadex spin column [GE Healthcare, Pittsburgh, PA] at 3000 RPM (743 RCF), and the eluted virus solution was stored in a LoBind vial [Eppendorf, Hamburg, Germany] to prevent loss of viral particles to vial surfaces while conducting the experiments. Before use, 250 μL of filtered virus solution was diluted with 1 mL of MES buffer. Note the labeling of virus with membrane dyes has already been shown to not affect HA function [104, 105].

2.2.7. Determining the virus concentration and size

The stock X-31 virus solution at an initial viral protein content of 2 mg/mL was diluted to 0.016 mg/mL. The virus solution was loaded into a flow chamber used in the NanoSight system (Malvern Instrument, Worcestershire, UK). Videos of particles floating in the solution were analyzed using the NanoSight software to extract the

virus concentration.

2.2.8. Setting the camera rate and experiment time

SPT studies face an unusual sensitivity to the image capture rate of SPT microscopy [58]. Sensitivity is attributed to the fact that a continuous time data of binding events, which could last anywhere from 0 to infinite time, are being sampled via a camera taking images at discrete time intervals with a set exposure time. Similar issues are explained by the Shannon Nyquist Sampling Theorem [106] and Bally et al. [58]. Short term binding events will inevitably be lost during the dead time between images, which means the overall binding event data will be affected by the camera setting. Increasing the imaging rate (by shortening the dead time) is not always viable as this would lead to excessive dye photobleaching issues and loss of data about long-term binding viruses. The camera setting was thus set according to the minimum binding residence time resolution desired relative to a reference time scale. We set the reference time scale based on that of virus-mediated *de novo* clathrin mediated endocytosis (CME), which takes roughly 3 min [107]. To encompass the CME timescale, camera was set to take images at 1 s intervals using a 100 ms exposure time for a total duration of 20 min (t_{movie} = 20 min).

2.2.9. Conducting SPT binding experiments

Labeled viruses were loaded into a SLB-coated microfluidic channel at a flow rate of 100 μL/min for 1 min. The flow was stopped by balancing the tube inlet and outlet pressures, which takes at most 1 minute to equilibrate. Stagnant flow conditions are necessary to prevent shear forces from affecting the binding/unbinding kinetics, especially of concern for weak binding interactions. Videos were recorded 1 min after the virus was introduced and the flow was stopped. The excitation laser was turned off in-between images during the 900 ms dead time to prevent excessive

photobleaching of fluorophores while recording the video. After experiments, a 20 vol % bleach solution was sent into the microfluidic channels to inactivate viruses. All experiments were performed at 25°C.

2.2.10. Restoring images and tracking particles in SPT videos

Shot noise from SPT videos was removed using our image restoration algorithm called STAWASP, to stand for Segmented Temporal Averaging While Avoiding Synced Pixels. Details about STAWASP are provided below. Particles were detected using a custom algorithm that looks for circular regions that are brighter than the background noise intensities. Particles' trajectories were determined using a basic algorithm that links particles from adjacent video frames together that are within 3 pixels away from each other. Any remaining and obvious errors in trajectories were corrected manually to increase the overall data accuracy, though the number of manually corrected trajectories constitutes a small portion of all trajectories returned by the automated tracking algorithm. All algorithms were developed using MATLAB (Mathworks, Natick, MA).

2.2.11. Defining a "binding event" via visual cues

Unlike SPR/QCM where the adsorbed mass to a surface can be detected, or AFM where binding force can be measured, SPT relies on visual cues that a binding event has occurred. These visual cues are not always obvious as virions can undergo stop-and-go motions. There are two criteria that can be used: Criteria 1 – a visible virus is always considered bound, or Criteria 2 – a visible virus that is immobile for at least a minimum duration time (t_{cutoff}) is considered bound. With Criteria 1, a mobile virus is treated as only 1 binding event regardless if this particle stops at and moves to several places. The concern with Criteria 1 is that the more interesting "stopping" events are ignored and the virus may not always be in contact with the SLB while

moving. For instance, the virus could be rolling along the SLBs, unbinding and rebinding to receptors, or simply floating near the field of view of TIRF without making contact. With Criteria 2, a single mobile virus can generate multiple binding events when it remains temporarily immobilized during the stop-and-go motion.

While Criteria 1 may be more appropriate only when studying the lateral diffusion of viruses into coated pits [108], we used Criteria 2 because an immobile virus is most certainly bound to the SLB. In this regime we are then corresponding most closely to the biological situation of virus binding events that lead to *de novo* CME occurring at stationary sites [109]. However, we must decide a minimum binding time for a binding event (t_{cutoff}), otherwise there would be no visual cue to discern a bound virus from a floating virus. We chose a t_{cutoff} of 5 frames (or 5 s) based on the performance of the automated particle tracking software. Note that the choice to t_{cutoff} will always be arbitrary because we are relying on visual cues, and not physical contact, to discern binding event. Ideally, we would want to capture events upon contact with the smallest t_{cutoff} possible. Furthermore, the camera exposure time and frame rate set a minimum cutoff time. We later investigate how the choice of t_{cutoff} affects the binding data.

2.2.12. Filtering biased binding events

When analyzing the binding residence time distributions, some binding events must be discarded due to ambiguity or bias. Particles that existed since the first frame (left-censored data) of the video were discarded since the actual binding time is uncertain. Those that bound after half of the movie time (½ t_{movie}) were also discarded because binding events that last longer than ½ t_{movie} cannot be observed in a fair manner as those that last for shorter times. Virions that stayed bound by the end of the movie (right-censored data) were included in the data if they initially bound before ½

t_{movie}. Due to the filtering of biased binding events, binding survival curves are drawn only up to ½ t_{movie}.

2.3 Results and discussion

2.3.1. Establishing conditions for high-quality SLBs

There are several ways to form SLBs: Langmuir Blodgett, lipid film rehydration, or vesicle rupture [65]. When using microfluidics, the vesicle rupture strategy is an effective means to form SLBs as it simply requires loading solutions of lipid vesicles into the channels. However, such method has previously been reported to cause low-quality SLBs if the devices are plasma cleaned [110]. To overcome this issue, which can be especially problematic when studying weak binding interactions, we determined conditions at which high-quality SLBs form with very minimal defects that viruses bind nonspecifically to by optimizing vesicle concentration and SLB formation time. Some issues with using lower vesicle concentrations are the creation of defective SLBs that induce nonspecific binding and spontaneous virus fusion (**Fig. 3a**), most likely due to interaction with edges of SLB patches. Defective SLBs like these could be useful for developing antiviral surfaces and may be worth exploring as a future work. However, since the focus of this work is on studying binding interactions, we sought conditions for reducing nonspecific binding events. Using at least 1 mg/ml vesicle concentration worked well. The SLB formation time is also important and can vary based on pH or salt [111], lipid compositions [112], and glass surface treatment [113]. For our SLBs, at least 3 hours were needed to reduce non-specific binding of viruses to negligible levels (**Fig. 3b**). Additional blocking steps were not required since SLBs themselves act as passivation layers. Dye-labeled bovine serum albumin, which is a typical blocking agent, did not bind to these bilayers to any detectable level (data not shown). Furthermore, inclusion of blocking

agents could instill uncertainty, as one must confirm that these do not coat the receptors, coat the viruses, or disrupt the SLB.

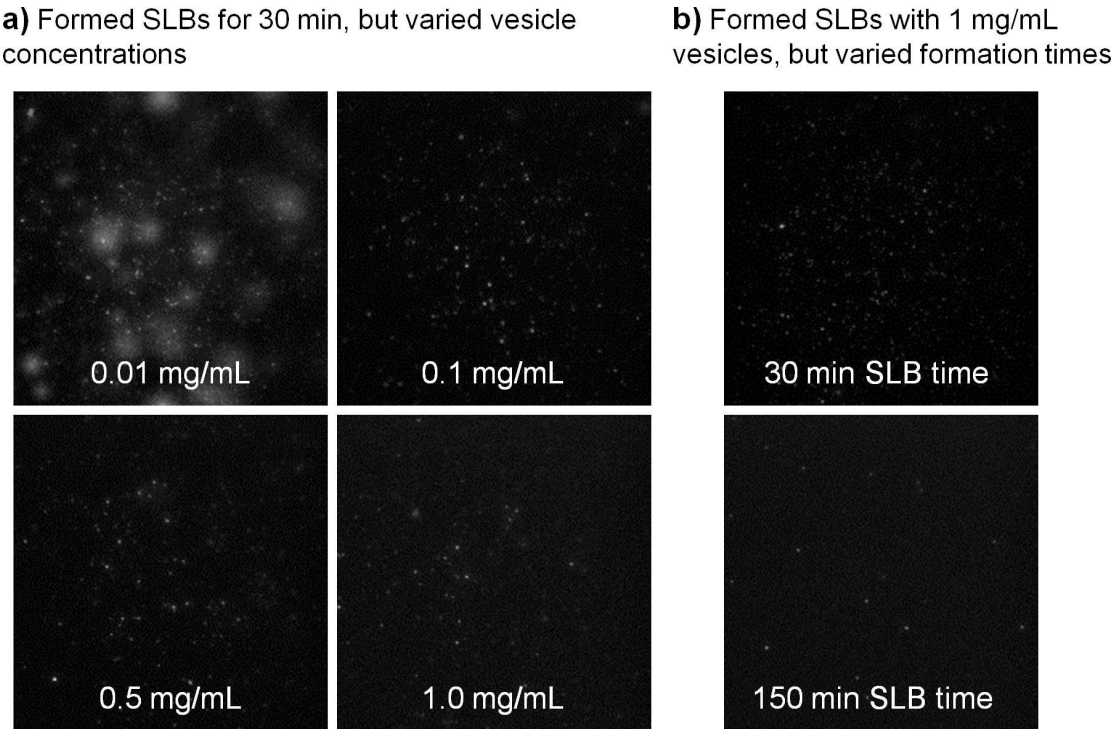

Figure 3 Optimizing SLB formation to reduce nonspecific binding. a) SLBs were formed over 30 min using 1% aGM1 receptor-less lipid vesicles at varying concentrations (white text). X-31 nonspecifically bound and spontaneously fused to SLBs (as noted by the radial release and diffusion of R18 into the supported bilayer) formed with low vesicle concentrations. b) The SLB formation time (white text) was varied while maintaining a constant 1 mg/mL vesicle concentration. Nonspecific binding was reduced greatly when SLBs are formed over at least 150 min. All images in panel a and b, were taken 30 min after loading the X-31 virus.

2.3.2. Controlling for long-range nonspecific electrostatic binding

Controlling long-range, electrostatic interactions is essential for ensuring that the observed binding events are due to specific virus-receptor interactions. The net charge

varies across aG_{M1} (0 charge), G_{M1} (-1 charge), G_{M3} (-1 charge), and G_{D1a} (-2 charge). To maintain the same receptor concentration and charge density of the bilayers, charged lipids must be added. Negatively-charged POPG lipids were added to equalize the negative charge density across all the SLBs (**Table 1**). Positively charged lipids could also be used to neutralize charges from the lipids, but since viruses are negatively charged, clusters of positively charged lipids could potentially induce non-specific binding. The surface charge of the virus must also be monitored, as the usage of too much lipophilic dye R18, which is positively charged, could change the polarity of the virus surface. The zeta potentials of all lipid vesicles and dye-labeled X-31 virus were negative and less than 5 mV in magnitude (**Table 1**). These magnitudes are much lower than 30 mV zetapotentials that could lead to nonspecific electrostatic attraction/repulsion between the virus and receptors [114]. The high salt content of the buffer also helps screen the charges. Long-range, nonspecific interactions are unlikely to play a major role in the viral binding kinetics here, enabling us to focus more on measuring the binding of viruses to their putative receptors.

Table 1. Zeta potential measurements of vesicles and viruses. suv = small unilamellar vesicles.

Sample			Zeta potential (mV)
1% aGM1	2% POPG suv	97% POPC	-3.45±0.50
1% GM1	1% POPG suv	98% POPC	-3.32±0.59
1% GM3	1% POPG suv	98% POPC	-4.60±1.19

1% GD1a	0% POPG suv	99% POPC	-3.47±0.73
X-31 virus with R18			-2.02±0.26
X-31 virus without R18			-10.11±0.55

2.3.3. Introducing STAWASP image restoration algorithm for SPT

Shot noise is rooted in low-signal, digital images due to the discrete photon collection method of digital cameras and complex electronic signal amplification hardware. In SPT videos, the airy rings of dim particles are barely larger than 2x2 pixels, making them nearly indistinguishable from noise. There are three major image restoration approaches: spatial, temporal, and spatio-temporal filtering. Spatial filtering removes static noise pixels based on how abnormal a pixel's intensity is compared to neighboring pixels. This method could produce artifacts such as particle blurring. Temporal filtering evaluates how pixel intensity changes over time to remove high-frequency noise fluctuation. However, it can cause particles to become blurred or faded. Spatio-temporal filtering combines aspects from both approaches, but this could become computationally expensive if it requires tracking local spatial regions over time.

Our STAWASP image restoration method can be classified as a spatio-temporal filter, and the algorithm is explained in **Fig. 4**. In short, this algorithm removes noise and preserves particle signals by averaging images (or stacking images) together in spatially and temporally-divided pixel segments. The unique feature of this algorithm is the method at which segments are determined with little input about what is or is not a particle. Segments are determined based on how synchronous a cluster of pixels fluctuates with time. For instance, the chance all 13 pixels in a circular area **(Fig. 4a**) synchronously increase intensity from one frame to the next is improbable due to

random noise and highly probably if a particle appears/disappears/moves. Pixels that change intensity synchronously are marked as "synced pixels" (**Fig. 4b**). Each pixel in the 2D image is then averaged through time, but the averaging is done in segments separated by the appearance of synced pixels (**Fig. 4c**).

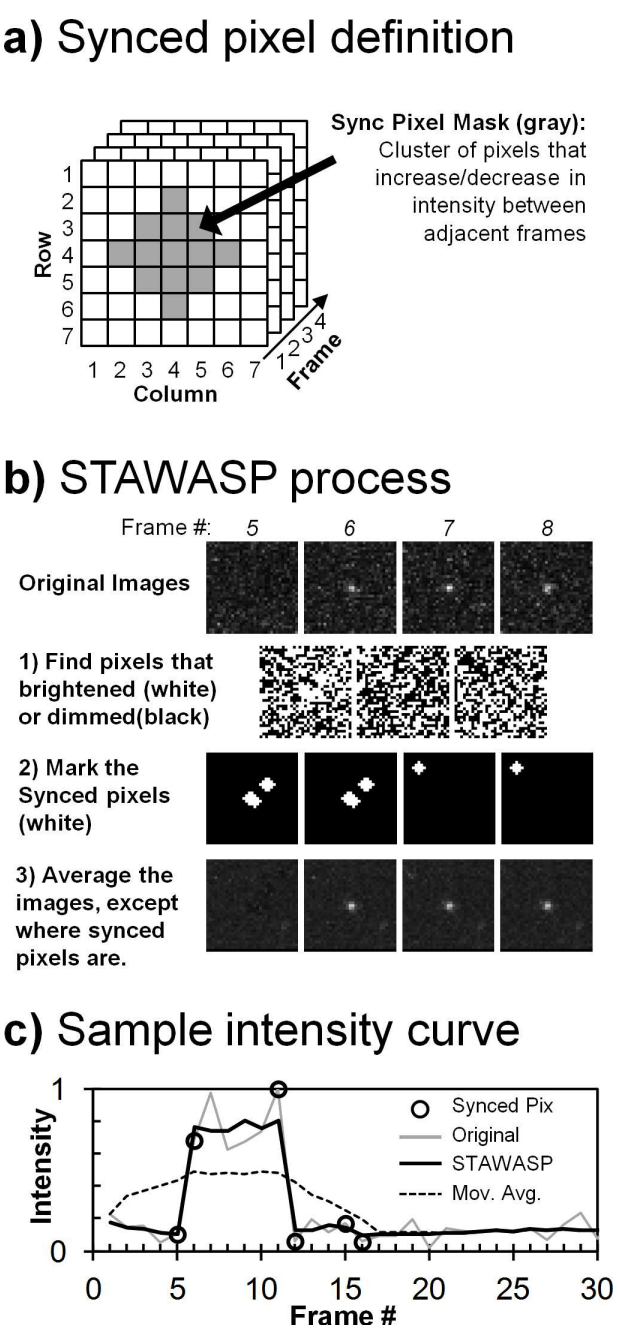

Figure 4. STAWASP algorithm. a) A local cluster of pixels (gray pixels) must either increase or decrease in intensity between consecutive frames to be classified as synced pixels. The pixel cluster size must be larger than a pixel and smaller than the

particle of interest. Here, at least 80% of the gray pixels must be synced. b) The steps to determine synced pixels are portrayed here for a particle appearing at frame 6. Since synced pixels are determined using two adjacent frames, synced pixels are marked on both of those frames. Note that false synced pixels can be generated by random noise fluctuations, but these do not necessarily cause a false particle to appear. c) The intensity trace for the center pixel of the particle images part B is shown when using STAWASP or the regular 10-frame temporal averaging scheme. With STAWASP, temporal averaging is performed in a segmented fashion such that temporally-adjacent, synced pixels are not averaged together.

2.3.4. Comparing the performance of STAWASP

The performance of the STAWASP image restoration was compared against other common methods, using a first simulated, noise-ridden video of binding particles (**Fig. 5**). The signal-to-noise ratios (SNRs, defined here as the particle peak intensity divided by the standard deviation of the noise intensity) were varied between 0.5 to 5. The Mean, Median, and LoG (Laplacian of Gaussian) noise filters intermittently revealed particles with SNRs $\geq$ 2.2, whereas particles with SNRs $<$ 2.2 were undetectable. The 10-frame temporal averaging method was able to reveal particles with SNRs $\geq$ 1.1, but all the particles faded in and out of view. The STAWASP algorithm was able to reveal particles with SNRs $\geq$ 1.1, and it preserved the appearance/disappearance times of particles with SNRs $\geq$ 2.2.

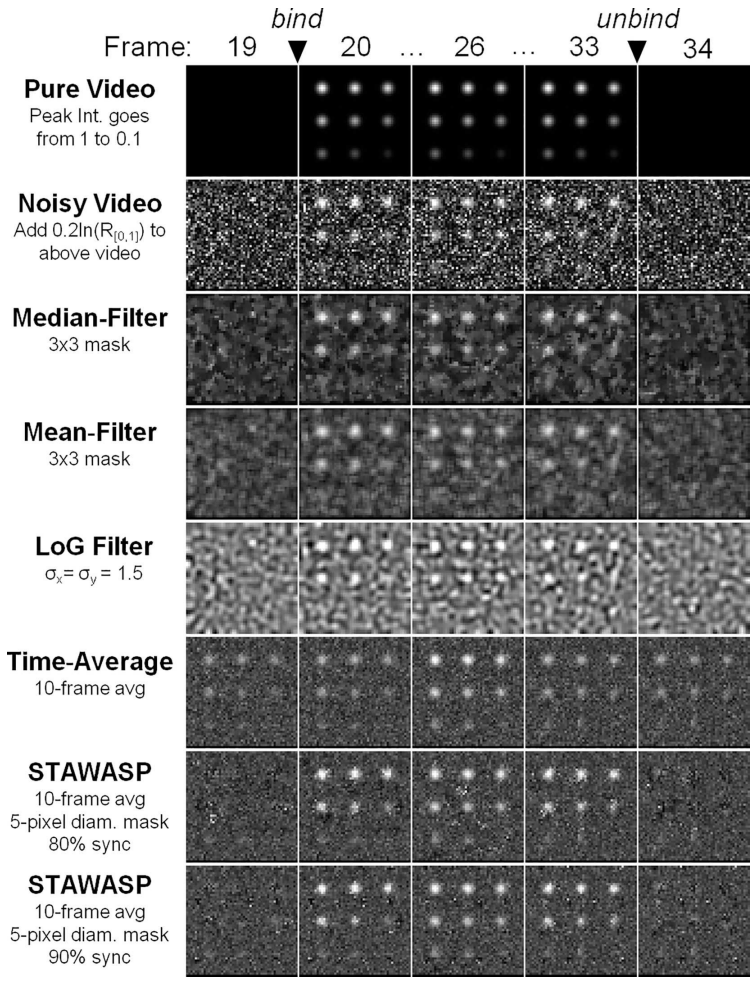

Figure 5. Testing various image restorations on a simulated movie. A simulated movie with noise was generated to compare image restoration performance (see Supporting Materials 1.3 for simulation details). The pure video shows particles with varying intensities appearing at frame 20 and disappearing after frame 33. Noise is added according to the function N = -0.2ln(R), where R is a uniform random number from 0 to 1. The SNRs of the 9 particles, from top left to bottom right are as follows: 5.0, 4.4, 3.9, 3.3, 2.8, 2.2, 1.6, 1.1, 0.5. The LoG (Laplacian of Gaussian) spatial filtering method is described by others [89, 115].

No image restoration is perfect, and a common artifact of the STAWASP algorithm are short-lived bright pixels throughout the movie, which is a result of the inability to

distinguish a small cluster of bright noise from an actual particle. These artifacts are dealt with later by the particle detection and tracking algorithms that filter out false particles (or shot noise that looks like particles) based on the criteria for a real binding event, as discussed above. We use a custom tracking algorithm that links particles together within 3 pixels between frames. Since determining the improvement of tracking in real SPT videos is difficult due to the inability to know the "true" binding events, we instead used a simulated video of particles and noise to assess the overall improvement in tracking. In short, STAWASP-restored videos enabled our SPT software to extract binding residence time curves that converges to the true data for when $t_{cutoff} > 5$ s, whereas the true data is not obtainable without any restoration. Note that for actual SPT videos involving X-31 viruses, we manually correct any obvious, erroneous trajectories to increase the accuracy of the data.

2.3.5. Applying STAWASP for real X-31 virus binding videos

We next show real images of viral binding before and after using STAWASP image restoration (**Fig. 6**). The clarity provided by the restored image is critical for obtaining accurate number statistics of viral binding. A qualitative assessment of the virus binding microscopy images shows that X-31 binds most frequently to G_{D1a}, less frequently to G_{M3}, and negligibly to G_{M1}. The control case shows a minimum level of nonspecific binding of X-31 to aG_{M1} SLBs, which confirms high-quality SLBs were formed inside microfluidic channels. The binding levels of virus to aG_{M1} bilayer also serves to characterize nonspecific binding levels, which can be contributed either by microdefects in the SLBs or denatured HA proteins that can insert hydrophobic residues into the SLBs.

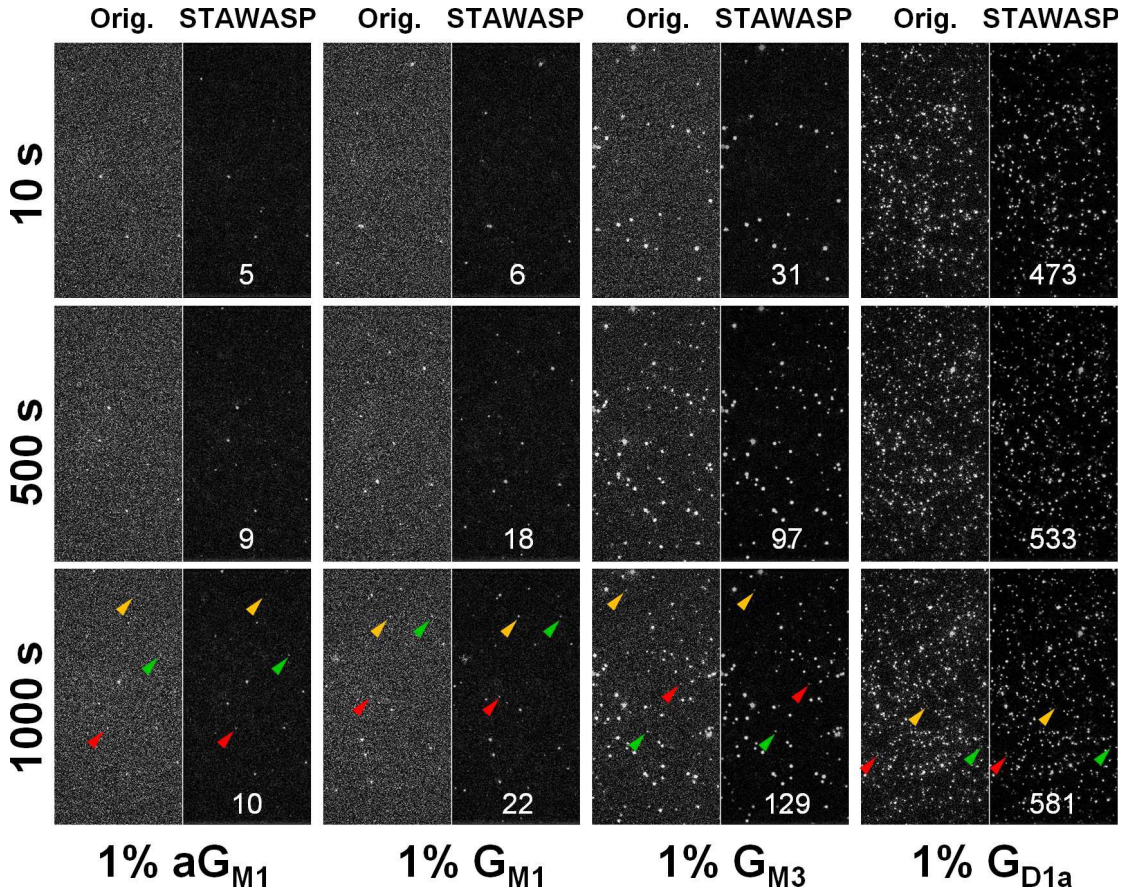

Figure 6. Sample images of viruses binding to glycolipids with and without image restoration. Few examples of restored particles are shown by the colored triangles. The white number shows the particle count, P_{count}, for the right half of each image, which represents a physical size of 82 μm high x 41 μm wide using 512 x 256 pixels. Note that P_{count} is not the same as N. We show P_{count} for qualitative comparisons only, since quantitative comparisons must be done using N instead, which is determined after the particle linking step. The time on left is the video recording time, which starts ~60 s after the virus is loaded, and therefore some virus exists at time 0. We show images starting at 10 s merely because the performance of STAWASP is optimal after 10 frames. We provide original movies without any image restoration for the first 300 s as supplemental files, played at 10x real time where 1 frame = 1 second. STAWASP-enhanced movies are provided for X-31 binding to G_{M3} (S5

Video) and G_{D1a} (S6 Video). Variations in particle intensities are caused by several factors, such as variable levels of dye that incorporated into the viral membrane, different degrees of photobleaching, and uneven microscope illumination (viruses in the center are generally brighter than those near the edges).

Some interesting observations from the SPT videos are surface-diffusing viruses. As mentioned in the Methods section, surface-diffusing viruses can be a result of rapid binding/unbinding events, tethered virus to mobile receptors, or rolling viruses. There are higher levels of surface-diffusing viruses in G_{D1a} bilayers compared to G_{M3} bilayers. The most likely explanation seems to be that the "diffusion" is actually rebinding events happening in rapid succession. For G_{D1a}, a virus rebinding to the bilayer is a highly probable event due to favorable binding interactions. For G_{M3}, the rebinding probability is much lower, and thus virus particles are more likely to float away from the field of view rather than bind to an adjacent site. The other possibilities, either that the virus is rolling or moving with a few attached glycolipids, seem less likely because the virus is much larger than a lipid and the G_{D1a} receptor density is too high. There are roughly 420 receptors per pixel (assuming a lipid occupies 0.61 nm^2 [116] and 1 pixel = 25600 nm^2), hence it would difficult for a virus to traverse long distances without forming immobilizing, multivalent bonds.

2.3.6. Analyzing the binding frequency rate and rate parameter k_{on}

Before discussing the virus binding kinetic data, we must first clearly define variables associated with SPT data analysis, as summarized in **Table 2**.

Table 2. Variables involved with SPT data analysis

Variable	Definition
P_{count}	Number of particles detected in an image
N	Number of binding events
N_+	Accumulated number of binding events since the movie started
N_-	Accumulated number of unbinding events since the movie started
t	Time elasped in the movie
t_{res}	Binding residence time (or contact time) of virus to receptors
t_{cutoff}	Minimum binding residence time required for a binding event
t_{movie}	Total duration time of the SPT video

Note that $N \leq P_{count}$ (unless t_{cutoff} = 1 frame) because not all particles seen in the movie satisfy the binding event criteria that a particle must remain immobile for longer than a certain cutoff time. Furthermore, when discussing SPT data, distinguishing normal time t and residence time t_{res} is important. For instance, N vs t plots portray the net number of binding events as a function of time, whereas N vs t_{res} plots portrays how many binding events last longer than t_{res} time (which is a survival function).

We first analyzed the N vs t plots for X-31 binding to the SA receptors. N is related to the other variables by the equation $N(t) = N_+(t) - N_-(t) + N_0$, where N_0 is the N when the movie starts. The N(t) data clearly shows that G_{D1a} bilayers have a higher capacity to hold onto viruses (**Fig. 7a**, blue line), versus other receptors. One

interpretation of the slowly rising net virus binding curve of G_{M3} (**Fig. 7a**, green line), relative to G_{D1a}'s curve, is to say G_{M3} is not a functional receptor. In fact, SPR studies concluded that G_{M3} is not a receptor for X-31 [64], though the authors studied viruses binding to lipid vesicles instead of SLBs, using half the G_{M3} concentration than what was used here, and while applying a slight hydrodynamic flow that could prevent weak binding events. However, having a dN/dt ~ 0 does not mean there is no binding rate, similar to how when a system reaches equilibrium, a forward/reverse reaction still exists.

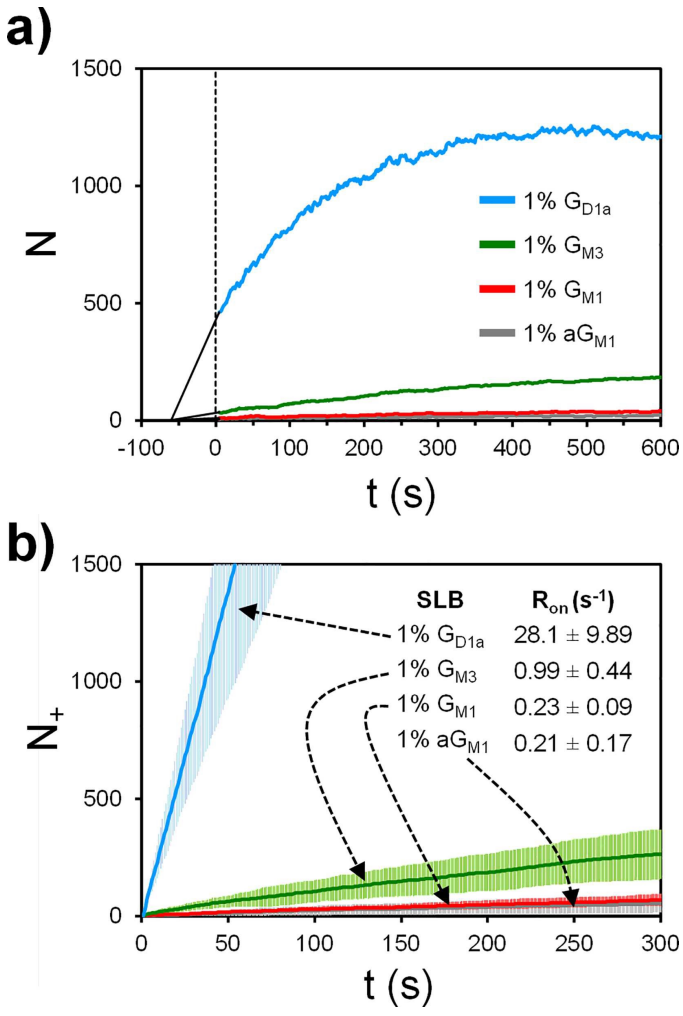

Fig 7. Two types of binding rate data of X-31 to various receptors. A) N vs t plots for one representative data set from a triplicate set. Negative time means time before recording, and the solid black lines are just an extrapolation to -60 s when the viruses

are estimated to first reach the SLBs. B) N_+ vs t plots, averaged over a triplicate set of data. The slope of this plot corresponds to binding frequency rate R_{on}. The error bars are the standard deviations, computed using 3 different trials.

The N_+ vs t plots (**Fig. 7b**) show that X-31 does in fact bind more frequently to G_{M3} than to aG_{M1} and G_{M1}. The slope of the N_+ vs t plots yields the binding frequency rate R_{on}, and R_{on} for G_{M3} is 3 STDs higher than that of aG_{M1} and G_{M1} cases. Our data suggest that G_{M3} can be a functional receptor for the virus.

Despite G_{D1a} and G_{M3} each having a terminal SA known to promote binding [71], X-31 binds to G_{D1a} ~30 fold more frequently than to G_{M3}. This cannot be explained by the presence of 2 SA per G_{D1a} molecule, as spatial distances between SA do not allow them to bind to 2 binding sites of an HA trimer (**Fig. 8**), including alternative binding sites located at the HA1/HA2 junction [117]. Additionally, the lack of binding of X-31 to G_{M1}'s internal SA suggests that the virus is not binding to the same internal SA in G_{D1a}. The extended distance of terminal SA from the SLB hydrophobic layer appears to promote binding. Access to G_{M3}'s internal SA may be sterically hindered by the close proximity of terminal SA to the bilayer.

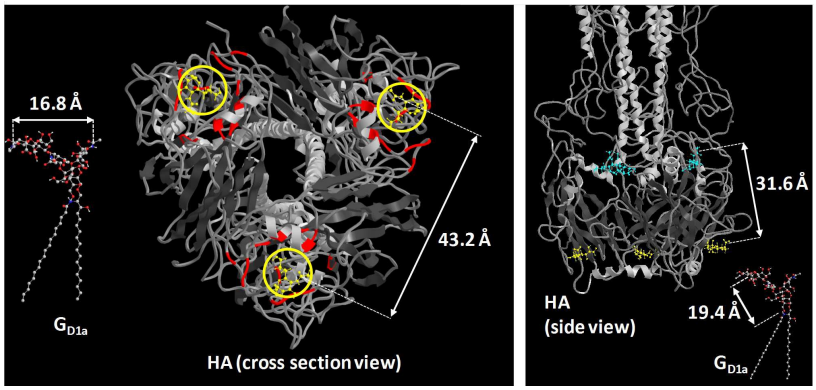

Figure 8. Using structural arguments to understand binding results. Left) View of HA protein head group in relation to G_{D1a}. Red regions show the binding pockets

and yellow circles show where sialic acid are located. Right) Side view of HA protein in relation to G_{D1a}. Teal molecules are sialic acids at potential secondary binding sites. The SLB would be on the bottom side of the protein, while the viral membrane would be on the top side. The hemagglutinin structure and sialic acid positions were obtained by Sauter et al. [117] PDB ID: 1HGG.

Binding rates are often characterized via a binding rate constant k_{on}, but SPT data do not provide a single value for k_{on} as we will discuss the reasons for later. Starting with the standard approach for finding a single k_{on} value, the k_{on} parameter can be solved for via the relation $R_{on} = k_{on}[V][SA]A_{cam}$ where A_{cam} is 6274 μm^2 for our camera field of view, [V] is the visible virus concentration in the bulk solution, and [SA] is the surface density of free receptors in the SLB. Since R_{on} is determined using early time points of the experiment, this enables the assumptions that [SA] and [V] are approximately equal to initial values right when the virus is loaded into the channels. Therefore we can treat $[SA] \approx [SA]_{init}$ and $[V] \approx [V]_{init}$ to estimate the binding rate constant k_{on}. The concentration $[V]_{init}$ is ~4.5 pM based on Nanosight measurements, and the receptor surface density $[SA]_{init}$ is ~16500 μm^{-2} for 1 mol % assuming a lipid occupies 0.65 nm^2 [116]. With these constants, the values for k_{on} are $(4.4\pm3.6)x10^2$, $(5.5\pm2.0)x10^2$, $(2.1\pm0.9)x10^3$, and $(6.0\pm2.1)x10^4$ 1/Ms for aG_{M1}, G_{M1}, G_{M3}, and G_{D1a} respectively, when using the binding event criterion t_{cutoff} = 5s. The k_{on} values for G_{M3} and G_{D1a} are within the expected range found by other binding assays, which have reported $k_{on} = 2x10^3$ $M^{-1}s^{-1}$ for multiple HAs binding to fetuin [118], $k_{on} = 3.61x10^4$ $M^{-1}s^{-1}$ for soluble HA binding to G_{D1a} [119], and $k_{on} = 1.6x10^6$ $M^{-1}s^{-1}$ for X-31 virion binding to vesicles containing 0.5 mol% Neu5Acα2-3nLc4Cer [64].

We now discuss why there can be multiple values of k_{on} and caution against the direct comparison of k_{on} from SPT assays to ensemble assays. Both k_{on} (or R_{on}) depend on the choice of t_{cutoff} because t_{cutoff} dictates how many binding events are included in a data set (**Fig. 9a**). For instance, by setting t_{cutoff} to be infinite, no binding events will exist that meets this requirement, hence, $k_{on} \rightarrow 0$. Conversely, setting t_{cutoff} to be 0 would make k_{on} seem to diverge to infinite because there will be no distinction between a binding event, elastic collision, or floating virus that is simply visible on the camera. Since the chance for a binding event to exceed a certain t_{cutoff} value is dictated by the binding residence time distribution, this means a relationship between k_{on} and k_{off} exists and the two parameters are not entirely decoupled as one would normally expect. In other words, the ability to observe a binding event is affected by the ability of the virus to stay bound long enough to be observed. To understand this relationship, we generated a plot for SPT data, that relates R_{on} (which is directly proportional to k_{on}) to the choice for t_{cutoff} (**Fig. 9b**).This plot also serves to facilitate the comparison of binding data taken across various t_{cutoff} settings.

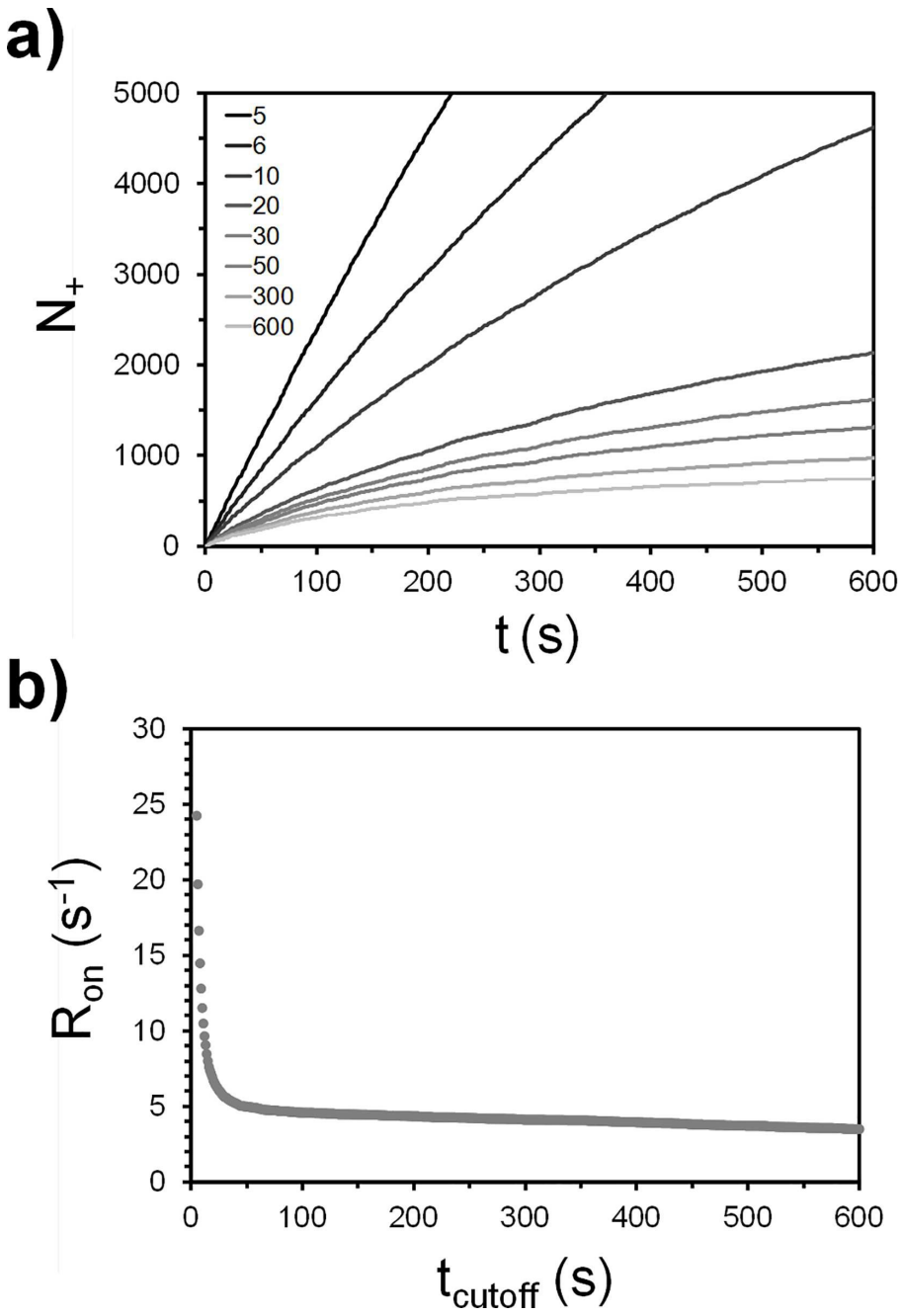

Figure 9. Observing how binding kinetics changes with choice of t_{cutoff} for a 1 % G_{D1a} trial. a) N_+ vs t at varying t_{cutoff} settings shown in the legend. b) R_{on} vs t_{cutoff} plot showing how R_{on} is affected with t_{cutoff} choice.

2.3.7. Analyzing the binding residence time distribution and unbinding parameter k_{off}

We next analyze the N vs t_{res} plots that portray information about the binding residence time distribution and unbinding rates (**Fig. 10a**). The unbinding curves did not agree with the 1:1 binding model (Eq. 1), and double exponential fit model (Eq. 2).

Eq. 1 : single binding energy population

$$N = N_0 \exp(-k_{off} t_{res})$$

Eq. 2 : double binding energy populations

$$N = N_{0,A} \exp(-k_{off,A} t_{res}) + N_{0,B} \exp(-k_{off,B} t_{res})$$

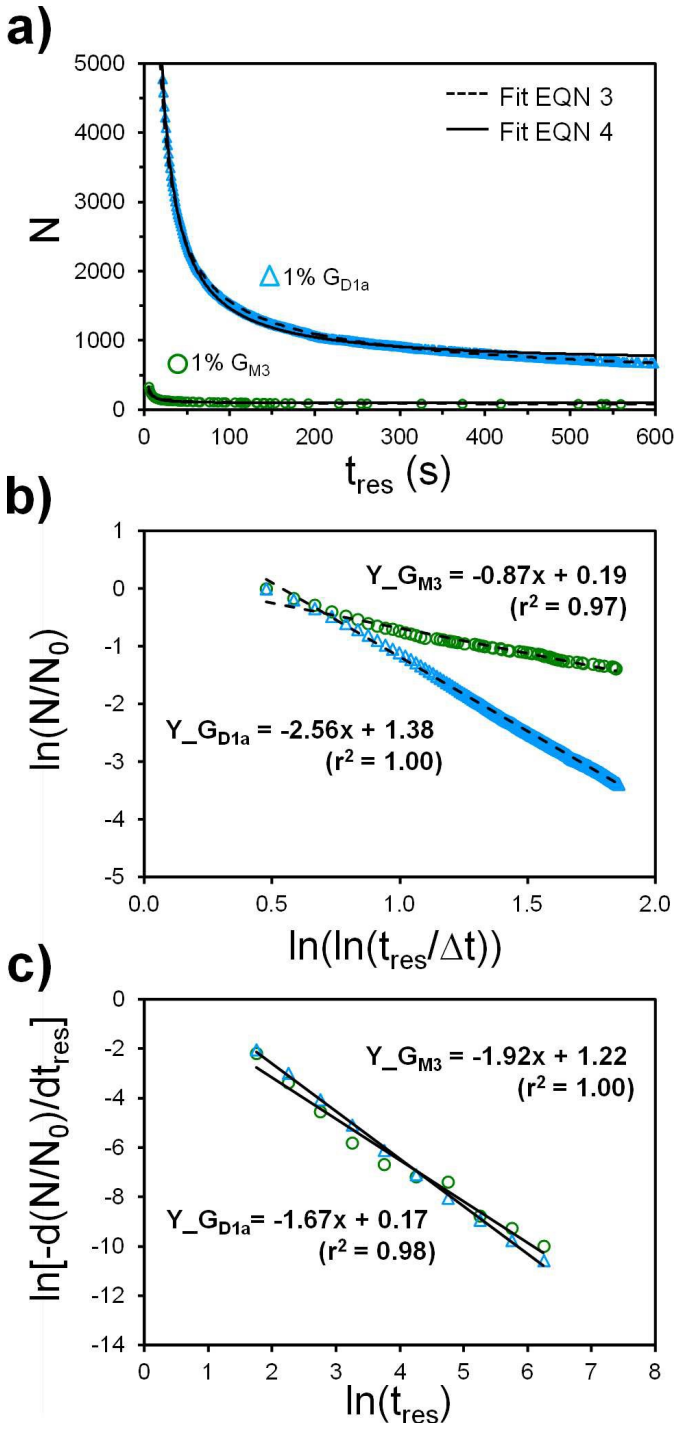

Figure 10. Representative X-31 binding survival curves and empirical fits. a) The number of virus bound, N, is plotted against the residence time, t_{res}, to yield a survival curve for binding. The Eq. 3 fit parameter for G_{M3} is [A = 0.87, B = 0.19] and G_{D1a} is [A = 2.56, B = 1.38]. The Eq. 4 fit parameters for G_{M3} is [A = 2.14, B = 1.63] and G_{D1a} is [A = 2.06, B = 1.72]. Note that the Eq. 4 fit parameters differ from those found

from the related log plots in panel c. The binning of the binding data in the log plots causes an approximation error. b) Log plots used to derive Eqn 3. c) Log plots used to derive Eqn 4 as used Bally et al.[58] (the data has been binned).

Rather, N decays in an unusual logarithmic fashion with respect to t_{res}, as also noticed by norovirus binding kinetics studies [58, 59] and our recent work with parvovirus binding to transferrin receptors [102]. Alternative analytical models are generally lacking for multivalent binding systems and recent studies have begun to address this issue [58, 59, 62, 102, 120]. Here, we searched for an empirical model to describe the overall unbinding probability of the virus by testing various log plots between N and t_{res} until a linear relationship was found (**Fig. 10b and 10c**). Two possible fit equations for N vs t_{res} are provided (Eq. 3 and 4). Note that Eq. 4 mimics the approach used by Bally et al. [58], while Eq. 3 is developed by us and also describes the binding residence distribution of parvovirus binding to transferrin receptors [102].

Eq. 3 : empirical fit derived from **Fig 10b**

$N = N_0 \exp(B)\left(\ln\frac{t_{res}}{\Delta t}\right)^{-A}$ where Δt is a reference time interval $\leq t_{cutoff}$. We used Δt = 1s based on the time interval between images. Note that all equations here apply only when $t_{res} \geq t_{cutoff}$.

Eq. 4 : empirical fit derived from **Fig. 10c** and proposed by Bally et al [58]

$N = N_0\left[1-\frac{\exp(B)}{1-A}\left(t_{res}^{1-A}-t_0^{1-A}\right)\right]$ if $A \neq 1$

$N = N_0\left[1-\exp(B)\ln\frac{t_{res}}{t_0}\right]$ if $A = 1$

Unbinding rates are often characterized via an unbinding constant k_{off}, which in turn is related to binding force. Since Eq. 1 and 2 failed to fit our data, this suggests that the unbinding kinetics does not follow a constant k_{off} value, complicating matters. We thus assumed k_{off} is not a constant and could vary with t_{res}. To extract k_{off}, we equated the empirical fits with the 1st order dissociation equation ($dN/dt = -k_{off}t$) and solved for k_{off}. The resulting equations for k_{off} are shown as Eq. 5 or 6

Eq. 5: $k_{off}(t_{res})$ based on Eq. 3

$$k_{off}(t_{res}) = \frac{A}{t_{res}\ln\left(\frac{t_{res}}{\Delta t}\right)}$$

Eq. 6: $k_{off}(t_{res})$ based on Eq. 4

$$k_{off}(t_{res}) = \frac{\exp(B)t_{res}^{-A}}{1-\frac{\exp(B)}{1-A}\left(t_{res}^{1-A}-t_0^{1-A}\right)} \quad \text{if } A \neq 1$$

$$k_{off}(t_{res}) = \frac{\exp(B)t_{res}^{-1}}{1-\exp(B)\ln\frac{t_{res}}{t_0}} \quad \text{if } A = 1$$

Since k_{off} is a function of t_{res}, this would imply that the binding force changes depending on the contact time between the virus and receptor. This is in good agreement with recent work by H. Witt and coworkers showing that binding force of multivalent bonds does change with contact time [121]. For viruses, the general term for increasing binding force over time is adhesion-strengthening [99-101], which includes co-receptor binding, conformational changes of viral proteins, and multivalent binding due to receptor diffusion within the target bilayer. Since the HA proteins do not significantly change conformation upon binding [117] or under the neutral pH conditions used here, adhesion strengthening is thus most likely caused by multivalent binding of the virus to the tightly-packed, mobile SA receptors on the SLB. In support of this, the estimated number of glycolipids per contact area is ~90,

assuming a virus diameter is 150 nm, a lipid molecule occupies 0.61 nm^2 of the SLB [116], and the contact area is roughly 30% of the virus cross-sectional area based on cryo-EM pictures of virus-membrane contacts [122]Furthermore, the glycolipid mobility was confirmed by fluorescence recovery after photobleaching (FRAP) experiments.

A competing interpretation of our unbinding curves is that k_{off} spans a wide range of values due to a wide distribution of virus sizes and thus degree of multivalent binding. To make an empirical model under this interpretation, one would sum many exponential functions for 1:1 binding model that are multiplied by a weight function that reflection the virus size distribution. This approach would also assume multivalent bonds effectively act as a single bond with a stronger binding force. However, the virus distribution is narrow and morphology is uniform according to particle size and EM studies [35]. Additionally, AFM studies showed complex unbinding process [123] that would be inconsistent with the idea that multivalent bonds can be treated as a single bond. Overall, the interpretation that k_{off} varies with t_{res} because of adhesion-strengthening via multivalent binding is most likely to agree with the biology involved in this study. The remaining question is why does k_{off} approach infinity if we allow t_{res} to approach 0? Theoretically, this is because as t_{res} goes to 0, an elastic collision between virus and membrane will count as a binding event, and thus k_{off} will be substantially high to reflect a lack of binding force.

2.3.8. Bridging SPT and SPR data analysis

Since protein-ligand binding are currently often studied via ensemble assays such as SPR (Surface Plasmon Resonance) and QCM (Quartz Crystal Microbalance), we explain how to fit ensemble data using our empirical model from SPT data. Ensemble assays collect data on the net adsorbed mass on a surface over time, which would be

similar to the N vs t data from our SPT assay. However, unlike SPT assays, ensemble assays require two experimental procedures to decouple binding and unbinding kinetics, noted as the "association" and "dissociation" phases. The virus must be loaded during the association phase to observe both binding and unbinding, and then a virus-free buffer is loaded during the dissociation phase to observe mainly unbinding. The procedure often requires the virus to be subjected to a gentle hydrodynamic flow that could shear off very weakly bound viruses and affect the final data. Also, rebinding events that occur during that dissociation phase are difficult to completely filter out and could lead to disagreements between expected and actual unbinding curves [124].

With SPT, we can extract association and dissociation curves using stagnant conditions and without conducting a separate dissociation phase procedure, simply by filtering binding events that occur during the "dissociation phase" that is set at the image processing stage. To make SPR-like curves, we plot N vs t, but with few differences. N is now set to start at 0 at $t = 0$ by removing binding events that occurred at or before the first frame, and a dissociation phase session is defined to start after time $t_{diss} = ½\ t_{movie}$, in which new binding events that occurred after that are ignored (**Fig. 11**).

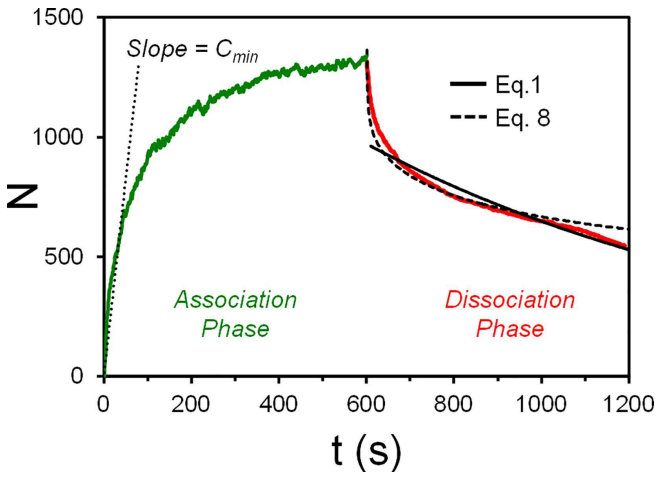

Figure 11. SPR-like curve assemble generated from SPT data for the purpose of comparing and contrasting the approaches. The fit parameters for Eq. 8 are A = 2.0, C = 47 (which is greater than C_{min} = 16.4). The fit parameters for Eq. 1 are N_0 = 971 and k_{off} = 0.001 s^{-1}).

The unbinding curve can be fitted using a modified form of Eq. 3, which the residence time t_{res} is converted into normal time t as shown in Eq. 7. Eq. 7 simply states that number of binding events remaining at $t > t_{diss}$ is the sum of the binding events that occurred at $t < t_{diss}$ and lasted until time t.

Eq. 7

$$N_{diss}(t) = \sum_{t'=0}^{t'=t_{diss}-\Delta t} \Delta t R_{on}(t') \exp(B) \left[\ln \frac{t-t'}{\Delta t} \right]^{-A} \quad \text{for } t \geq t_{diss}$$

Since ensemble assays do not yield $R_{on}(t)$ directly, an simplifying assumption must be made. We approximate $\Delta t R_{on}(t)$ as a constant, C, based on the N_+ vs t plots showing a fairly linear relation and constant slope R_{on} (**Fig. 7**) This yields the fit Eq. 8, which would be used if one were given SPR-like data without knowing exactly what $R_{on}(t)$ is.

Eq. 8

$$N_{diss}(t) = \sum_{t'=0}^{t'=t_{diss}-\Delta t} C \left[\ln \frac{t-t'}{\Delta t} \right]^{-A} \quad \text{for } t \geq t_{diss}$$

C is the number of binding events that occur on average within a time increment Δt. One could instead use a time-varying C fit parameter, $C(t)$, but it may lead to over-fitting issues. A lower bound value of C can be set based on the initial slope of

the N vs t curve during the association phase, denoted as C_{min}. Optimal fit parameters can be determined via an iterative search strategy. An example of how our adhesion-strengthening model (Eq. 8) performs against the standard 1:1 binding model (Eq 1) is shown in **fig. 11**. The exponential fit model failed to fit the steep drop in unbinding immediately after the dissociation phase start, whereas our empirical model fitted main features of the curve.

We assessed of the SPT binding assay platform, image restoration, and data analysis for use in virus-membrane binding studies. We developed an image restoration algorithm called STAWASP to enhance dim particle signal and improve SPT binding data quality. STAWASP restored particles that had a SNR as low as 1.1, and preserved appearance/disappearance time of particles with an SNR as low as 2.2. The image restoration enabled the SPT software to extract accurate binding residence curves when tracking particles lasting at least 5 frames. However, a small number of trajectories must still be manually corrected. Fully automated tracking without any error is currently not possible and is an active research area for machine-learning algorithms.

We explained data analysis strategies for X-31 binding to various glycolipids, and showed X-31 weakly binds to G_{M3} and to G_{D1a} ~28 times more frequently than to G_{M3}, despite both containing terminal sialic acid that should promote receptor binding

[71]. On the other hand, ensemble assays and cell infectivity assays had mixed results about whether or not the virus can bind to G_{M3} [64, 98]. The accessibility of SA appears highly restricted by the close proximity of it to the SLB lipid core.

The binding residence distribution curves show an interesting time-dependent k_{off}, which is unusual since k_{off} is often assumed to be a constant. The empirical model agrees with the interpretation that viruses increase their binding force to host membrane with longer contact time via an adhesion-strengthening process. For X-31 virus, adhesion-strengthening most likely occurs via multivalent bonds that form when mobile receptors in the SLBs are recruited to the virus, as opposed to any protein conformation changes. We provide a general strategy to apply our empirical model to fit ensemble assay unbinding data (Eq. 8) that feature a sharp decline in the dissociation curve, followed by a slow decay.

The combined image restoration and analysis tools developed here is easily extendible to other studies that involve imaging low-fluorescence particles binding stochastically with surfaces. We have recently applied these tools for tracking parvovirus binding to transferrin receptors [102], in which both were labeled with limited fluorophores and were difficult to observe without image restoration. Another example where this approach could be useful is for studying viruses that undergo membrane fusion upon receptor binding (such as parainfluenza). In such case, viruses

are usually labeled with a quenched membrane dye and would be difficult to track until membrane fusion and dye-dequenching occurs.

CHAPTER 3

Viral fusion efficacy of specific H3N2 influenza virus reassortant combinations at single-particle level

Hung-Lun Hsu[1], Jean K. Millet[2], Deirdre A. Costello[1], Gary R. Whittaker[2], and Susan Daniel[1]*

[1]School of Chemical and Biomolecular Engineering, Cornell University, Ithaca, NY.

[2]Department of Microbiology and Immunology, Cornell University, Ithaca, NY.

3.0. Acknowledgement

This chapter has been accepted for publication in Scientific Reports as "Viral fusion efficacy of specific H3N2 influenza virus reassortant combinations at single-particle level" [125]. Hung-Lun Hsu was the first author and co-authors include Jean K. Millet, Deirdre Costello, Gary R. Whittaker and Susan Daniel. H.L.H. and S.D. conceived and designed the study. H.L.H. performed experiments and carried out data analysis and interpretation of results. S.D. acknowledges funding from the National Science Foundation, grant CBET-1263701 in support of this work. G.R.W. acknowledges research funding from the National Institute of Allergy and Infectious Diseases, National Institutes of Health, Department of Health and Human Services, under CEIRS Contract No. HHSN272201400005C. J.K.M acknowledges Victor Tse for his help in obtaining influenza reagents.

3.1. Introduction

Influenza A viruses are enveloped, single-stranded, segmented, negative-sense RNA viruses that infect a wide variety of bird and mammalian species. The extensive and dynamic genetic diversity of influenza viruses is driven by the frequent generation of mutations due to the error-prone viral RNA polymerase and the process

of reassortment of gene segments from distinct viruses. Seasonal human influenza epidemics result in acute respiratory infections that circulate worldwide and cause up to 500,000 deaths each year [126]. Moreover, although they are rare, human influenza pandemics can occur when novel subtypes of influenza viruses emerge through genetic mutations and reassortment. In these situations, high transmissibility and pathogenicity leads to elevated human infections and deaths, as observed during the 1918 pandemic that led to an estimated 50 million deaths worldwide [127, 128]. The 1957 and 1968 pandemics, caused by the reassortment of avian and human viruses, and more recently, the 2009 pandemic, caused by a triple reassortant between avian, swine, and human viruses highlight the importance of the gene reassortment process in generating influenza virus strains that exhibit markedly altered tropism, pathogenicity, and interspecies transmission characteristics [129, 130].

Influenza A viruses require hemagglutinin (HA) and neuraminidase (NA) envelope glycoproteins for cell entry and egress, respectively. HA is a trimeric membrane-embedded glycoprotein that is a critical determinant of host tropism, and mediates both binding to host cell surface sialic acid receptors and fusion of viral and host cell membranes. Because of its crucial role in governing cell entry, tissue and host tropism, HA is also a key factor in regulating viral pathogenicity. NA protein is a tetramer on the surface of virions and is responsible for catalyzing cleavage of terminal sialic acids from HA [23, 24]. NA's functional role is critical for the release of progeny viral particles from infected cells at late stages of the infection cycle [25], and prevents virus from binding to the mucus overlying the human airway epithelium [26]. Influenza A viruses are divided into subtypes based on antigenic and amino acid sequence differences of the HA and NA surface glycoproteins, each composed of 18 and 11 known subtypes, respectively. While different HA and NA combinations are

found in circulating influenza viruses, aquatic birds can be infected by most subtypes, while humans are known to be infected by three main subtypes: H1N1, H2N2, and H3N2 [27]. The human H2N2 subtype is not currently circulating, but was responsible for the 1957 pandemic [28]. The avian H5N1 and H9N2 subtypes have been recognized for their pandemic potential in the human population [29]. The transition of receptor usage from avian-like α2,3-linked to human-like α2,6-linked sialic acids represents a critical step for avian viruses to acquire efficient replication and transmission capabilities in humans. Furthermore, understanding the effects of switching combinations of gene segments that occur during reassortment, in particular those encoding HA and NA, is critical for uncovering the basis of emergence of influenza viruses with increased pathogenicity and for pandemic preparedness.

During influenza virus entry, which occurs through the endocytic pathway, conformational changes of the HA are critical for virus fusion to occur. HA is a type I transmembrane protein and represents a prototypical class I viral fusion protein that has been widely studied both structurally and functionally. HA is initially synthesized as an uncleaved precursor, HA_0, which is proteolytically processed by host cell proteases into two subunits, HA_1 and HA_2, linked by two disulfide bonds. The HA_1 subunit contains a globular domain with residues responsible for binding to sialic acids, while the core of the fusion machinery, the hydrophobic fusion peptide, is found within the membrane anchored HA_2 subunit [20, 33]. The proteolytic cleavage event is critical for activating the HA, as it allows for exposure of the fusion peptide. In the late endosome, the pH drops from pH 6.5-6 to pH 5-4.5 causing the HA_2 fusion domain to undergo major conformational changes exposing the fusion peptide and enabling it to be inserted into the target endosomal membrane. HA_2 then refolds, and pulls viral and endosomal membranes together, allowing for hemifusion to occur and

ultimately leading to the opening of the fusion pore and release of the viral genome [17, 34]. In previous studies, we and others have successfully applied a single-particle tracking (SPT) methodology combining total internal reflection microscopy (TIRFM), microfluidics, and supported lipid bilayers to study influenza HA-mediated fusion kinetics using native viruses or HA-pseudotyped viral particles [35-38].

While influenza virus fusion has been well studied, including using the SPT approach, the influence of NA on HA fusion function is less clear. In particular, the comparison of different HA-NA pairings has not been well characterized in the context of HA-mediated fusion. Here, using SPT and a vesicular stomatitis virus (VSV)-based pseudotyping system, we investigated how co-incorporation of NA with HA in viral particles affects HA-mediated fusion kinetics. The VSV-based pseudotyping approach allowed us to focus specifically on the effects of HA-NA pairings. We examined the effects of incorporation of the H3 HA and N2 NA of the prototypical X-31 strain and compared them with authentic X-31 influenza virus fusion kinetics. In addition, to model reassortment of N2 NA, we studied how co-incorporation of heterologous human (H2N2 Japan) or avian (H9N2 MS96) N2 proteins impacts H3 HA-mediated fusion kinetics. The N2 NA gene of the H3N2 (X-31) subtype is genetically more closely related to the one from the H2N2 (Japan) subtype (94.5% amino acid identity) than the one from the H9N2 (MS96) subtype (90.5% identity, with 84 amino acid C-terminal deletion) (**fig. 12**). We show that co-incorporation in pseudotyped particles of influenza X-31 H3 and N2 allows higher hemifusion kinetics than particles incorporating only H3. Further, the influenza X-31 H3 and N2 pseudotyped particles exhibited fusion kinetics that closely matched the ones observed for authentic X-31 virus. We also demonstrated that co-incorporation of X-31 H3 with heterologous N2 from the human H2N2 (Japan) or from the avian

H9N2 (MS96) are associated with markedly decreased fusion kinetics, results that were consistent with viral phylogenetic relationships, suggesting that even within a given subtype there is some degree of constraint imposed by HA-NA pairings with respect to HA-mediated function. Finally, we show that the differences in hemifusion kinetics we observed could be attributed to changes in relative incorporation of HA and NA in viral pseudotyped particles.

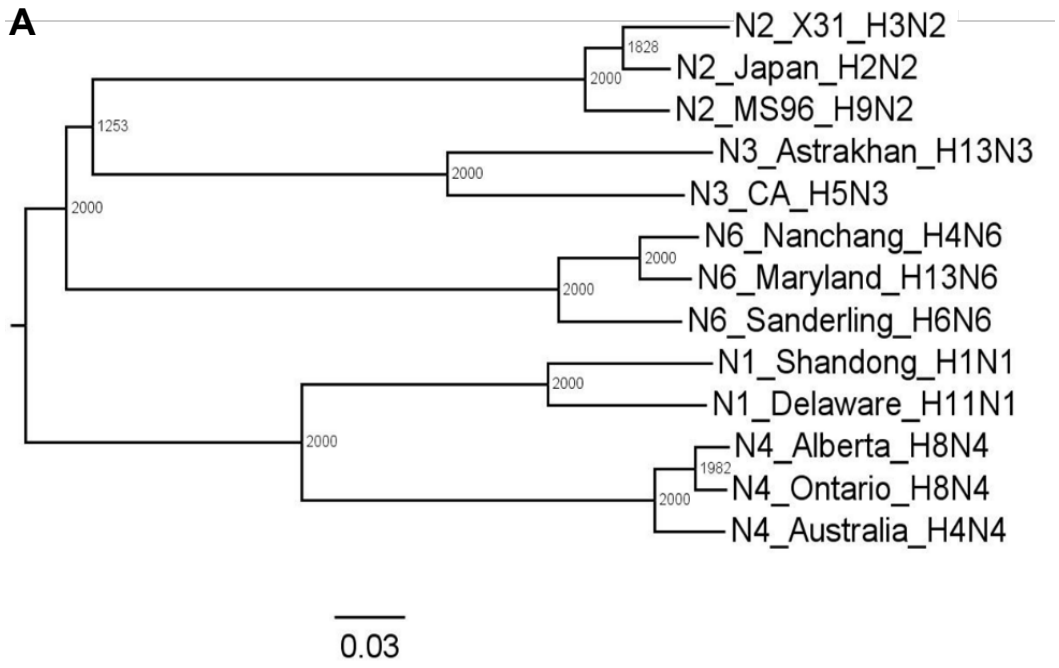

B

```
                1                                                                                                   10
N2_Japan_H2N2   MNPNQKIITIGSVSLTIATVCFLMQIAILATTVTLHFKQHECDSPASNQVMPCEPIIIERNITEIVYLNNTTIEKEICPEVVEYRNWSKPQCQITGFAP
N2_MS96_H9N2                                          N  SI S    V                        L  K
N2_X31_H3N2                                 V         Y                                   K

                101                                                                                                 20
N2_Japan_H2N2   SKDNPIRLSGGGDIWVTREPYVSCDPGKCYQFALGQGTTLDNKHSNGTIHDRIPHRTLLMNELGVPFHLGTKQVCVAWSSSSCHDGKAWLHVCVTGDDR
N2_MS96_H9N2        S    A  S           SSD                                                 I                S
N2_X31_H3N2         S    A               H                    D                         R   I                I    K

                201                                                                                                 30
N2_Japan_H2N2   ATASFIYDGRLVDSIGSWSQNILRTQESECVCINGTCTVVMTDGSASGRADTRILFIKEGKIVHIGPLSGSAQHIEECSCYPRYPDVRCICRDNWKGSN
N2_MS96_H9N2            M                                                       S                      V
N2_X31_H3N2                                                                E  E    S        V          G

                301                                                                                                 40
N2_Japan_H2N2   PVIDINMEDYSIDSSYVCSGLVGDTPRNDDSSSNSNCRDPNNERGNPGVKGWAFDNGDDVWMGRTISKDLRSGYETFKVIGGWSTPNSKSQVNRQVIVD
N2_MS96_H9N2     I N   A H                   G      K                Y N           S       R     T A
N2_X31_H3N2        V                           R       N       Q                                  LVVGP --------------

                401                                                 469
N2_Japan_H2N2   NNWSGYSGIFSVEGKSCINRCFYVELIRGRPQETRVWWTSNSIVVFCGTSGTYGTGSWPDGANINFMPI
N2_MS96_H9N2
N2_X31_H3N2     ---------------------------------------------------------------------
```

Figure 12. (A) Phylogeny of influenza NA genes, including N2 genes from

A/Aichi/68-X-31(H3N2), A/Japan/305/57 (H2N2) and A/chicken/Korea/MS96/96 (H9N2). The phylogenetic tree was generated using the NA amino acid sequences of isolated influenza A viruses and with alignments performed with ClustalX 2.1 (displayed with FigTree) with the Neighbor-Joining method and bootstrap values calculated from 2000 trees. Scale bar represents estimated number of substitutions per site. Numbers at nodes represent boot strap values. (B) Amino acid sequence alignment of influenza A N2. Sequence of A/Aichi/68-X-31(H3N2), A/Japan/305/57 (H2N2) and A/chicken/Korea/MS96/96 (H9N2). Residues identical to N2 (Japan) are left blank. Numbering is based on the N2 (Japan) sequence. The alignment was generated using ClustalW in DNASTAR.

3.2. Materials and methods

3.2.1. Cells, plasmids, and viruses. Baby hamster kidney-21 (BHK-21) cells and Madin-Darby canine kidney (MDCK) cells were obtained from the American Type Culture Collection (ATCC, Manassas, VA) and grown in Dulbecco's modified Eagle medium (DMEM, CellGro), supplemented with 10% fetal bovine serum (Gibco), 1% penicillin and 10 μg/mL streptomycin (CellGro), 1% HEPES buffer (CellGro). The cells were cultured in a 37 °C, 5% CO_2 incubator.

The plasmids pCAGGS-H3/X-31, pCAGGS-N2/X-31, pCAGGS-N2/MS96, pCAGGS-N2/Japan, pCAGGS-VSVG and pCAGGS-empty were used to transfect BHK-21 cells. pCAGGS-H3/X-31 and pCSAGGS-N2/X-31 encode the hemagglutinin and neuraminidase of influenza virus X-31, respectively. pCAGGS-N2/MS96 encodes the neuraminidase of influenza virus MS96 (H9N2), pCAGGS-N2/Japan encodes the neuraminidase of influenza virus Japan (H2N2), and pCAGGS-VSVG encodes the glycoprotein of vesicular stomatitis virus. The

pCAGGS vector serves as the empty vector control. Influenza X-31 A/Aichi/68 H3N2 (Charles River, Wilmington, MA) (live virus) was used as a reference case in the study.

The VSV *G-VSVΔG is a recombinant virus that harbors a genome in which the glycoprotein gene is replaced by the green fluorescence protein (GFP) reporter gene, and is a generous gift from Michael Whitt from University of Tennessee.

3.2.2. Preparation of influenza pseudoparticles[131, 132]. 9×10^5 cells BHK-21 were seeded in 10 cm petri dishes (Corning), and incubated for 24 h. BHK-21 cells were transfected by a mixture containing 36 μL of lipofectamine 2000 transfection reagent (Thermo Fisher) and 12 μg of plasmid DNA (6 μg of HA- and NA-encoding plasmids DNA) for each plate, and incubated for 24 h. Next, transfected BHK-21 cells were inoculated with VSV *G-VSVΔG in RPMI medium (10.4 g RPMI powder, 26.7 mL BSA 7.5% liquid, 25 mL 1 M HEPES, 1 L H_2O), and incubated for 2 h at 37°C with rocking. Unbound viruses were washed out with DPBS (Dulbecco's phosphate-buffered saline), and incubated for 24 h at 37°C with DMEM growth medium. For HA only case, 0.25 units of exogenous neuraminidase from *C. welchii* (Sigma-aldrich) was added to the plate to facilitate viral particle release. The supernatants, which contain pseudotyped particles, were collected after several gentle taps on the walls of petri dishes to help the release of particles. The supernatants were ultracentrifuged in a Ti45 rotor at 35,000 rpm for 120 min. The supernatants were discarded, and pellets were resuspended in 3 μg/ml trypsin and incubated for 30 min at 37 °C to activate HA. The trypsin-treated viral solutions were then aliquoted for storage at -80°C.

3.2.3. Western blotting. Pseudotyped particles were concentrated using an ultracentrifuge at 20,000 rpm in a TiSW28 rotor (Beckman-Coulter) for 2 h at 4°C.

The pellets were resuspended in 30 μL of 3 μg/mL trypsin EDTA (Thermo Fisher Scientific) solution, and put in 37°C water bath for 15 min. The samples were then analyzed by Western blot using goat anti-A/HongKong/1/68 (H3) (NR-3118, BEI resources), goat anti-A/shorebird/Delaware/127/1997(N2) (NR-670, BEI resources) and mouse anti-VSV-M antibodies (Kerafast) followed by incubation with HRP-conjugated rabbit anti-goat IgG (Life Technologies) and HRP-conjugated goat anti-mouse IgG (Life Technologies). All Western blots were visualized and analyzed using a Chemidoc XRS+ system with Image Lab image capture software (BioRad). The Image Lab software was used to quantify intensities of bands using low sensitivity setting. The software detects the bands by the signal contrast between band and background. We note that all bands have only been adjusted in contrast and brightness in the Image Lab software. The software shows the original signal intensities of the bands.

3.2.4. Immunofluorescence assay. 5×10^5 cells BHK-21 cells were seeded in 8-well glass slides (Millipore). After 24 h, BHK-21 cells were transfected by a mixture containing 0.75 μL of lipofectamine 2000 transfection reagent (Thermo Fisher Scientific) and 1 μg of plasmid DNA (500 ng of HA- and NA-encoding plasmid DNA) for each well, and incubated for 24 h. Transfected cells were then fixed with 4% paraformaldehyde (PFA) (Thermo Fisher Scientific) for 15 min and PFA was then quenched in 50 mM ammonium chloride (NH_4Cl) for 15 min. For the permeabilized condition, 0.1% Triton X-100 was added to each well for 5 min at 4°C and washed three times with DPBS. The cells then were blocked with 5% normal goat serum for 45 min, and labeled with monoclonal mouse anti-HA antibody (Sigma-Aldrich), and goat anti-A/shorebird/Delaware/127/1997(N2) (NR-670, BEI resources), followed by labeling Alexa Fluor 568-conjugated goat anti-mouse

antibody (Thermo Fisher Scientific) and 488-conjugated chicken anti-goat antibody (Thermo Fisher Scientific). The nuclei were labeled with DAPI (Southern Biotech). Microscopy images were acquired using inverted microscope (Carl Zeiss) with a 63x objective.

3.2.5. Preparation of liposomes. Liposomes used in this study contain a 4:4:2:0.5:0.01 molar ratio of 1,2,dioleoyl-sn-glycero-3-phosphocholine (DOPC), 1-oleoyl-2-palmitoyl-sn-glycero-3-phosphocholine (POPC), cholesterol, total ganglioside extract (TGE) and Oregon green DHPE, based on compositions found in previous studies that provide comparative data[37, 69]. The lipids were purchased from Avanti Polar Lipids (Alabster, AL), and Oregon green DHPE was purchased from Molecular Probes, Eugene, OR. To form liposomes, all components were dissolved and mixed in biotechnology grade chloroform (Sigma-Aldrich) in a glass vial. The bulk solvent was first removed by blowing high purity nitrogen and the solution was placed in a desiccator under vacuum for 3 h to ensure complete evaporation of the solvent. GPMV buffer (50 mM Hepes, 150 mM NaCl, 2 mM $CaCl_2$, pH 7.4) was then added to the vial to re-suspend the dried lipid film to create a 5 mg/mL solution. Liposomes were then extruded ten times through a 100 nm pore size polycarbonate filter (Whatman Nucleopore), and five times through a 50 nm pore size filter.

3.2.6. Fluorescent labeling of viruses. Both influenza viruses and the influenza pseudoparticles were labeled with the lipophilic fluorophores: octadecylrhodamine B chloride (R18), a red-emitting fluorophore, at a sufficient concentration and sonicated 30 min to quench fluorescence.

3.2.7. NA inhibition assay. The neuraminidase inhibitor N-Acetyl-2,3-dehydro-2-deoxyneuraminic acid (NADNA) (Sigma-Aldrich) was

dissolved in DI water to 2 mg/mL. 1 μL of NADNA was mixed with 6 μL of influenza X-31 virus and incubated at 37 °C for 1 h. The NADNA-treated virus was labeled as described in the labeling procedure and fusion carried out at selected triggering pH's.

3.2.8. Preparation of glass surfaces for supported bilayers. To produce biomimetic planar supported lipid bilayer, researchers have developed various methods[48, 133, 134]. Here, self-assembling of lipid vesicles was performed to form a host cell-mimetic membrane bilayer, and the procedure is described as follows. Glass microscope coverslips (25 mm × 25 mm; No. 1.5) from VWR were cleaned in piranha solution (45 ml 50% hydrogen peroxide and 105 ml 70% sulfuric acid) for 10 min then rinsed 30 min with deionized water with a minimum resistance of 18.2 MΩ cm (Siemens Purelab Ultra water purification system). Glass slides were flushed by deionized water again and dried by a stream of ultra-pure nitrogen gas prior to plasma cleaning.

3.2.9. Fabrication of microfluidic devices. The generation of microchannel silicon mold developed using soft lithography was published previously [36, 48, 69]. The pattern contains six trenches 70 μm deep, 135 μm wide and 1.5 cm long with 100 μm spacing between each channel. Microfluidic devices were formed using polydimethylsiloxane (PDMS) in a molding process. The silicon mold was coated with chlorotrimethylsilane (Sigma-Aldrich) via vapor deposition to facilitate the release of cured PDMS. A 10:1 (elastomer:crosslinker) mixture of Sylgard 184 (Dow Corning) was mixed and degassed to remove bubbles before pouring on the silicon mold. The PDMS then was crosslinked in the oven for 3 h at 80 °C. Both the piranha cleaned glass cover slip and the microfluidic device were assembled by oxygen plasma bonding. They were first treated with oxygen plasma using a Harrick Plasma

Cleaner (Model # PDC-32G, Ithaca, NY) at a pressure of 750 millitorr on the "high" setting for 15 s. The two pieces were then pressed together gently to form a tight bond and annealing was performed at 80 °C for 15 min.

3.2.10. Forming supported bilayers in microfluidic channels. A 10% dilute solution of liposomes was drawn into the microchannel at a flow rate of 100 μL/min for 90 s and incubated on the glass substrates for 2 h. The microchannel was then rinsed with the GPMV buffer at 100 μL/min for 2 min. To heal defects in membranes, a 5% dilute solution of liposomes was drawn into the microchannel at 10 μL/min for 5 min. Before loading virus-containing solutions, channels were rinsed again with GPMV buffer at 100 μL/min for 2 min.

3.2.11. TIRF microscope configuration. Single-particle fusion assays were operated using total internal reflection fluorescence microscopy (TIRFM) with an inverted Zeiss Axio Observer.Z1 with an α Plan-Apochromat 100× oil immersion objective with a numerical aperture (NA) of 1.46. Index-matching immersion oil (Carl Zeiss, Inc.) was added to the glass coverslip of the microfluidic device and the objective. Two lasers with 561 nm and 488 nm excitation wavelengths were used to simultaneously excite red and green fluorophores under this setting. The Laser TIRF 3 slider (Carl Zeiss, Inc.) was used to control the angles of incidence in the optical pathway. Exceeding the critical angle (~62°) generates total internal reflection due to the difference in refractive indices of the two different substances (glass and aqueous buffer), and further creates an evanescent wave that penetrates about 100 nm into the aqueous buffer. Because virion binding and fusion occurs within a ~100 nm thick region, the evanescent wave can excite fluorophores near the membrane and eliminate the background noise from viruses floating in the bulk aqueous phase.

3.2.12. Image processing. Membrane fusion events were analyzed using both ImageJ

(NIH) and MATLAB (Mathworks). Each fusion event was manually selected in ImageJ with Time series analyzer V2.0 plugin, and the intensity of each event in 4 × 4 pixels was averaged and saved with the corresponding time as a table. The data was then processed by MATLAB to calculate the fusion lag time and used to fit the lag times into a gamma-distribution equation to retrieve the fusion rate constant [37].

3.3. Results

3.3.1. Influenza pseudotyped particle production and infectivity assays. To assess the effect of HA-NA pairings on infectivity of influenza pseudotyped viruses, six types of pseudotyped particles were produced: HA only pseudoparticles ($H3_{X\text{-}31}$), native matching pseudoparticles ($H3_{X\text{-}31}/N2_{X\text{-}31}$), human:human mismatching pseudoparticles ($H3_{X\text{-}31}/N2_{Japan}$), human:avian mismatching pseudoparticles ($H3_{X\text{-}31}/N2_{MS96}$), and two control pseudovirions, VSV-Δenv and VSV-G.

The pseudovirions were then used to infect Madin-Darby canine kidney epithelial (MDCK) cells, with infection confirmed by the green fluorescence signals produced by the infected cells. In all cases, MDCK cells were evenly seeded at 2×10^5 cells/cm^2, so more GFP-positive cells indicate that pseudovirions had higher infectivity **(Fig. 13)**. VSV-Δenv refers to particles without envelope glycoproteins (negative control case) and VSV-G are particles harboring the VSV G surface fusion protein (positive control case). The results of the infectivity assays show that VSV-$H3_{X\text{-}31}/N2_{X\text{-}31}$, VSV-$H3_{X\text{-}31}/N2_{Japan}$ VSV-$H3_{X\text{-}31}/N2_{MS96}$ and VSV-$H3_{X\text{-}31}$ particles are infectious, as GFP-positive cells were observed in all these cases. However, among these, infectivity levels varied based on the number of GFP-positive cells observed. To better understand the basis for the differences in infectivity observed, we carried out single-particle fusion assays to determine if there were

differences in cell entry behavior among these particles.

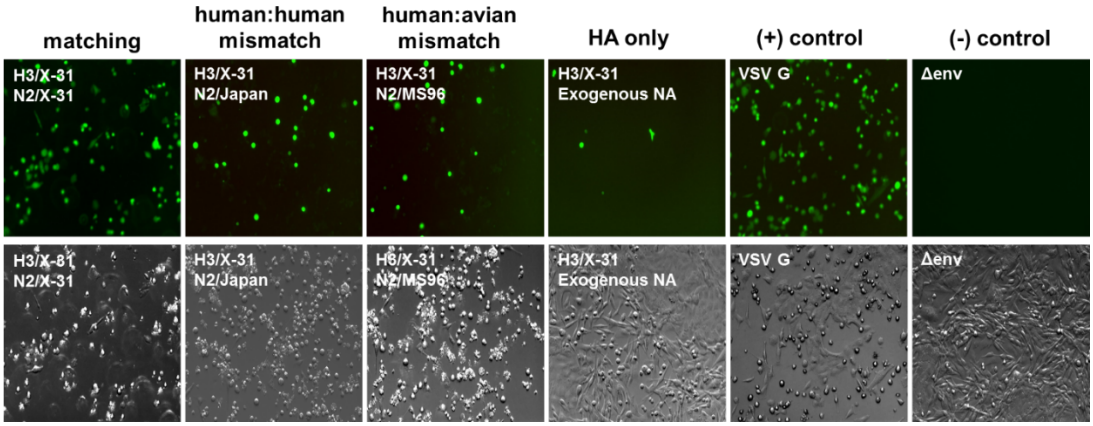

Figure 13. Top row: MDCK cell infectivity assay of influenza pseudotyped particles $H3_{X\text{-}31}/N2_{X\text{-}31}$, $H3_{X\text{-}31}/N2_{Japan}$, $H3_{X\text{-}31}/N2_{MS96}$, $H3_{X\text{-}31,}$ VSV and Δenv. Green fluorescence indicates infection of the cell. Bottom row: bright field images of the images above.

3.3.2. Single-virion fusion experiments. To monitor virus entry and fusion at the single particle level, individual virion fusion measurements were performed using total internal reflection fluorescence (TIRF) microscopy. Microfluidic channels were coated with supported lipid bilayers (SLB) (**Fig. 14**). The SLB contained a mixture of zwitterionic lipids, cholesterol, total ganglioside extract (TGE), and Oregon green DHPE[37, 69]. TGE contains glycolipids that possess sialic acid groups necessary for influenza binding. Oregon green DHPE is a pH-sensitive fluorophore embedded in the SLB that drastically decreases in emission intensity when exposed to an acidic solution, marking the time when HA-activating acidification occurs in the microfluidic channel. The fluidity of SLBs was confirmed by using fluorescence recovery after photobleaching (FRAP) performed prior to the fusion assay. Membrane fluidity of SLBs can affect the hemifusion kinetics and is thus a crucial parameter to control when comparing the rate of fusion between assays[35, 69]. The average

diffusion coefficient for three samples was determined to be 0.847 ± 0.03 $\mu m^2/s$ which corresponds to the value measured in a previous study[69].

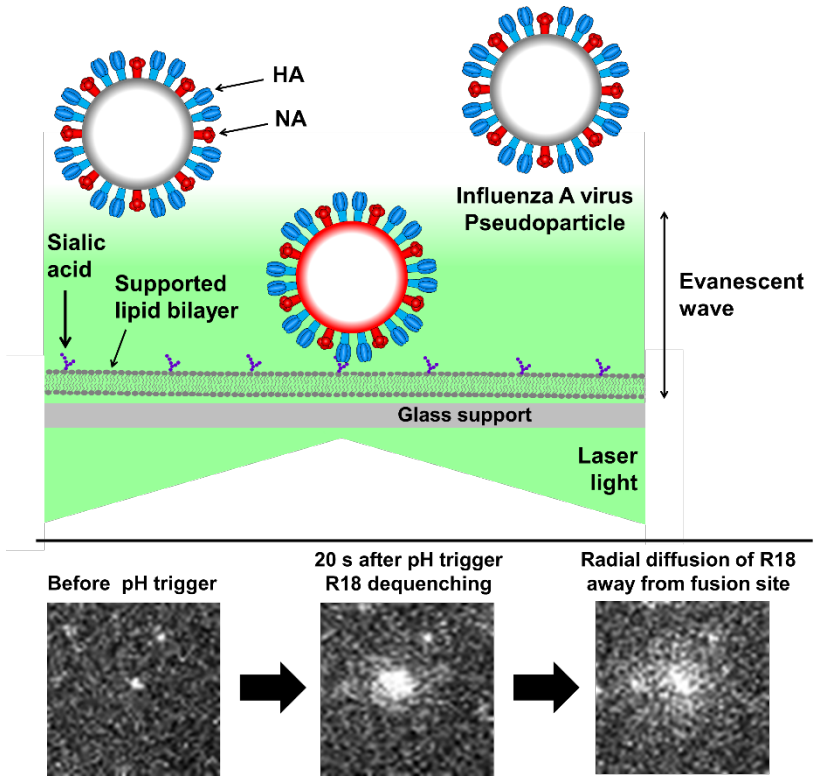

Figure 14. Top illustration: Single-particle fusion assay performed with total internal reflection fluorescence microscope (TIRFM). Three pseudovirus particles are shown containing HA (blue) and NA (red) in their membrane envelopes. The center virus is bound to sialic acid (purple) in the supported lipid bilayer (gray) localizing the virus in the ~100 nm evanescent wave (green) that results from the total internal reflection of laser light at the glass-buffer interface. The evanescent light excites the fluorophores in the viral membrane, emitting in red. Viruses outside the evanescent field are not excited, and thus no red emission is observed. Note that a membrane-bound pH sensor (Oregon green DHPE) is not shown for clarity. Bottom row: images of a native X-31 virus labeled with R18 fusing with a supported bilayer

after triggering with pH 4.5.

HA-mediated membrane fusion is a multistep reaction that begins with hemifusion (the merging of the outermost leaflets of the host and viral membranes). Hemifusion commences when hemagglutinin is exposed to an acidic solution, which triggers major conformational changes of the viral envelope protein. Pseudovirions were treated with TPCK-trypsin for 15 min at 37°C in order to cleave the precursor HA_0 into HA_1 and HA_2, which is an essential activating step for successful membrane fusion to occur[20]. To track the fusion reaction and its intermediate steps, viral membranes were labeled with quenched amount of octadecyl rhodamine B chloride (R18). Upon membrane hemifusion, the membrane dye that originated in the viral envelope spreads into the SLB and dequenches as the fluorophores diffuse radially away from the hemifusion site, an event that is easily detected by a CCD camera (**Fig. 14**, bottom). Fusion experiments were carried out within a channel for 3-4 min at a data collection rate of 10 frames/s.

The hemifusion lag time is defined as the interval of time between the pH drop and hemifusion for each individual virion. Within the field of view, hemifusion is marked by individual dequenching events. The lag time distributions are fit to the cumulative gamma distribution:

$$p_H = \int_0^1 \frac{k_H^N t^{N-1}}{\Gamma(N)} e^{-k_H t}\, dt$$

where k_H is the hemifusion or pore formation rate constant, t is lag time, and N is an additional fit parameter reporting the number of rate-limiting steps. In the context of fusion kinetics, N is often correlated to the number of HA trimers that must act concertedly to initiate fusion[37], but is mathematically defined as the number of steps in the pathway. The gamma distribution is appropriate here, as fusion events occur stochastically and independently of each other. Each fusion event is a multistep

process, with each step in the process being described by a Poisson process. The gamma distribution is a convolution of multistep Poisson processes.

We characterized the hemifusion behavior of native influenza X-31, native-matching pseudoparticles ($H3_{X\text{-}31}/N2_{X\text{-}31}$), human:human mismatching pseudoparticles ($H3_{X\text{-}31}/N2_{MS96}$), human:avian mismatching pseudoparticles ($H3_{X\text{-}31}/N2_{Japan}$), and HA only pseudoparticles ($H3_{X\text{-}31}$) over a range of initiation pHs. **Figure 15** illustrates hemifusion rates by showing the cumulative gamma distribution data at the upper and lower limits of HA conformational change activation, pH 4.5 and pH 5.1, respectively. At pH 4.5 and 5.1, the rate of hemifusion of native influenza X-31 and matching pseudoparticles ($H3_{X\text{-}31}/N2_{X\text{-}31}$) are similar and are distinctively faster than that of other pseudoviruses, including the HA only pseudoparticles ($H3_{X\text{-}31}$).

The hemifusion kinetics over a range of initiation pHs between pH 4.0 to pH 5.1 were determined (**Fig. 15**). The hemifusion rate constants of samples at the tested pH in ascending order are HA only pseudopaticles ($H3_{X\text{-}31}$), mismatching pseudoparticles ($H3_{X\text{-}31}/N2_{MS96}$), mismatching pseudoparticles ($H3_{X\text{-}31}/N2_{Japan}$), matching pseudoparticles ($H3_{X\text{-}31}/N2_{X\text{-}31}$) and native influenza X-31. The hemifusion rate constants of matching pseudoparticles ($H3_{X\text{-}31}/N2_{X\text{-}31}$) and native influenza X-31 are similar at all initiation pHs. The hemifusion kinetics of native influenza viruses is strongly dependent on pH as well as matching pseudoparticles ($H3_{X\text{-}31}/N2_{X\text{-}31}$). The rate of hemifusion increases almost linearly from pH 5.3 to 4.7 and reaches a plateau at the "fastest" fusion pH. It is not evident from the data shown in **figure 16** that mismatching pseudotyped particles ($H3_{X\text{-}31}/N2_{MS96}$) exhibits the same dependence on pH. While the maximum rate of fusion of mismatching pseudovirions ($H3_{X\text{-}31}/N2_{MS96}$) also occurs at pH 4.7, the error associated with the parameter falls within the rate

constant values associated with adjacent pHs, thus it can be concluded that the hemifusion kinetics of mismatching pseudotyped particle ($H3_{X\text{-}31}/N2_{MS96}$) is triggered by acidification but rate independent of triggering pH. pH independent influenza fusion rate is not unprecedented, as we also observed a similar flat trend for a clinical isolate, A/Brisbane/2007/H3N2 [35].

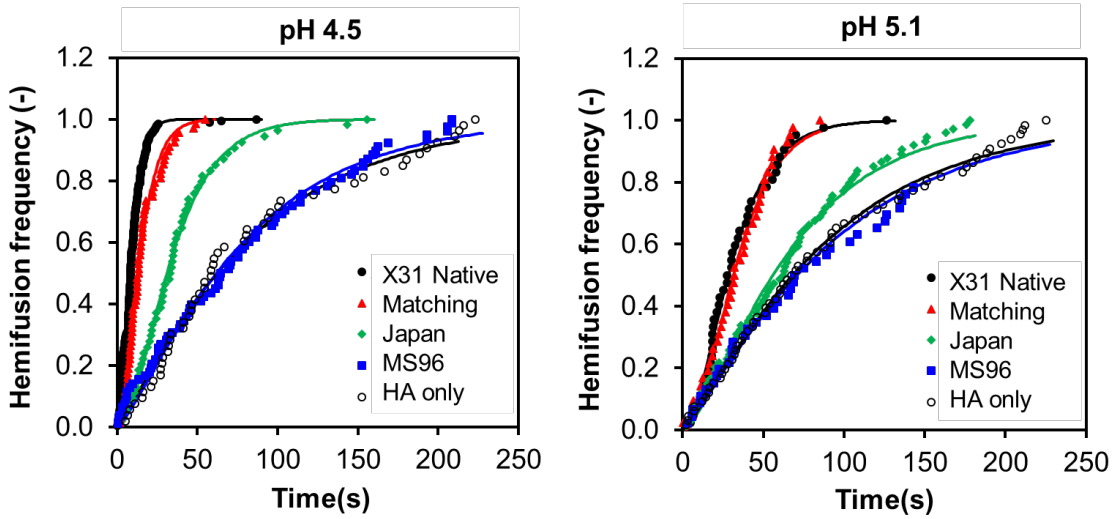

Figure 15. Cumulative distribution function plot of different batches of native influenza X-31, matching pseudoparticles ($H3_{X\text{-}31}/N2_{X\text{-}31}$), mismatching pseudoparticles ($H3_{X\text{-}31}/N2_{Japan}$), mismatching pseudoparticles ($H3_{X\text{-}31}/N2_{MS96}$), and HA only pseudopaticles ($H3_{X\text{-}31}$) at pH 4.5 and 5.1.

The number of HA trimers (*N*) required for pseudotyped particle fusion was also calculated and compared with that of native influenza X-31 (**Fig. 16**). At high, physiological pH values, *N* values for influenza virus X-31 and matching pseudovirions ($H3_{X\text{-}31}/N2_{X\text{-}31}$) are found to be approximately 3, while the *N* values of human:human mismatching pseudovirions ($H3_{X\text{-}31}/N2_{Japan}$) vary between 1.5 to 3. A few possible interpretations of this variation include a change in the number of HA contributing to bending the membrane over this range, but this is hard to rationalize with our understanding of the fusion process. It may reflect that other processes are

dominating the kinetics in this regime, but it also seems at odds with what we know about hemifusion, that there would be such oscillations among rate limiting steps within this range. What seems most likely to us is considering that N is an exponential fit parameter; it gives rise to an inherent sensitivity in data fluctuations and thus produces a wider range of output values. Considering that the authentic X-31 does not have such variation in its fits for N, we may attribute these fluctuations as resulting from variations among the particles themselves: the HA incorporation in VSV pseudotypes are lower than the authentic influenza X-31, or that the morphology of the rhabdoviral pseudovirions are bullet-shaped compared to the spherical morphology of authentic X-31. For human:avian mismatching pseudotyped particles ($H3_{X\text{-}31}/N2_{MS96}$) and HA-only pseudopaticles ($H3_{X\text{-}31}$), N is consistently closer to unity as a function of pH. These findings suggest that only one HA trimer may be needed for mismatching pseudotyped particle fusion. However, since hemifusion is a multi-step process, an N value equal to 1 more likely indicates that another process less dependent on viral particle properties, e.g. the merging of membranes, may occur so slowly that kinetics are dominated by this single step, thus resulting in a gamma distribution where $N = 1$ [135].

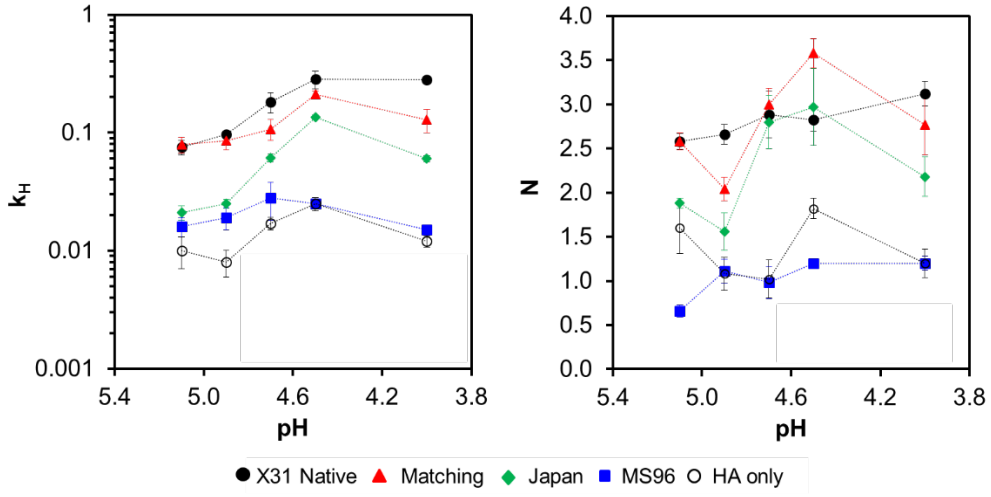

Figure 16. HA hemifusion kinetics. Hemifusion rate constant, k_H and number of HA

trimers, *N*, as a function of pH for native influenza X-31, matching pseudoparticles ($H3_{X\text{-}31}/N2_{X\text{-}31}$), mismatching pseudoparticles ($H3_{X\text{-}31}/N2_{Japan}$), mismatching pseudoparticles ($H3_{X\text{-}31}/N2_{MS96}$) and HA only pseudoparticles ($H3_{X\text{-}31}$). The error bars of the data represent the standard deviation of at least three separate experiments. Dashed lines serve to guide the eye only.

3.3.3. Incorporation of HA and NA in pseudovirions. Previous work done by Bosch et al., has demonstrated that the presence and activity of NA was key to HA incorporation into lentiviral-based pseudotyped particles and their release from the cell surface [136]. In order to understand better the differences in fusion kinetics observed among matching ($H3_{X\text{-}31}/N2_{X\text{-}31}$) and mismatching pseudovirions, quantitative Western blots were performed to determine the relative protein incorporation of HA in particles. The internal VSV matrix protein (M protein, ~37 kDa) was used to normalize band intensities of HA. The three hemagglutinin bands include one uncleaved HA (HA_0) at 75 kDa and the cleaved HA (HA_1 and HA_2) at 50 kDa and 25 kDa, respectively (**Fig. 17**). HA_1 bands were normalized to corresponding VSV M bands to calculate the cleaved proportion of HA protein in different samples. The normalized bands were normalized again to the HA_1 bands of HA only pseudoparticles ($H3_{X\text{-}31}$) so the values could be compared between different HA-NA combinations. HA band intensities of human:avian mismatching pseudoparticles ($H3_{X\text{-}31}/N2_{MS96}$) and human:human mismatching pseudoparticles ($H3_{X\text{-}31}/N2_{Japan}$) are ~45% and ~20% lower than X:31 matching pseudoparticles ($H3_{X\text{-}31}/N2_{X\text{-}31}$), respectively. Considering that a successful viral fusion event may require at least three HA trimers, a lower density of HA trimers on mismatching pseudoparticles may explain the slower fusion rate we have measured.

N2 bands (~55 kDa) were detected by Western blot (except in HA only pseudoparticles ($H3_{X-31}$)). Three N2 bands were normalized to corresponding VSV M bands to calculate the NA density on different samples. The normalized bands were normalized again to the matching pseudovirions ($H3_{X-31}/N2_{X-31}$), and the quantitative analysis indicated that normalized N2 bands intensity were similar in the three pseudoparticle types containing it.

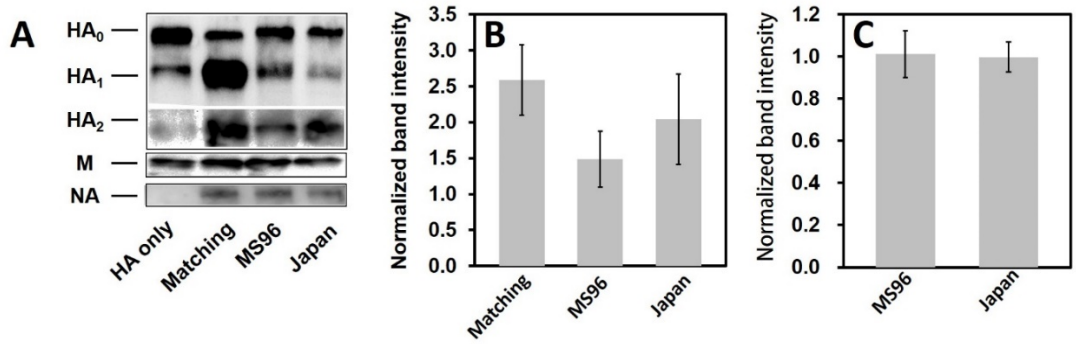

Figure 17. Quantification of intensities of HA, NA and VSV M protein by Western Blot (A). The HA_1 (B) and NA (C) band intensities were directly detected by Chemidoc XRS+ imager and normalized to corresponding M band intensity to obtain the relative HA and NA expression levels on different VSV pseudotyped particles. Each error bar represents the mean ± SD of three independent experiments. NA protein was also detected except for HA only particles.

3.3.4. HA and NA expression in transfected cells. During production of pseudoparticles, cells were transfected with the same amount of HA- and NA-encoding plasmids DNA (6 μg), but HA incorporation levels in each type of particle varied, while NA stayed relatively constant, as shown in the Western blot analysis [137]. Hence, an immunofluorescence assay was used to monitor HA and NA trafficking in BHK-21 cells. 24 h post transfection, HA, NA, and cell nuclei were

fluorescently labeled in permeablized and non-permeablized conditions **(Fig. 18)**. Staining in the permeablized condition gives an assessment of the HA and NA localization in the cell, while the non-permeabilized condition shows cell surface expression of the viral proteins.

In the permeablized condition (top three panels), HA accumulated mostly within perinuclear vesicles in HA-only ($H3_{X\text{-}31}$), mismatching ($H3_{X\text{-}31}/N2_{MS96}$) and mismatching ($H3_{X\text{-}31}/N2_{Japan}$) conditions. In matching transfected cells ($H3_{X\text{-}31}/N2_{X\text{-}31}$), HA was found to accumulate in perinuclear patches that extended throughout the cytoplasm. The NAs were found being expressed more diffusely in cells than X-31 HA. No NA signal was observed in the HA-only ($H3_{X\text{-}31}$) condition, as expected.

In the non-permeablized condition (bottom three panels), the different NAs and the X-31 HA could be observed co-localizing at the cell surface in most cells. Cells co-transfected with matching $H3_{X\text{-}31}/N2_{X\text{-}31}$ displayed the strongest cell-surface expressed HA labeling. $H3_{X\text{-}31}/N2_{Japan}$ co-transfected cells had slightly less bright cell-surface HA labeling, followed by $H3_{X\text{-}31}/N2_{MS96}$ co-transfected condition and cells without NA transfection had the lowest cell-surface HA expression.

Overall, the immunofluorescence microscopy results are in alignment with the report by Galloway et al. which also compared the expression of H3 in X-31 HA-transfected cells with and without cognate N2, and showed that NA influences trafficking of HA to the cell surface in BHK and Vero cells [138]. Taken together, these results indicate that the matching NA is required for efficient HA trafficking to the plasma membrane, which is the site of virion budding for both native influenza and VSV pseudotyped particles. Danieli *et al.* and Lee *et al.* suggest that an influenza A virus requires at least three HA trimers to be close to each other to form a hemifusion site [135, 139], which indicates that the density of HA trimers affects the

hemifusion rate of influenza A virus. The immunofluorescence analysis shown here confirms the Western blot HA densitometry data and suggests that NA plays an important role in expression and intracellular trafficking of HA, and that even within the same subtype (N2), different NAs can influence cell-surface expression of HA.

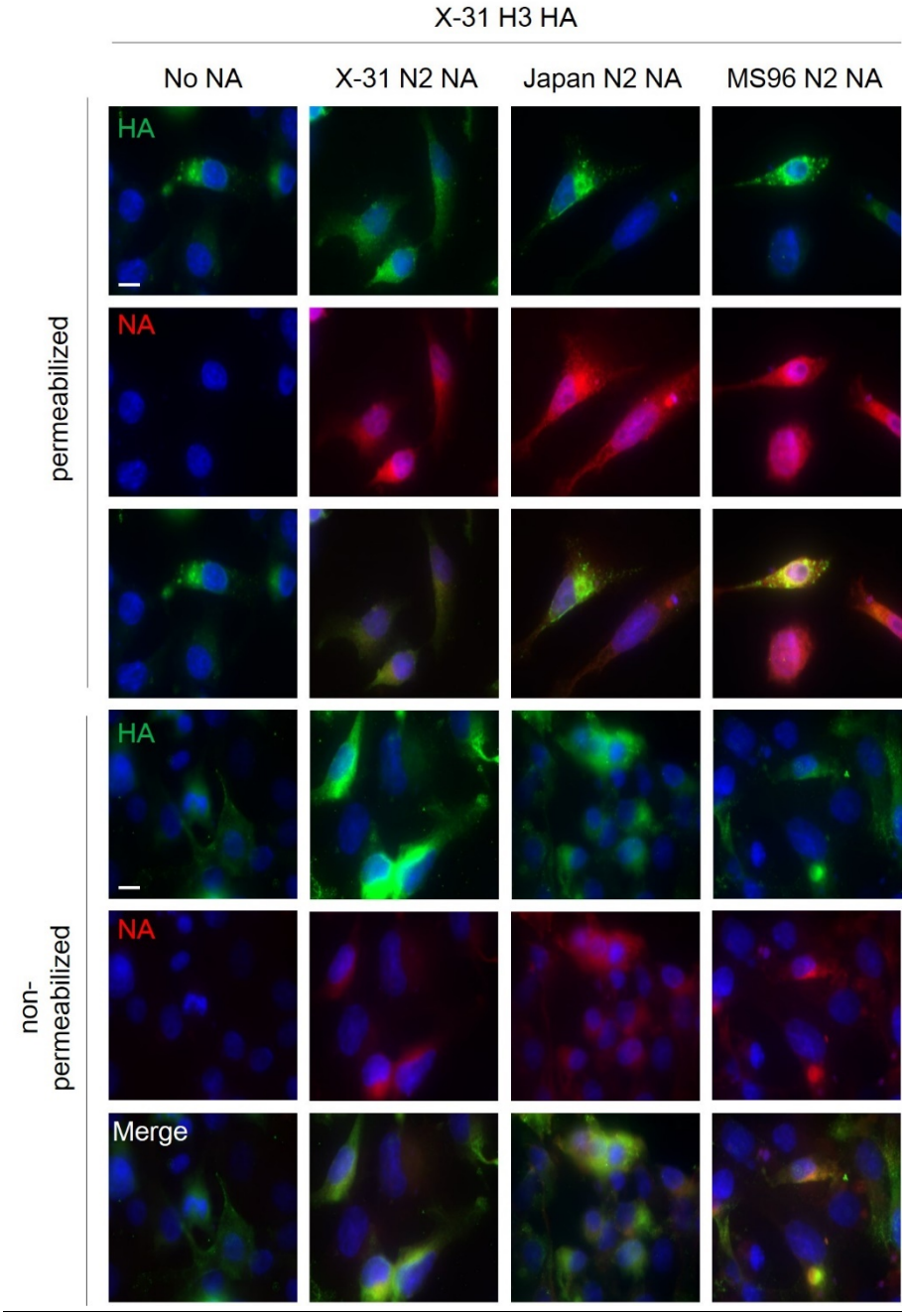

Figure 18. Expression and subcellular localization of HA and NA in HA-NA co-transfected BHK-21 cells by immunofluorescence microscopy assay. Cell nuclei were labeled with DAPI (blue), and HAs/NAs were labeled with anti-HA (clone

HA-7) and anti-N2 (H6N2) primary antibodies and with corresponding fluorophore-conjugated antibodies (false-colored with HA in green and NA in red). Top three rows: permeabilized BHK-21 cells imaged using 100× objective. Bottom three rows: non-permeabilized BHK-21 cells using 100× objective and with identical exposure time. For each panel, cells were co-transfected with pCAGGS-H3(X-31) and with either (from left to right): pCAGGS-empty (No NA), pCAGGS-N2 (X-31), pCAGGS-N2(Japan) (Japan N2 NA), and pCAGGS-N2(MS96) (MS96 N2 NA). Scale bar represents 10 μm.

3.3.5. Effect of NA inhibition on hemifusion kinetics. Influenza NA has an important role during progeny virus egress from host cell by enzymatically cleaving sialic acids and facilitating the release of viral particles [17, 140, 141]. Here, our immunofluorescence assay result suggests that heterologous N2 proteins modify H3 trafficking in HA-NA co-transfected cells, and can lead to a decrease in HA incorporation levels in VSV pseudotyped particles. Single-particle fusion analyses reveal that the rate of hemifusion decreased significantly with lower surface HA protein expression level [142].

In order to assess whether the enzymatic activity of NA plays a role in these observations, we used N-Acetyl-2,3-dehydro-2-deoxyneuraminic acid (NADNA), a known inhibitor of NA, to block the neuraminidase activity on influenza X-31 **(Fig. 19)**. The data demonstrates the hemifusion kinetics of NADNA-treated influenza virus and non-treated virus are similar at pH 4.0 and pH 5.1, and there were no significant differences on viral binding either. The hemifusion rate constant of NA inhibitor treated virus is 0.24 s^{-1} with a value of 2.5 for N at pH 4, and 0.06 and 1.9 at pH 5.1. That NADNA does not affect hemifusion kinetics of the virus follows the conclusions of Ohuchi et al.'s work[142], where they also found that NA inhibitors do

not impact either binding or fusion; however, they suggest that NA function does impact endocytosis, and in this way, impacts "entry". Since the SPT assay presented here isolates binding and fusion processes from endocytosis, our results corroborate Ohuchi et al.'s observations and reinforces our conclusion that differences in expression level (HA/NA) balance among particles is important for the fusion process.

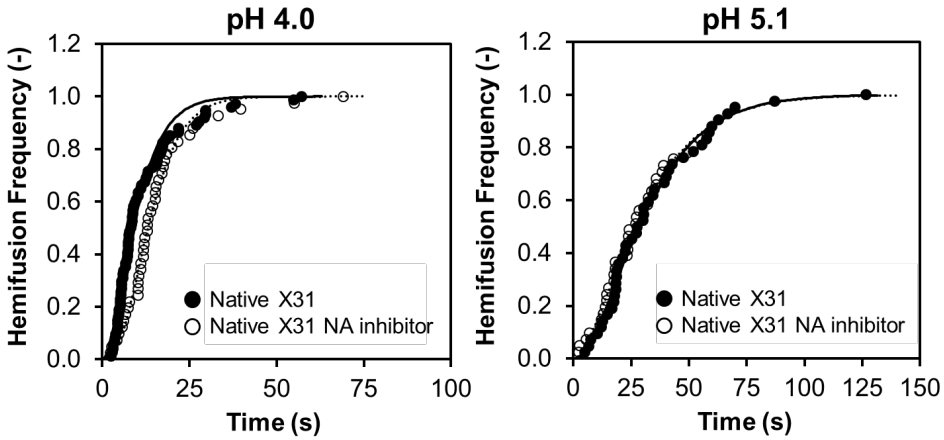

Figure 19. Cumulative distribution of hemifusion events at pH 4.0 and pH 5.1 for NADNA-treated influenza X-31 and non-treated influenza X-31.

3.4. Discussion

The ever-evolving diversity of influenza virus strains, particularly those of avian origin, represents a pressing concern for global health. While it is well known that mutations and the reassortment of gene segments generates this diversity, understanding the consequences of different combinations of viral genes, particularly those encoding HA and NA still awaits further elucidation. Some studies have shown that a functional balance of HA and NA is required for virus replication[143] and that insufficient NA enzymatic activity leads to the formation of virus aggregates on

egress [144]. Here, we have investigated how incorporation of different NAs affect the fusion function of the HA protein and provide more evidence for a potential role for NA during entry and glycoprotein transport.

Using a VSV-based viral pseudotyping approach we were able to specifically study the interplay between HA and NA. This system allowed us to study the co-incorporation of H3 HA and N2 NA of the prototypical strain X-31 and to switch N2 NAs of different strains. We produced four different types of influenza pseudoparticles: pseudoparticles containing HA only ($H3_{X-31}$), X-31 HA and NA matching pseudoparticles ($H3_{X-31}/N2_{X-31}$), and to model N2 NA gene reassortment, human:human mismatching pseudoparticles ($H3_{X-31}/N2_{Japan}$) and human:avian mismatching pseudoparticles ($H3_{X-31}/N2_{MS96}$). Particles that incorporated both X-31 HA and NA displayed distinctly higher fusion kinetics than those harboring HA only. Further, we show that the X-31 matching pseudoparticles ($H3_{X-31}/N2_{X-31}$) exhibit similar hemifusion kinetics than native influenza X-31. Other combinations of particles display different kinetics from the native particles.

The significant decrease of hemifusion rate between influenza X-31 and mismatching pseudoviruses could be explained by the variations in HA incorporation on the pseudotyped particles when different NAs were co-transfected [136, 138], a hypothesis confirmed by quantitatively analyzing HA_1 bands in Western blot assays performed on concentrated pseudotyped particles. However, the degree of NA incorporation by Western blot showed that the densities were similar for the three different NAs in the pseudoparticles. These results are also supported by the immunofluorescence microscopy assay that shows that HA trafficking varies considerably depending on which NA is co-expressed in transfected BHK-21 cells, leading to differential HA expression on cell plasma membranes, whereas NA

expression does not seem as affected. These analyses demonstrate that NA does not act directly on HA function but rather has an indirect effect by modulating the trafficking and incorporation of HA into pseudotyped viral particles. Our work shows that switching NAs of the same subtype (N2) can have profound effect on fusion kinetics mediated by the HA protein. This study suggests that HA-NA combinations form pairs of varying compatibility that can ultimately impact HA fusogenicity. In summary, we show that influenza X-31 H3 HA requires its matching neuraminidase to maximize the HA packaging density on VSV pseudoparticles, and the matching pseudoparticles exhibit similar hemifusion kinetics as influenza X-31 by single virion fusion assay.

Beyond this study, there are some directions worth pursuing next. First, defining the pore formation of VSV pseudoparticles is an important step to understanding the impact of HA-NA balance on genome transfer. From previous studies we know that the pore formation kinetics of influenza H3N2 is described by a simple single exponential decay (one step transition from hemifusion intermediate to open pore) [35, 37] which begs the question if pseudovirus particles behave in the same way, or if HA-NA balance may impact this process as well. The SPT fusion platform has been useful for screening the HA neutralizing antibodies [145]. We note a recent development of a high-throughput, microdroplet-based single particle hemifusion assay [146, 147] that is a potentially powerful tool to screen antibodies could be also useful in expanding the studies presented here to characterize many phenotypes quickly based on hemifusion function.

CHAPTER 4

Evaluating the pandemic potential of influenza A virus (H10N8) according to hemagglutinin (HA)-mediated membrane fusion attributes

Hung-Lun Hsu[1], Jean K. Millet[2], Gary R. Whittaker[2], and Susan Daniel[1*]

[1]School of Chemical and Biomolecular Engineering, Cornell University, Ithaca NY 14853, United States and [2]Department of Micrbiology and Immunology, Cornell University, Ithaca NY 14853, United States

4.0. Acknowledgement

This chapter is currently under review as "Evaluating the pandemic potential of influenza A virus (H10N8) according to hemagglutinin (HA)-mediated membrane fusion attributes". Hung-Lun Hsu was the first author and co-authors include Jean K. Millet, Gary R. Whittaker and Susan Daniel. H.L.H. and S.D. conceived and designed the study. H.L.H performed experiments and carried out data analysis. This work was supported by the National Science Foundation (Grant CBET-1263701 to S.D.) Work in the authors' labs is also funded in whole or in part with Federal funds from the National Institute of Allergy and Infectious Diseases, National Institutes of Health, Department of Health and Human Services, under the Centers of Excellence for Influenza Research and Surveillance (CEIRS) Contract No. HHSN272201400005C.

4.1. Introduction

Influenza viruses are membrane-enveloped, single-stranded, negative sense segmented RNA viruses of the family *Orthomyxoviridae*. In order to deliver their genomic viral RNA segments into host cells, influenza viruses must accomplish several key steps through specific virus-host interactions that are mediated by cell surface receptors and viral envelope proteins. Influenza A viruses harbor two distinct envelope glycoproteins: hemagglutinin (HA) and neuraminidase (NA), for cell entry

and egress, respectively. HA is a trimeric membrane-embedded glycoprotein that is a critical determinant for host tropism as it mediates both binding to host cell surface receptors and fusion of viral and host cell membranes. HA is composed of two subunits, HA1 and HA2, where HA1 governs binding to target cells, while HA2 governs membrane fusion by conformational rearrangement that exposes the fusion peptide. Importantly, HA requires proteolytic activation by host cell proteases to become fusion-competent, a priming event that occurs between the HA1 and HA2 subunits.

The first step of influenza virus entry is the binding of HA1 to host cell receptors, α-sialic acids (α-SA), an event that triggers endocytosis of the virion [17]. During maturation of the endosome, the internal pH decreases. The acidic environment triggers major conformational changes in HA, leading to exposure and release of the fusion peptide found at the N-terminal extremity of HA2 [148]. The fusion peptide then inserts into the target endosomal membrane and further conformational changes pull the viral and endosomal membranes together until they merge. During this process of membrane fusion, an intermediate structure is formed, the hemifusion stalk, where only the outer leaflets of the two opposing membranes are fused. Eventually the hemifusion intermediate collapses and forms an expanding fusion pore, where influenza genomic RNAs are released into the cytoplasm allowing viral replication to ensue [17, 34]. Moreover, viral fusion depends on the characteristics of the host cell in various ways, e.g. host protease expression profile [29, 149], the progression of endosomal acidification [138], and properties of host cell membrane [150].

Influenza A viruses are divided into subtypes based on antigenic and amino acid sequence differences of the HA and NA surface glycoproteins, each composed of 18

and 11 known subtypes, respectively. HA subtypes H1-H16 and NA subtypes N1-N9 are found in avian species, while humans are known to be infected by three main subtypes: H1N1, H2N2, and H3N2. However, other virus subtypes including H5N1, H7N2, H7N3, H7N7, H9N2, H10N7, H7N9, H6N1, H5N6, and H10N8 have been found to be able to infect humans, with avian H5N1, H7N9 and H9N2 subtypes recognized for their pandemic potential in the human population [151-153]. Transmission of AIV to humans is controlled by binding avidity preferences towards different types of α-SA [17]. Among other factors, AIV more preferentially binds to α2,3 galactose-linked SA and less so to α2,6 galactose-linked SA. On the surface of epithelial cells in the upper respiratory tract of humans, there are high levels of α2,6-SA receptors and low levels of α2,3-SA receptors. Moreover, α2,3-SA receptors are present predominantly in the lower respiratory tracts of humans[154]. In contrast, α2,3-SA receptors are more readily found in epithelia of avian species [155, 156]. Despite differences in binding avidity towards α-SA, AIV is still considered an important pathogenic threat for humans. The major concern is that AIV can accumulate mutations that would enable the virus to acquire efficient replication and transmission capabilities in humans, which may lead to an influenza pandemic.

Pandemic influenza remains a serious threat to human health globally due to the fact that it is unpredictable and can result in millions deaths [157]. Vaccinations and antiviral drugs are effective control measures for influenza, however, the frequent emergence of novel influenza viruses and the emergence of resistant strains complicate their implementation. Hence, the Influenza Risk Assessment Tool (IRAT) was developed by the Centers of Disease Control and Prevention (CDC) to evaluate the pandemic potential of newly emerging influenza viruses. IRAT builds a framework which weighs 10 risk elements and the top three weighted elements are

human infection, transmission (laboratory animals), and receptor binding [40]. However, there is evidence that besides virus receptor binding properties, virus fusion properties might also play a role in virus pandemic potential [35, 41, 138, 158-163]. Russier and colleagues showed changes in the pH of activation for HA of the pandemic influenza virus (pH1N1) during its inter-species transmission from swine to humans [41]. The HA activation pH decreased significantly when it transmitted from swine (activating pH > 5.5) to early human cases (pH 5.5), which further decreased in human isolates characterized later in the pandemic (pH 5.4-5.2). Galloway et al. reported that the HA activation pH of human seasonal viruses is closer to pH 5.0 [138]. Costello et al. further reported that at single-virion level, the HA of a clinically relevant strain, H3N2 (Brisbane), was observed to be able to maintain its fusogenicity for the longest time at low pHs (pH 5.1-4.5) compared to the egg-adapted strain (Udorn), and the laboratory-adapted strain (X-31) [35]. Furthermore, influenza has also been shown to adapt to enhance its ability to remain fusion-competent in lower pH environments (HA structural stability) [159, 163]. Because the human airway tissue constitutes an acidic environment (pH 5.5-6.9) [42, 43], both these adaptations boost the success of infecting these host cells. These findings highlight and promote the importance of taking into account changes in HA activation pH and ability to persist in acidic environments (structural stability) when evaluating the pandemic potential of newly-emerged influenza virus strains [162, 164].

In this study, we focus on the emergence of a recent influenza strain which was initially characterized in a human case in 2013 in Jiangxi Province, China (strain A/Jiangxi-Donghu/346/2013(H10N8), or H10N8 (JX346)) [165]. JX346 has been reported to be less pathogenic in poultry, but its infection in humans was found to be lethal [166]. So far, three human cases have been reported, two of which were fatal,

suggesting that future cases of human infection with H10N8 may be associated with a high fatality rate [167]. An additional concern arose from the observation that, after several passages of an avian H10N8 strain in the lungs of mice, the passaged viruses became more virulent and resulted in the death of the animals [168]. Although to date there have been few reported human H10N8 infections and deaths, it is important to characterize in detail this strain, as it could represent a future pandemic threat [169]. To assess one critical aspect of pathogenicity, we examined the fusogenicity of JX346 HA by cell-cell fusion and single-particle hemifusion assays. In single-particle hemifusion assay, murine leukemia virus (MLV)-based pseudotyping system was performed as the surrogate of influenza H10N8 (JX346). Previously, we have shown a similar influenza pseudotyping system can recapitulate the hemifusion characteristic of native virus at the single-virion level[170]. The single-particle hemifusion data on JX346 HA presented here, unveils distinct HA fusion attributes that govern viral entry and could impact transmissibility and govern pathogenicity and pandemic potential. With this work, we reinforce the importance of characterizing fusion attributes of emergent strains like H10N8 influenza virus for a more complete assessment of pandemic potential.

4.2. Materials and Methods

4.2.1. Cells plasmids and antibodies. African green monkey kidney Vero-E6, human embryonic kidney HEK-293T, and Madin-Darby canine kidney (MDCK) cells were obtained from the American Type Culture Collection (ATCC, Manassas) and grown in Dulbecco's modified Eagle medium (DMEM, CellGro), supplemented with 10% fetal bovine serum (Gibco), 1% penicillin and 10 μg/mL streptomycin (CellGro), 1% HEPES buffer (CellGro). The cells were cultured in a 37 °C, 5% CO_2 incubator. pCMV3-H10N8-JD-13-HA(JX346), pCMV3-JD-13-NA(JX346) plasmids were

purchased directly from Sino Biological (EPI497479 for N8; EPI497477 for H10). pCMV3-H10N8-JD-13-HA(JX346), pCMV3-H10N8-JD-13-NA(JX346), pCMV-MLVgag-pol, and pTG-Luc plasmids were used to transfect HEK-293T cells for pseudotyped particle production. pCMV3-H10N8-JD-13-HA(JX346) and pCMV3-H10N8-JD-13-NA (JX346) plasmids were cotransfected along with pCMV-MLVgag-pol and pTG-Luc to produce H10N8 pseudotyped particles. pCMV-MLVgag-pol encodes the retroviral core proteins of murine leukemia virus (MLV), and pTG-Luc transfer vector encodes a luciferase reporter gene with a packaging sequence. pCAGGS-VSV-G encodes the glycoprotein (G) of the vesicular stomatitis virus (VSV) and pCAGGS empty vector were used to generate positive and negative control-pseudotyped particles, respectively.

Polyclonal anti-H10 sera was produced by immunizing a rabbit (Rockland) with purified, baculovirus-derived H10 HA (Sino Biological)

4.2.2. H10 expression characterization. The H10 HA expression in Vero cells were assessed using both immunofluorescence assay and western blotting. 5×10^5 cells Vero-E6 cells were seeded in 8-well microscopy glass slides (Millipore). After 24 h cells were transfected with a mixture containing 0.75 μL of Lipofectamine 2000 transfection reagent (Thermo Fisher Scientific) and 1 μg of plasmid DNA (500 ng of H10-encoding plasmid and 500 ng N8-encoding plasmid) or 500 ng of H10-encoding plasmid for each well, and incubated for 24 h. Transfected cells were then fixed with 4% paraformaldehyde (PFA) (Thermo Fisher Scientific) for 15 min and PFA was then quenched in 50 mM ammonium chloride (NH_4Cl) for 15 min. For the permeabilized condition, 0.1% Triton X-100 was added to each well for 5 min at 4 °C and washed three times with DPBS. The cells then were blocked with 5% normal goat serum for 45 min and labeled with rabbit anti-H10 (Rockland), followed by incubation with the

secondary Alexa Fluor 488-conjugated goat anti-rabbit antibody (Thermo Fisher Scientific). Nuclei were labeled with DAPI (Southern Biotech). Microscopy images were acquired using inverted microscope (Carl Zeiss) with a 63× objective.

To further characterize the antibody-antigen interaction specificity, the Vero-E6 cells transfected with H10-encoding plasmid and N8-encoding plasmid or transfected with empty vector were lysed and analyzed by western blotting. 24 h post transfection, the cells were washed once by DPBS and lysed with RIPA buffer (Thermo Fisher) for 15 min at 4 °C. The attached cells were removed by a cell scraper. The cell lysate was then further incubated for 15 min at 4 °C, and the lysate was centrifuged at 13000 × g for 5 min at 4 °C to remove cell debris. The supernatant was collected, and denatured by incubating with SDS sample buffer (10% 2- mercaptoethanol) for 7 min at 75 °C. Samples were then analyzed by western blot using rabbit anti-H10 (Rockland) followed by incubation with HRP-conjugated goat anti-rabbit IgG (Life Technologies). Western blots were visualized and analyzed using a Chemidoc XRS+ system with Image Lab image capture software (Bio-Rad).

4.2.3. Cell-cell fusion assay [171]. HA stability and membrane fusion were assessed by cell-cell fusion assay. 5×10^5 Vero-E6 cells were seeded in 8-well microscopy glass slides (Millipore). After 24 h cells were transfected with a mixture containing 0.75 μL of Lipofectamine 2000 transfection reagent (Thermo Fisher Scientific) and 1 μg of plasmid DNA (500 ng of H10-encoding plasmid and 500 ng N8-encoding plasmid) for each well, and incubated for 24 h. Cells were then treated with 3 μg/mL of trypsin for 30 min at 37 °C to activate H10 expressed on the cell membrane. Cells were then incubated with a low-pH buffer (5 mM HEPES, 5 mM MES, 5 mM succinate, 150 mM NaCl) for 5 min at 37 °C to destabilize the HA and induce fusion. Cell-cell fusion was left to proceed for 1 h at 37 °C in DMEM. Cells were then fixed

with 4% paraformaldehyde (PFA) (Thermo Fisher Scientific) for 15 min followed by quenching with 50 mM ammonium chloride (NH_4Cl) for 15 min. The antibody labeling procedure was performed as detailed above. Microscopy images were acquired using an inverted microscope (Carl Zeiss) with a 20× objective. Syncytia were analyzed by counting number of nuclei per syncytium, with at least 9 syncytia assessed for each condition.

4.2.4. Preparation of influenza pseudoparticles. HEK-293T cells were seeded in a 6-well plate (Corning), and incubated for 24 h. The cells were then transfected with a mixture containing 3 μL of Lipofectamine 2000 transfection reagent (Thermo Fisher) and 1.3 μg of plasmid DNA (300 ng of H10-encoding plasmid, 300 ng of N8-encoding plasmid, 300 ng pCMV-MLVgag-pol and 400 ng pTG-Luc plasmids) in each well, and incubated for 48 h [172]. Supernatants containing pseudotyped particles were collected after several gentle taps on the walls of petri dishes to help release of particles. Supernatants were ultracentrifuged in a Ti45 rotor at 35,000 rpm for 120 min and pellets were resuspended in PBS and then aliquoted for storage at -80 °C. The particles were treated by 3 μg/mL trypsin and incubated for 30 min at 37 °C to activate HA right before use[173]

4.2.5. Liposomes used to prepare supported bilayers. Liposomes contained 4:4:2:0.5:0.01 molar ratio of 1,2,dioleoyl-sn-glycero-3-phosphocholine (DOPC), 1-oleoyl-2-palmitoyl-sn-glycero-3-phosphocholine (POPC), cholesterol, total ganglioside extract (TGE) and Oregon green DHPE (pH sensitive marker), based on compositions found in previous studies that provide comparative data [37, 69]. The lipids were purchased from Avanti Polar Lipids (Alabaster, AL), and Oregon green DHPE was purchased from Molecular Probes, Eugene, OR. To form liposomes, all components were dissolved and mixed in biotechnology grade chloroform

(Sigma-Aldrich) in a glass vial. The bulk solvent was first removed by blowing high purity nitrogen and the solution was placed in a desiccator under vacuum for 3 h to ensure complete evaporation of the solvent. PBS buffer was then added to the vial to re-suspend the dried lipid film to create a 5 mg/mL solution. Liposomes were then extruded ten times through a 100 nm pore size polycarbonate filter (Whatman Nucleopore), and five times through a 50 nm pore size filter.

4.2.6. Preparation of glass surfaces for supported bilayers. Glass microscope coverslips (25 mm × 25 mm; No. 1.5) from VWR were cleaned in piranha solution (45 mL 50% hydrogen peroxide and 105 mL 70% sulfuric acid) for 10 min, then rinsed 30 min with deionized water with a minimum resistance of 18.2 MΩ cm (Siemens Purelab Ultra water purification system). Glass slides were flushed by deionized water again and dried by a stream of ultra-pure nitrogen gas prior to plasma cleaning.

4.2.7. Fabrication of microfluidic devices. The generation of microchannel silicon mold developed using soft lithography was published previously [36, 48, 69]. The pattern contains six trenches 70 μm deep, 135 μm wide and 1.5 cm long with 100 μm spacing between each channel. Microfluidic devices were formed using polydimethylsiloxane (PDMS) in a molding process. The silicon mold was coated with chlorotrimethylsilane (Sigma-Aldrich) via vapor deposition to facilitate the release of cured PDMS. A 10:1 (elastomer:crosslinker) mixture of Sylgard 184 (Dow Corning) was mixed and degassed to remove bubbles before pouring on the silicon mold. The PDMS was then crosslinked in the oven for 3 h at 80 °C. Both the piranha cleaned glass cover slip and the microfluidic device were assembled by oxygen plasma bonding. They were first treated with oxygen plasma using a Harrick Plasma Cleaner (Model # PDC-32G, Ithaca, NY) at a pressure of 750 millitorr on the “high”

setting for 15 s. The two pieces were then pressed together gently to form a tight bond and annealing was performed at 80 °C for 15 min.

4.2.8. Forming supported bilayers in microfluidic channels. To produce biomimetic planar supported lipid bilayers, various methods have been developed [48, 133, 134]. Here, self-rupturing lipid vesicles were generated to form a host cell-mimetic membrane bilayer. A 10% diluted solution of liposomes prepared as described above in PBS was drawn into the microchannel at a flow rate of 100 μL/min for 90 s and incubated on the glass substrates for 2 h. The microchannel was then rinsed with the PBS buffer at 100 μL/min for 2 min. To heal defects in membranes, a 5% diluted solution of liposomes in PBS buffer was drawn into the microchannel at 10 μL/min for 5 min. Before loading virus-containing solutions, channels were rinsed again with PBS buffer at 100 μL/min for 2 min.

4.2.9. Fluorescent labeling of viruses. Hemifusion in single particle tracking is reported by fluorescence dequenching. For these experiments, influenza H10N8 (JX346) pseudotyped particles were labeled with a lipophilic reporter called octadecylrhodamine B chloride (R18), a red-emitting fluorophore, at a sufficient concentration and sonicated 30 min to quench fluorescence. The particles were then passed through a MicroSpin G-25 column (GE Healthcare Life science) to remove excess R18. The fluorophore-labeled particles were then ready to be flowed into the channels for binding and hemifusion assays.

4.2.10. Single particle hemifusion assay: microscopy. Another method used to assess HA stability and membrane hemifusion is single particle tracking of hemifusion in supported lipid membranes formed within microfluidic devices. These assays were performed using total internal reflection fluorescence microscopy (TIRFM) with an inverted Zeiss Axio Observer.Z1 with an α Plan-Apochromat 100×

oil immersion objective which has a numerical aperture (NA) of 1.46. Index-matching immersion oil (Carl Zeiss, Inc.) was added to the glass coverslip of the microfluidic device and the objective. A laser with 561 nm excitation wavelength was used to simultaneously excite red fluorophores under this setting. The Laser TIRF 3 slider (Carl Zeiss, Inc.) was used to control the angles of incidence in the optical pathway. Exceeding the critical angle (~62°) generates total internal reflection due to the difference in refractive indices of the two different substances (glass and aqueous buffer), and further creates an evanescent wave that penetrates about 100 nm into the aqueous buffer. Because virion binding and fusion occurs within a ~100 nm thick region, the evanescent wave can excite fluorophores near the membrane and eliminate background noise from virions in the bulk aqueous phase.

4.2.11. Single particle hemifusion assay: experimental execution. R18-labeled influenza pseudotyped particles were drawn into the channels and allowed to bind to the bilayers for at least 15 min. Unbound particles were rinsed out with PBS buffer at a flow rate of 100 μL/min for 90 s. To test the effect of triggering pH on influenza HA hemifusion kinetics, acidic buffers (150 mM NaCl, 1.5 mM MES, 5 mM citric acid) pre-calibrated over a range of acidic pH values were used. Each solution was delivered through a microfluidic channel at a flow rate of 100 μL/min for 120 s to acidify the microfluidics device channels and induce membrane hemifusion between particles and SLBs. The R18 dequenching spike from particle hemifusion were recorded with a CCD camera for 4 min.

4.2.12. Single particle hemifusion assay: image processing. Membrane hemifusion events were analyzed using both ImageJ (NIH) and MATLAB (Mathworks). Each hemifusion event was manually selected in ImageJ with Time series analyzer V2.0 plugin, and the intensity of each event in 4 × 4 pixels was averaged and saved with

the corresponding time as a table. The data was then processed by MATLAB to calculate membrane hemifusion parameters.

4.3. Results

4.3.1. H10 characterization and H10 sera testing. The pCMV3-H10 and pCMV3-N8 plasmids were first used to transfect mammalian cells to test the H10 HA expression and trafficking with or without N8 NA. Rabbit sera from the H10 immunized animal (Rockland) was used to detect and confirm the expression of H10 HA protein in Vero-E6 cells by immunofluorescence (IFA) analysis (**Fig. 20A**). To be sure the antibodies generated from the rabbit sera were specific to H10N8 transfected cell lysate, bands corresponding to H10 HA0 (~75 kDa) were analyzed and detected by western blot (**Fig. 20B**).

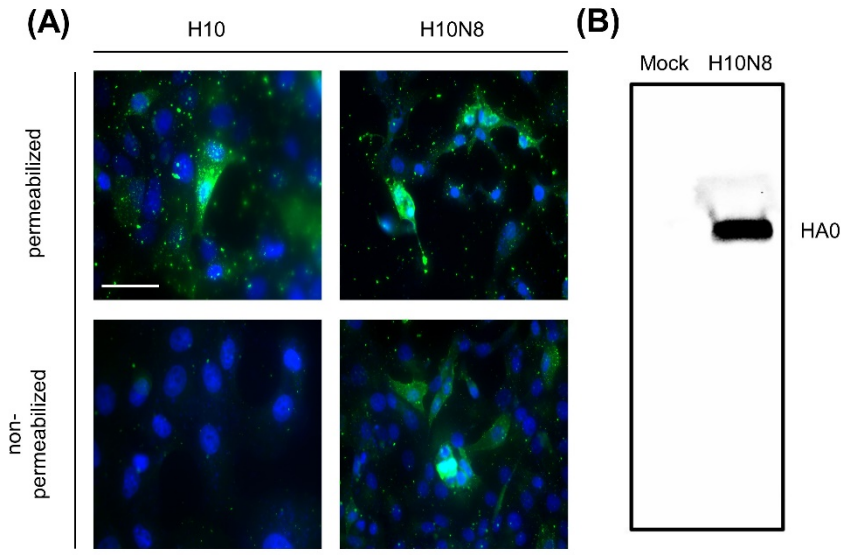

Figure 20. H10 expression and detection in Vero-E6 cells. (A) Expression and subcellular localization of HA in H10/N8 co-transfected Vero-E6 cells visualized by immunofluorescence microscopy. Cell nuclei were labeled with DAPI (blue), and HA was labeled with rabbit anti-H10 followed by AF488-conjugated goat anti-rabbit

antibody. Top row: permeabilized Vero-E6 cells imaged using 63× objective. Bottom row: non-permeabilized Vero cells using 63× objective and with identical exposure time. The scale bar represents 50 μm. (B) Western blot of H10 HA. H10/N8 transfected cells or mock-transfected cells were lysed. HA was detected by rabbit anti-H10 primary antibody and HRP-conjugated goat anti-rabbit secondary antibody.

IFA analysis was conducted to track the trafficking of the HA in the cells. 24 h post transfection, HA and cell nuclei were fluorescently labeled in membrane permeabilized and membrane non-permeabilized conditions. The permeabilized plasma membrane condition shows the location of HA in the cytosol, where the antibody can bind to HA present in cell organelles (e.g. Golgi apparatus, ER). We found that in the permeabilized condition, HA accumulates mostly within perinuclear vesicles when expressed without N8 expression. However, in HA and NA co-transfected cells, HA was found to accumulate in perinuclear patches that spread throughout cytoplasm. In the non-permeabilized condition, which shows the plasma membrane surface expression of the viral proteins, in the absence of N8 NA, the HA signal appeared to be weaker at the surface compared to the HA and NA co-transfected cells, which showed robust surface expression.

4.3.2. Cell-cell fusion assay results. With the confirmation that we can express H10 on the surface of cells, we first set out to characterize its fusogenicity using cell-cell fusion assays. The goal of these experiments was to determine the pH threshold at which H10 starts to mediate membrane fusion. We define this point as the HA fusion activation pH, which is an important property of HA that may contribute to a strain's pathogenicity and tropism.

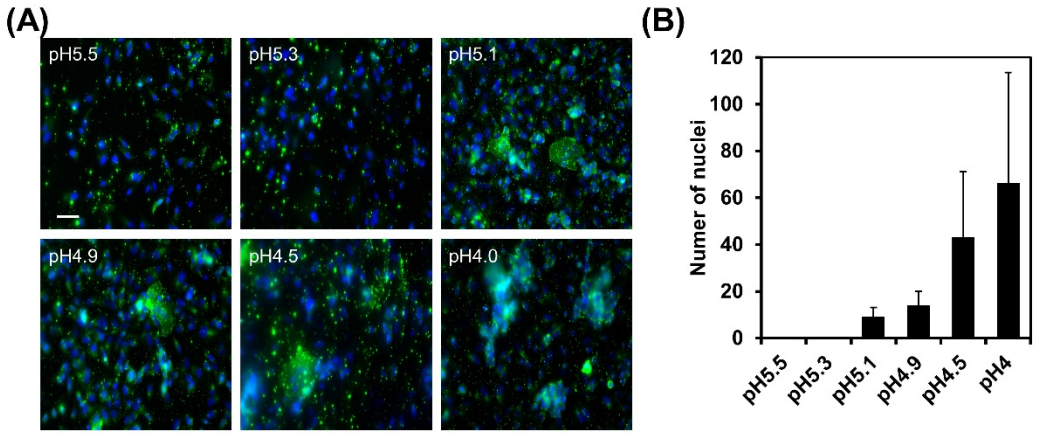

Figure 21. H10 fusogenicity characterization. (A) H10N8 cell-cell fusion assay. H10 was labeled by rabbit anti-H10 serum followed by anti-rabbit AF488-conjugated secondary antibody. Nuclei were stained with DAPI (blue). Syncytia (multinucleated cells) can be observed from pH 5.1 to pH 4. The images were obtained by using a 20× objective, and the scale bar represents 50 μm. (B) The number of nuclei per syncytium were counted and plotted for different pH values.

For these experiments, Vero-E6 cells were co-transfected to express H10 and N8 and treated with the HA-activating protease TPCK-trypsin in 8-well glass slides. The cells in each well were then incubated in a pH buffered solution ranging from pH 3.5 to 7 to trigger membrane fusion. Cells were then fixed and labeled with rabbit anti-H10 sera and with the nuclear stain DAPI so that the formation of syncytia could be determined. At the fusion activation pH, formation of syncytia containing multiple nuclei were observed. In Vero-E6 cells (**Fig. 21A**), the first syncytia were observed at pH 5.1, with no syncytia observed at pH 5.5 or 5.3. A semi-quantitative analysis was used to evaluate the extent of cell-cell fusion that shows that there is an acidic

pH-dependent increase in the extent of fusion (number of nuclei/syncytium) (**Fig. 21B**).

In order to examine the fusion properties of the H10 (JX346) in more detail, we describe results from single particle fusion assays using H10N8 pseudoparticles. Single particle hemifusion assay monitors the hemifusion between the outermost leaflet of the membranes of an individual pseudoparticle and a host cell. With the higher resolution afforded by single particle imaging, we gain additional information regarding fusion in the virus entry step, i.e., H10 acid stability (the amount of time HA can remain fusion competent in a given acidic environment) and the pH-dependent H10 hemifusion kinetics. These features are also potentially important aspects of entry behavior that can be assessed for pandemic potential.

4.3.3. H10N8 pseudotyped particle production and infectivity assay. Prior to using the pseudovirus particles for single particle fusion assays, we first assessed their overall cell infectivity using a luciferase assay. Murine leukemia virus (MLV) pseudotyped particles harboring both H10 and N8 proteins and containing the luciferase reporter gene were generated. Such pseudotyping approach has been successfully used for other envelope glycoproteins such as those of the Ebola virus and Middle East Respiratory Syndrome coronavirus (MERS-CoV) [174-177]. After the pseudoparticles were harvested, they were used to transduce MDCK cells to test the infectivity. The infectivities were measured as relative luciferase units (RLU) from the infected cells. The positive control particles harboring VSV-G had an infectivity level around at ~1 × 10^7 RLU. For negative control conditions, both non-infected cells and Δenv particles had infectivities of ~1 × 10^2 RLU, a lower limit indicating no infectivity. H10N8 pseudotyped particles have an infectivity level at ~1

$\times 10^5$ RLU. For comparison, H10 pseudotyped particles (no NA) have an infectivity level at ~1×10^2 RLU, supporting our previous western blot results that these particles have little to no HA incorporated (**Fig. 22B**). Overall, these results demonstrate that the pseudotyped particles harboring H10N8 HA and NA proteins can be successfully produced and give rise to robust infectivity in MDCK cells. Furthermore, a western blotting assay was conducted to demonstrate the H10 expression on pseudoparticles. **Figure 22B** shows HA0 was barely detected on the pseudotyped particles containing H10 only and no HA1 was detected (the left column). However, two bands corresponding to H10, HA0 (~75 kDa) and HA1 (~50 kDa), were detected in H10N8 pseudotyped particles (the right column). After trypsin treatment, the signal for HA0 decreases and the signal of HA1 increases (the middle column). Together, these results show that H10 can be expressed and detected by the rabbit sera in our system and that is it necessary to co-express N8 in the particles to ensure presence of H10 in the pseudotyped viral particles and their infectivity. These results align with previous reports that show that the model human influenza virus (H3N2) X-31 strain requires its strain-matched N2 protein co-expression for efficient HA packaging into pseudoparticles (and to recapitulate its native virus fusion attributes) [149, 170].

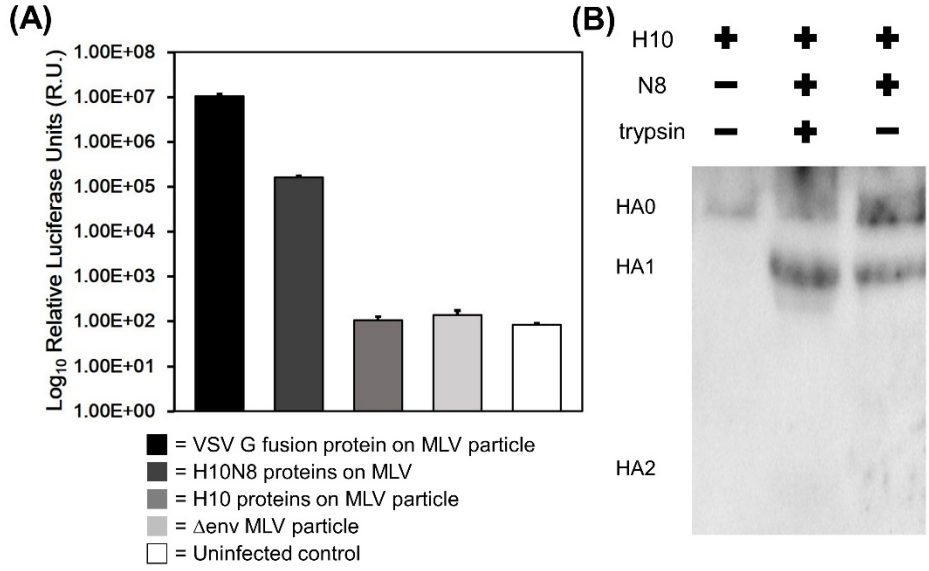

Figure 22. H10N8 pseudotyped particles characterization. (A) Assessment of MLV-based pseudotyped particle infectivity by luciferase assay. Four types of MLV pseudotyped particles were produced and used to infect MDCK cells. 72 h post-infection, infected MDCK cells were lysed and analyzed for luciferase activity using a luminometer. The values are the mean with S.D. of triplicate wells. (B) Western blot of H10 HA. H10 or H10N8 were expressed on MLV pseudotyped particles and detected by rabbit anti-H10 primary antibody and HRP goat anti-rabbit secondary antibody. H10N8 pseudotyped particles were treated by 3 μg/mL trypsin to cleave HA.

4.3.4. Single-particle hemifusion assay. We monitored individual virion membrane fusion events of H10N8 pseudotyped particles with supported lipid bilayers (SLBs) using a microfluidic platform coupled with a total internal reflection fluorescence (TIRF) microscope. By changing the angle of the incident laser, an evanescent wave at the interface between the glass and aqueous buffer can be generated. In this configuration, the evanescent wave illuminates a region 100 to 200 nm away from the

interface, where viral binding and fusion events on the SLB can be readily monitored. The SLB is designed to mimic a host cell surface; it contains phospholipids, cholesterol, total ganglioside extract (TGE) for the receptor, and Oregon green DHPE as a pH indicator. TGE is a glycolipid that is extracted and purified from porcine brain tissue, and contains mainly α2,3-linked sialic acid (SA) and serves as the receptor for the virus. Oregon green DHPE is a pH-sensitive fluorophore embedded in the SLB that serves as an indicator of acidification of the channel by drastically decreasing its intensity when exposed to an acidic solution in the range of pH 4 to 7. For quality control of our supported bilayers, the fluidity of the SLBs was examined by using fluorescence recovery after photobleaching (FRAP), and the diffusivity was determined to be 0.812 ± 0.01 $\mu m^2/s$ which meets the average diffusivity and mobile fractions reported previously [170].

To evaluate the hemifusion behavior of influenza H10N8 (JX346), the membranes of H10N8 pseudotyped particles were labeled with a red membrane-intercalating, quenched dye, octadecyl rhodamine B chloride (R18). Control of the buffer environment of the bound particles was readily managed using the microfluidic device to precisely control and change different solution conditions. Fusion was triggered by acidifying the channel and tested over a range of low-pH buffered solutions. Upon membrane hemifusion, the outer leaflets of the virus particles and the SLB mix, which results in the R18 that was originally contained in the viral particle diffusing radially away from the fusion site in the SLB and consequently dequenching. These dequenching events of hemifusion are easily detected and recorded with a CCD camera. The resulting video microscopy analysis provides information about the hemifusion lag time for each particle, which is defined as the time between the pH drop (assessed by the decrease in Oregon green signal) and onset of hemifusion (spike

of dequenching) for each individual particle. Once all the hemifusion events are cataloged by their time points, the lag time distributions are fit to the following cumulative gamma distribution:

$$p_H = \int_0^1 \frac{k_H^N t^{N-1}}{\Gamma(N)} e^{-k_H t}\, dt$$

where p_H is the probability of hemifusion, k_H is the hemifusion constant, t is lag time, and N is an additional fit parameter. N represents the number of independent steps that are required for hemifusion to occur. However, within the context of virus fusion, N is often assigned as the number of HA trimmers that must act concertedly to initiate fusion [37]. k_H and N are usually plotted as a function of pH to assess the pH-dependence of the hemifusion rate during acidification. Because in a maturing endosomal environment, the pH drops, we tested the pH range from the early endosome (~pH 6) to the late endosome (~pH 5). The hemifusion lag time can give an indication of the timing of virus genome release along the endocytic pathway and whether this happens closer to the plasma membrane or the cell nucleus [35]. This is a critical step in the influenza virus life cycle, as the genome requires transport into the nucleus for replication. Nevertheless, we have previously shown that in terms of fusion kinetics, influenza HA- and NA-pseudotyped particles behave almost identically to wild type, native viral particles [170], making this approach useful in assessing fusion properties of native viruses, so long as the HA and NA are matched.

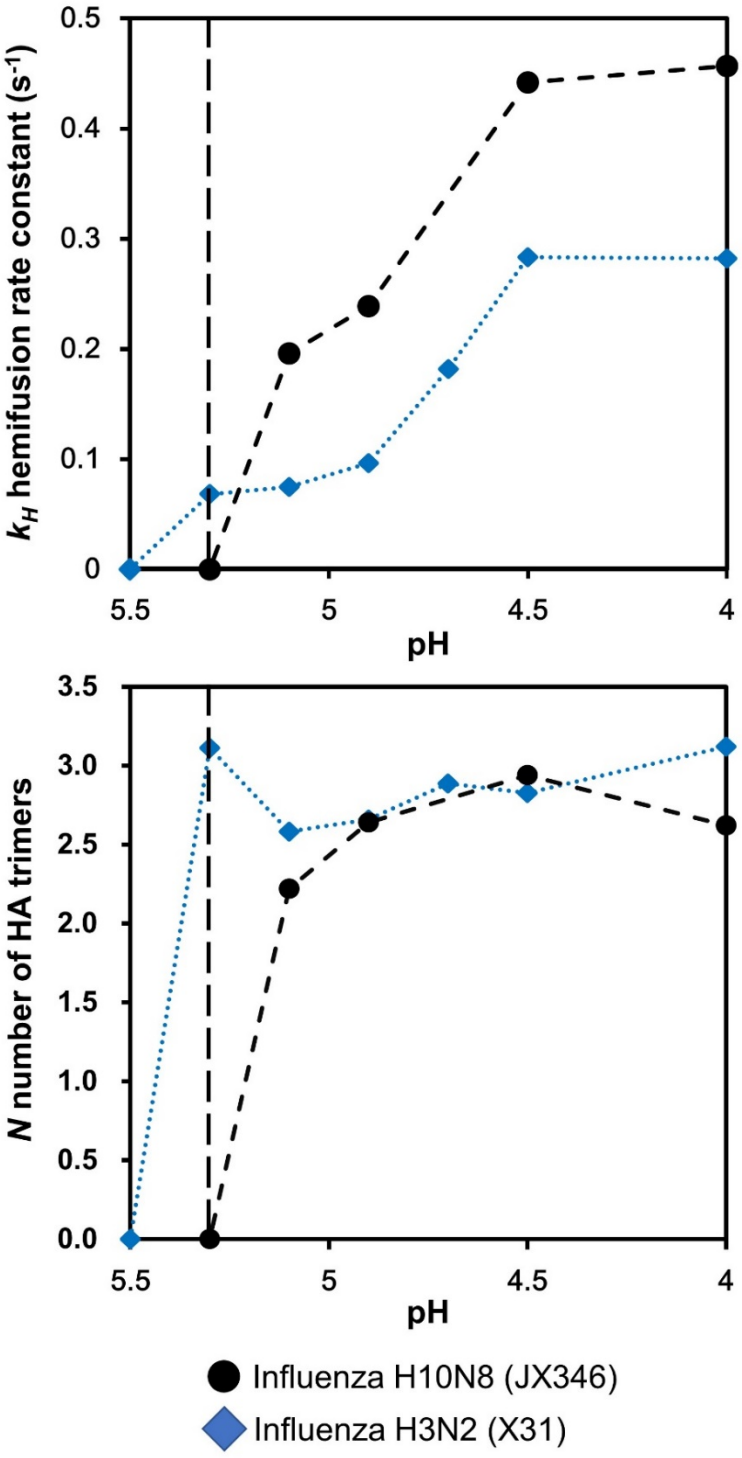

Figure 23. H10 hemifusion kinetics. Hemifusion rate constant, k_H and number of HA trimers, N, as a function of pH for native influenza X-31, and H10N8 (JX346) pseudoparticles. Dashed lines serve for visual guidance only. The vertical dashed line indicates the fusion activation pH of JX346.

We characterized the fusion behavior of H10N8 pseudotyped particles and compare to results for a common egg-adapted influenza strain, X-31 (H3N2) over a range of initiation pHs (**Fig. 23**). The first hemifusion events for H10N8 particles are observed at pH 5.1 at single-particle level, which agrees with the previous cell-cell fusion assay, where the first syncytia were observed at pH 5.1 as well. Looking at the trends in the single particle data, generally, the hemifusion rate constant of H10N8 pseudotyped particles increases with decreasing pH, and the hemifusion rate constant, $k_{H,}$ at pH 4.5 is ~2.3-fold higher than at pH 5.1. Compared to a standard egg-adapted strain, X-31, the k_H values of H10N8 are always ~2-fold higher than the k_H values from influenza X-31. The kinetic data here suggests that after endosomal uptake, due to the lower pH of HA activation pH for JX346, it may release its genome later along the endosomal pathway than X-31, so the viral genomes may have a better chance to reach the host nucleus [104, 105, 178]. Additionally, at lower pHs, the hemifusion rate of H10N8 is higher than X-31, which may also indicate that more fusion activity occurs in late endosomes for H10N8 than for X-31, which may correlate overall to more infection. Looking at the *N* parameter from the fits, it appears that both H10N8 and X-31 in general require ~3 cooperating proteins over most of the physiological pH range. This result agrees that in general, three HA trimers are needed for fusion to take place [135].

4.3.5. Extent of fusion. The extent of fusion of H10N8 pseudotyped particles can provide an additional parameter for evaluating the pathogenic potential of H10N8. Using hemifusion data from the single particle tracking assay described previously, we calculated the extent of hemifusion for H10N8. The extent of hemifusion is

defined as the ratio, expressed in percentage, between the number of fused virions and the number of bound virions at t_0 (right before pH is dropped). In **figure 24**, the extent of fusion of H10N8 is plotted at different initiation pHs. At pH 4, H10N8 has the highest extent of fusion at ~35%, and at pH 5.1 it reaches its lowest value at ~16%. The trends show that the extents of fusion decrease with increasing pH, which is similar to the trend of the number of nuclei in the syncytia (**Fig. 21B**). Comparison of the extent of fusion of H10N8 with the ones of X-31 and two other H3N2 strains (A/Brisbane/07/H3N2 (Brisbane) – clinical strain , and A/Udorn/72/H3N2 (Udorn) – another egg-adapted strain) characterized previously [170], shows that H10N8 has a fusion extent that is higher than the ones for X-31 and the Brisbane strains, but lower than the one for the Udorn strain [35].

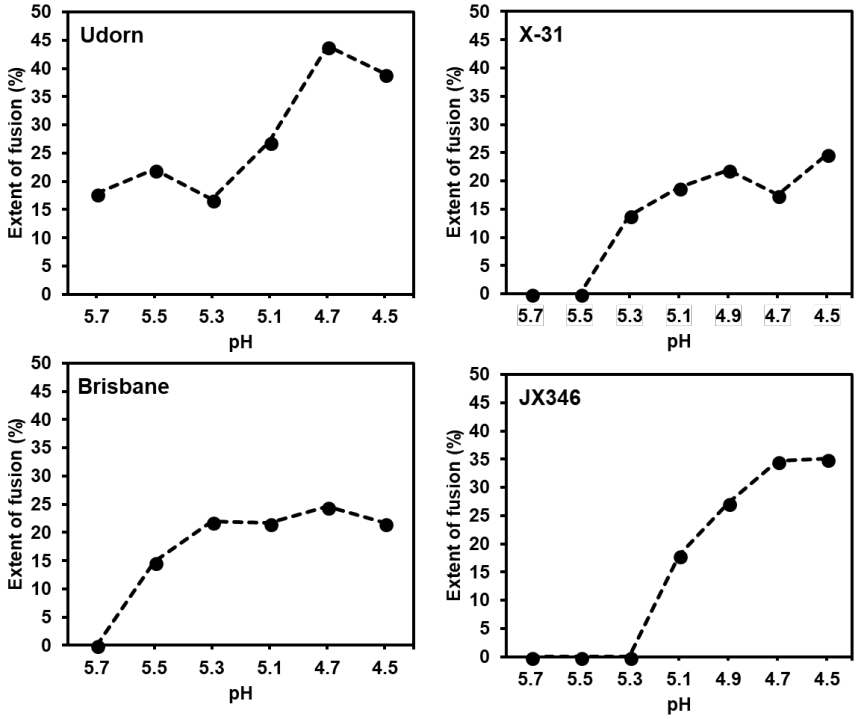

Figure 24. Extent of fusion for three H3N2 strains (Udorn, Brisbane and X-31) and H10N8 (JX346) over the range of examined pHs. The extent of fusion is defined as (number of fusion virions)/(number of bound virions at t_0) × 100%. The data of Udorn, Brisbane, and X-31 were replotted from our previous publication [35].

4.3.6. H10 acid stability. Another parameter for evaluating pathogenicity of a potentially pandemic strain is the ability of HA to remain fusion competent in an acidic environment, also referred to here as its acid-dependent structural stability. This parameter can be obtained by examining the distribution of HA-mediated hemifusion events over time as a function of pH derived from the hemifusion kinetic data (**Fig. 25A**). From this data, the time of the last hemifusion event for each pH is plotted against the pH. For H10N8, the last hemifusion events occurs between ~80-110 s over all initiating pHs tested, indicating that the acidification deactivates H10 beyond this time point. The advantage of SPT here is that because we can visually monitor each individual particle, we can obtain more precise information on how long HA can remain fusogenic in different acidic environments. Costello et al. previously demonstrated that the HA of the human clinical H3N2 strain, A/Brisbane/07/H3N2 (Brisbane), can remain stable relatively longer, in an acid-independent manner (~140 s) than common laboratory-adapted strains [35]. Here we note that the extent of fusion of H10N8 is higher than the H3N2 strain (Brisbane). However, when comparing Brisbane and JX346 to laboratory-adapted H3N2 strains, both are more acid-stable, but JX346 does not sustain as long in an acidic environment as the Brisbane strain before becoming inactivated.

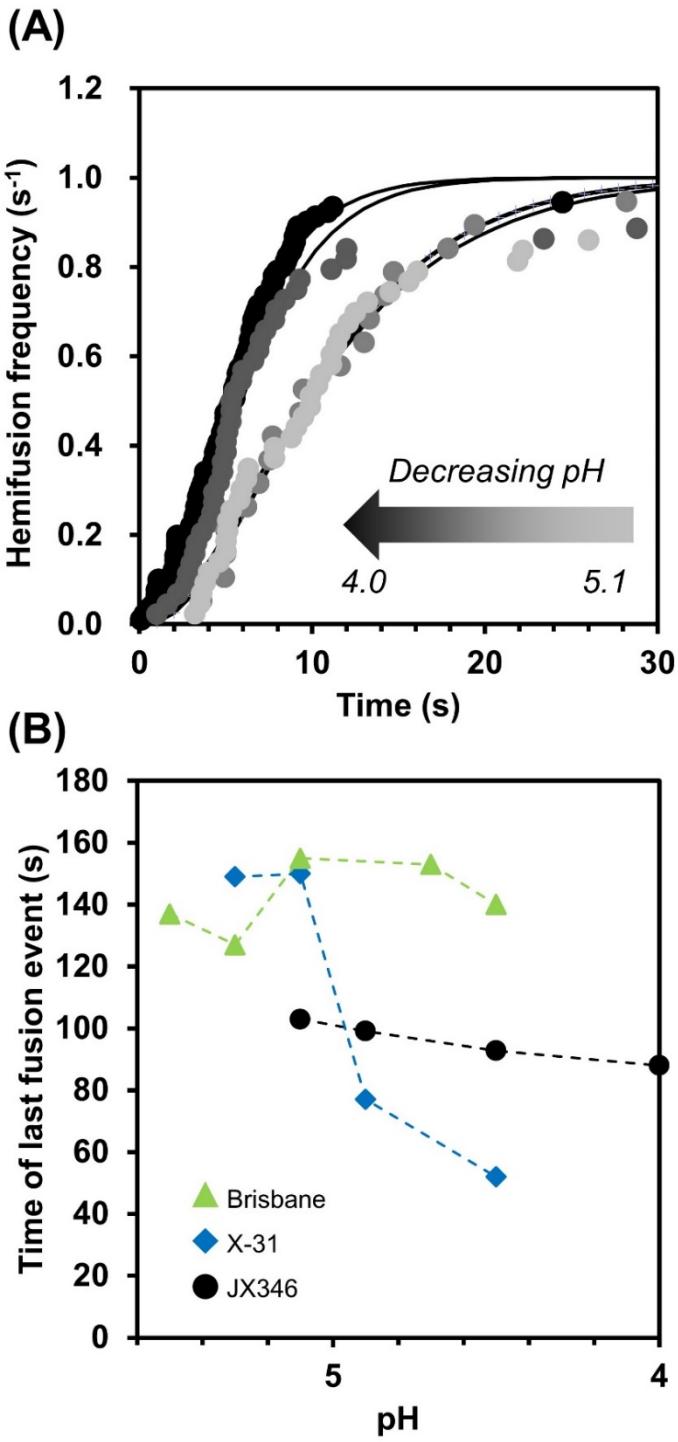

Figure 25. Acid stability of H10. (A) Cumulative distribution of hemifusion events at pH 4, 4.5, 4.9 and 5.1 (from left to right) from t = 0 s to t = 30 s. (B) Time point at which the curves to the top reach 1.0 indicating when fusion activity ceases at each pH value. The values for X-31 and Brisbane are replotted from Costello *et al.* data

[35].

3.4. Discussion

The objective of this work is to use individual virion fusion assays to characterize an emergent influenza strain's fusion properties and gain more insight into its pandemic potential. Western blot analyses indicated that the rabbit anti-H10 antibody can bind to an epitope on HA1 on pseudotyped particles made from the JX346 coat protein sequences. H10 incorporation into particles was decreased in absence of N8 co-expression, which suggests that H10 HA requires its matching NA for efficient incorporation into particles. Furthermore, cell-cell fusion assays indicate that H10 fusion is pH-dependent and syncytia were first observed at pH 5.1. JX346 strain H10N8 pseudotyped particles were further examined for their fusion attributes at the single-particle level, which was necessary due to the unavailability of native virus particles.

The HA fusion activation pH of influenza virus (JX346) was determined both by cell-cell fusion assays and SPT analyses. While cell-cell fusion assay allows determination of the pH threshold for initiating HA fusion, it does not provide other information regarding HA fusion attributes. SPT can provide a more comprehensive characterization. With SPT, we can determine the initiating pH threshold for HA-mediated fusion (HA fusion activation), the rate at which fusion occurs as a function of initiating pH (pH–dependent kinetics), the duration of HA activity in a given acidic environment (HA acid stability), and the extent of overall fusion at a given initiating pH. It is important to note that the highest fusion initiation pH does not always correlate with maximal fusion rate.

The acid stability of HA is a factor that can be important in determining the successful

outcome of an infection because it impacts the timing of release of viral RNA within an infected cell [35]. Also, the acid stability promotes the survival of virus in a more acidic human airway before getting into the endosome, so the HA does not get deactivated before cellular uptake. Considering all the data from SPT and cell-cell fusion assays, it appears that H10N8 may have evolved towards better acid stability to overcome the naturally more acidic environments in potential new hosts, like the natural barrier of the human airway [42, 179]. Furthermore, H10 HA shows an increased rate of fusion as the initiating pH is decreased. Together these data indicate that the properties H10 of JX346 are conducive to shifting the tropism of this virus to human hosts. However, considering the findings that JX346 H10 binds more preferentially to α2,3 galactose-linked SA than α2,3 galactose-linked SA [180], and H10 can be cleaved by trypsin and weakly by matriptase[149], suggests JX346 is more an avian influenza virus than a human influenza virus. In conclusion, we suggest that HA fusion properties, including pH of HA fusion activation, HA acid stability, and rates of fusion, might be several crucial factors important for assessing virus transmission ability. Hence, these attributes should be considered as part of the influenza risk assessment tool (IRAT).

CHAPTER 5

CONCLUSIONS & OUTLOOK

This thesis has presented several achievements for understanding influenza virus-host interaction at the single-particle level. The single particle tracking (SPT) technique used in this thesis offers new insights into the mechanism that influenza viruses use to enter cells and cause local and systemic infection. This work provides insight into the impact of influenza reassortment on virus entry and extends the application of SPT technique to further investigate an influenza antiviral drug.

The importance of this thesis is that we developed new tools to study highly pathogenic viruses while minimizing safety concerns. Pseudoviruses have been utilized widely in the field to replace the native pathogenic viruses. However, there was no reported data to demonstrate that pseudoviruses mimic the native virus entry at the single-particle level. Hence, by applying the pseudovirus system, we first showed that pseudovirus particles mimicking a lab-adapted strain, influenza X-31, recapitulate the native, live virus fusion behavior. Next, we wanted to investigate the influenza reassortment process and we generated reassorted particles. We conducted SPT experiment on these influenza reassorted pseudoviruses and found that the reassortment impacted the virus hemifusion kinetics. We ultimately determined that the mismatching NAs slowed down the fusion kinetics by hampering the HA trafficking inside the HA/NA expressing cells. This work demonstrated that although influenza reassortment causes serious pandemic in human societies, the mutation is not always infectious because it might prevent the HA from becoming packaged on the virus membrane.

After confirming that the pseudoviruses can serve as the best mimic for native pathogenic viruses, we further applied SPT techniques to an emerging influenza virus

(JX346). JX346 was initially characterized in a human case in 2013 in Jiangxi Province, China (strain A/Jiangxi-Donghu/346/2013(H10N8), or H10N8 (JX346)) [69]. So far, three human cases have been reported, two of which were fatal, suggesting that future cases of human infection with H10N8 may be associated with a high fatality rate [71]. In this study, we showed that the highest pH for HA fusion activation for JX346 is relatively low at pH 5.1, corroborating previous reports that lower activation pH is an adaptation detected in strains that jump to human hosts. Moreover, we showed that the rate of membrane hemifusion of JX346 is pH dependent, similar to what we observed for X-31, a lab-adapted H3N2 strain. However, in contrast to X-31, but similar to H3N2 human clinical strains, JX346 strains remains fusion-competent longer in a low pH environment. Given these features, JX346 has entry properties that could promote transition to human hosts and underscores that fusion attributes should be included in the influenza risk assessment tool (IRAT). In the future, SPT can be a helpful tool for surveilling the emerging influenza viruses and evaluating their potential of causing pandemic in humans.

Lastly, from ongoing work in collaboration with Prof. Hang at the Rockefeller University, we applied the SPT technique to investigate the impact of an interesting membrane protein, interferon-induced transmembrane proteins IFITM 3 on viral entry (**appendix A**). IFITMs have been shown to inhibit virus entry, but the actual cellular and biochemical mechanism of how they modulate the antiviral activities is still unclear. Hence, using SPT to study the IFITM3 inhibitory mechanism may benefit the field because it can easily distinguish whether IFITM3 affects viral binding, hemifusion or pore formation. Furthermore, SPT provides a purer system that only focuses on the impact of IFITM3 on virus entry.

CHAPTER 6

REFERENCE

1. Marsh, M. and A. Helenius, *Virus entry into animal cells*, in *Advances in virus research*. 1989, Elsevier. p. 107-151.
2. Nguyen, D.H. and J.E. Hildreth, *Evidence for budding of human immunodeficiency virus type 1 selectively from glycolipid-enriched membrane lipid rafts.* Journal of virology, 2000. **74**(7): p. 3264-3272.
3. Marsh, M. and A. Helenius, *Virus entry: open sesame.* Cell, 2006. **124**(4): p. 729-740.
4. White, J.M. and G.R. Whittaker, *Fusion of enveloped viruses in endosomes.* Traffic, 2016. **17**(6): p. 593-614.
5. Kawaoka, Y., *Influenza virology: current topics*. 2006: Horizon Scientific Press.
6. Kuhn, J.H., et al., *Proposal for a revised taxonomy of the family Filoviridae: classification, names of taxa and viruses, and virus abbreviations.* Archives of virology, 2010. **155**(12): p. 2083-2103.
7. Thiel, V., *Coronaviruses: molecular and cellular biology*. 2007: Horizon Scientific Press.
8. Matlin, K.S., et al., *Pathway of vesicular stomatitis virus entry leading to infection.* Journal of molecular biology, 1982. **156**(3): p. 609-631.
9. Nanbo, A., et al., *Ebolavirus is internalized into host cells via macropinocytosis in a viral glycoprotein-dependent manner.* PLoS pathogens, 2010. **6**(9): p. e1001121.
10. Saeed, M.F., et al., *Cellular entry of ebola virus involves uptake by a macropinocytosis-like mechanism and subsequent trafficking through early and late endosomes.* PLoS pathogens, 2010. **6**(9): p. e1001110.
11. Mulherkar, N., et al., *The Ebola virus glycoprotein mediates entry via a non-classical dynamin-dependent macropinocytic pathway.* Virology, 2011. **419**(2): p. 72-83.
12. Krzyzaniak, M.A., et al., *Host cell entry of respiratory syncytial virus involves macropinocytosis followed by proteolytic activation of the F protein.* PLoS pathogens, 2013. **9**(4): p. e1003309.
13. De Vries, E., et al., *Dissection of the influenza A virus endocytic routes reveals macropinocytosis as an alternative entry pathway.* PLoS pathogens, 2011. **7**(3): p. e1001329.
14. Sieczkarski, S.B. and G.R. Whittaker, *Influenza virus can enter and infect cells in the absence of clathrin-mediated endocytosis.* Journal of virology, 2002. **76**(20): p. 10455-10464.

15. Chen, C. and X. Zhuang, *Epsin 1 is a cargo-specific adaptor for the clathrin-mediated endocytosis of the influenza virus.* Proceedings of the National Academy of Sciences, 2008. **105**(33): p. 11790-11795.
16. Parrish, C.R., P.R. Murcia, and E.C. Holmes, *Influenza virus reservoirs and intermediate hosts: dogs, horses, and new possibilities for influenza virus exposure of humans.* Journal of virology, 2015. **89**(6): p. 2990-2994.
17. Skehel, J.J. and D.C. Wiley, *Receptor binding and membrane fusion in virus entry: the influenza hemagglutinin.* Annual review of biochemistry, 2000. **69**(1): p. 531-569.
18. Carr, C.M. and P.S. Kim, *A spring-loaded mechanism for the conformational change of influenza hemagglutinin.* Cell, 1993. **73**(4): p. 823-832.
19. Gamblin, S., et al., *The structure and receptor binding properties of the 1918 influenza hemagglutinin.* Science, 2004. **303**(5665): p. 1838-1842.
20. Steinhauer, D.A., *Role of hemagglutinin cleavage for the pathogenicity of influenza virus.* Virology, 1999. **258**(1): p. 1-20.
21. Bosch, F., et al., *The structure of the hemagglutinin, a determinant for the pathogenicity of influenza viruses.* Virology, 1979. **95**(1): p. 197-207.
22. Varghese, J.N., et al., *The structure of the complex between influenza virus neuraminidase and sialic acid, the viral receptor.* Proteins: Structure, Function, and Bioinformatics, 1992. **14**(3): p. 327-332.
23. Colman, P.M., *Influenza virus neuraminidase: structure, antibodies, and inhibitors.* Protein science: a publication of the Protein Society, 1994. **3**(10): p. 1687.
24. Russell, R.J., et al., *The structure of H5N1 avian influenza neuraminidase suggests new opportunities for drug design.* Nature, 2006. **443**(7107): p. 45-49.
25. Yang, P., et al., *Hemagglutinin specificity and neuraminidase coding capacity of neuraminidase-deficient influenza viruses.* Virology, 1997. **229**(1): p. 155-165.
26. Matrosovich, M.N., et al., *Neuraminidase is important for the initiation of influenza virus infection in human airway epithelium.* Journal of virology, 2004. **78**(22): p. 12665-12667.
27. Webster, R.G., et al., *Evolution and ecology of influenza A viruses.* Microbiological reviews, 1992. **56**(1): p. 152-179.
28. Simonsen, L., et al., *The impact of influenza on mortality in the USA.* Options for the control of influenza III. Amsterdam: Elsevier Science BV, 1996: p. 26-33.
29. Tse, L.V., et al., *A novel activation mechanism of avian influenza virus H9N2*

by furin. Journal of virology, 2014. **88**(3): p. 1673-1683.

30. Hensley, S.E., et al., *Hemagglutinin receptor binding avidity drives influenza A virus antigenic drift.* Science, 2009. **326**(5953): p. 734-736.
31. Mitnaul, L.J., et al., *Balanced hemagglutinin and neuraminidase activities are critical for efficient replication of influenza A virus.* Journal of virology, 2000. **74**(13): p. 6015-6020.
32. Han, X., et al., *Membrane structure and fusion-triggering conformational change of the fusion domain from influenza hemagglutinin.* Nature Structural and Molecular Biology, 2001. **8**(8): p. 715.
33. Shaw, M. and P. Palese, *Orthomyxoviridae: The viruses and their replication.*, in *Fields Virology*, D. Knipe and P. Howley, Editors. 2013, Lippincott Williams & Wilkins,: Philadelphia, PA. p. 1151-1185.
34. Bosch, F., et al., *Proteolytic cleavage of influenza virus hemagglutinins: primary structure of the connecting peptide between HA1 and HA2 determines proteolytic cleavability and pathogenicity of Avian influenza viruses.* Virology, 1981. **113**(2): p. 725-735.
35. Costello, D.A., G.R. Whittaker, and S. Daniel, *Variations in pH Sensitivity, Acid Stability, and Fusogenicity of Three Influenza Virus H3 Subtypes.* Journal of virology, 2015. **89**(1): p. 350-360.
36. Costello, D.A., et al., *Membrane fusion-competent virus-like proteoliposomes and proteinaceous supported bilayers made directly from cell plasma membranes.* Langmuir, 2013. **29**(21): p. 6409-6419.
37. Floyd, D.L., et al., *Single-particle kinetics of influenza virus membrane fusion.* Proceedings of the National Academy of Sciences, 2008. **105**(40): p. 15382-15387.
38. Wessels, L., et al., *Rapid Membrane Fusion of Individual Virus Particles with Supported Lipid Bilayers.* Biophysical Journal, 2007. **93**(2): p. 526-538.
39. *Weekly U.S. Influenza Surveillance Report*. 2018; Available from: https://www.cdc.gov/flu/weekly/index.htm.
40. Trock, S.C., S.A. Burke, and N.J. Cox, *Development of framework for assessing influenza virus pandemic risk.* Emerging infectious diseases, 2015. **21**(8): p. 1372.
41. Russier, M., et al., *Molecular requirements for a pandemic influenza virus: An acid-stable hemagglutinin protein.* Proceedings of the National Academy of Sciences, 2016. **113**(6): p. 1636-1641.
42. Washington, N., et al., *Determination of baseline human nasal pH and the effect of intranasally administered buffers.* International journal of pharmaceutics, 2000. **198**(2): p. 139-146.

43. Fischer, H. and J.H. Widdicombe, *Mechanisms of acid and base secretion by the airway epithelium.* The Journal of membrane biology, 2006. **211**(3): p. 139-150.
44. Hoekstra, D., et al., *Fluorescence method for measuring the kinetics of fusion between biological membranes.* Biochemistry, 1984. **23**(24): p. 5675-5681.
45. Lowy, R., et al., *Observation of single influenza virus-cell fusion and measurement by fluorescence video microscopy.* Proceedings of the National Academy of Sciences, 1990. **87**(5): p. 1850-1854.
46. Loyter, A., V. Citovsky, and R. Blumenthal, *The use of fluorescence dequenching measurements to follow viral membrane fusion events.* Methods of Biochemical Analysis, Volume 33, 1988: p. 129-164.
47. Melikyan, G.B., et al., *Imaging individual retroviral fusion events: from hemifusion to pore formation and growth.* Proceedings of the National Academy of Sciences of the United States of America, 2005. **102**(24): p. 8728-8733.
48. Costello, D.A., et al., *Single particle assay of coronavirus membrane fusion with proteinaceous receptor-embedded supported bilayers.* Biomaterials, 2013. **34**(32): p. 7895-7904.
49. Wang, H., et al., *SARS coronavirus entry into host cells through a novel clathrin-and caveolae-independent endocytic pathway.* Cell research, 2008. **18**(2): p. 290-301.
50. Huang, I.-C., et al., *Influenza A virus neuraminidase limits viral superinfection.* Journal of virology, 2008. **82**(10): p. 4834-4843.
51. Tang, X.-C., et al., *Identification of human neutralizing antibodies against MERS-CoV and their role in virus adaptive evolution.* Proceedings of the National Academy of Sciences, 2014. **111**(19): p. E2018-E2026.
52. Lawson, N.D., et al., *Recombinant vesicular stomatitis viruses from DNA.* Proceedings of the National Academy of Sciences, 1995. **92**(10): p. 4477-4481.
53. Whelan, S., et al., *Efficient recovery of infectious vesicular stomatitis virus entirely from cDNA clones.* Proceedings of the National Academy of Sciences, 1995. **92**(18): p. 8388-8392.
54. Schnell, M.J., et al., *Foreign glycoproteins expressed from recombinant vesicular stomatitis viruses are incorporated efficiently into virus particles.* Proceedings of the National Academy of Sciences, 1996. **93**(21): p. 11359-11365.
55. Zimmer, G., et al., *Pseudotyping of vesicular stomatitis virus with the envelope glycoproteins of highly pathogenic avian influenza viruses.* Journal

of General Virology, 2014: p. vir. 0.065201-0.

56. Longping, V.T., et al., *A novel activation mechanism of avian influenza virus H9N2 by furin.* Journal of virology, 2014. **88**(3): p. 1673-1683.
57. Lee, D.W., et al., *Image restoration and analysis of influenza virions binding to membrane receptors reveal adhesion-strengthening kinetics.* PloS one, 2016. **11**(10): p. e0163437.
58. Bally, M., et al., *Interaction of single viruslike particles with vesicles containing glycosphingolipids.* Physical Review Letters, 2011. **107**(18): p. 188103.
59. Bally, M., et al., *Interaction of virions with membrane glycolipids.* PHYSICAL BIOLOGY, 2012. **9**(2): p. 026011.
60. Bally, M., et al., *A virus biosensor with single virus-particle sensitivity based on fluorescent vesicle labels and equilibrium fluctuation analysis.* Biointerphases, 2013. **8**(1): p. 4.
61. Kukura, P., et al., *High-speed nanoscopic tracking of the position and orientation of a single virus.* Nat Meth, 2009. **6**(12): p. 923-927.
62. Szklarczyk, O.M., et al., *Receptor concentration and diffusivity control multivalent binding of Sv40 to membrane bilayers.* PLOS COMPUTATIONAL BIOLOGY, 2013. **9**(11): p. e1003310.
63. Hayden, O., et al., *Mass-sensitive detection of cells, viruses and enzymes with artificial receptors.* Sensors and Actuators B: Chemical, 2003. **91**(1): p. 316-319.
64. Hidari, K., et al., *Binding kinetics of influenza viruses to sialic acid-containing carbohydrates.* Glycoconjugate Journal, 2007. **24**(9): p. 583-590.
65. Castellana, E.T. and P.S. Cremer, *Solid supported lipid bilayers: From biophysical studies to sensor design.* Surface Science Reports, 2006. **61**(10): p. 429-444.
66. Wagner, M.L. and L.K. Tamm, *Tethered Polymer-Supported Planar Lipid Bilayers for Reconstitution of Integral Membrane Proteins: Silane-Polyethyleneglycol-Lipid as a Cushion and Covalent Linker.* Biophysical Journal, 2000. **79**(3): p. 1400-1414.
67. Richards, M.J., et al., *Membrane protein mobility and orientation preserved in supported bilayers created directly from cell plasma membrane blebs.* Langmuir, 2016.
68. Ivanovic, T., et al., *Influenza-virus membrane fusion by cooperative fold-back of stochastically induced hemagglutinin intermediates.* eLife, 2013. **2**: p. e00333.
69. Costello, D.A., et al., *Influenza virus-membrane fusion triggered by proton uncaging for single particle studies of fusion kinetics.* Analytical Chemistry,

2012. **84**(20): p. 8480-8489.

70. Lee, D., et al., *Stochastic fusion simulations and experiments suggest passive and active roles of hemagglutinin during membrane fusion.* BIOPHYSICAL JOURNAL, 2014. **106**(4): p. 843-854.
71. Suzuki, Y., et al., *Ganglioside GM1b as an influenza virus receptor.* Vaccine, 1985. **3**(3): p. 201-203.
72. Ritter, J.G., et al., *Light Sheet Microscopy for Single Molecule Tracking in Living Tissue.* PLoS ONE, 2010. **5**(7): p. e11639.
73. Alcor, D., G. Gouzer, and A. Triller, *Single-particle tracking methods for the study of membrane receptors dynamics.* European Journal of Neuroscience, 2009. **30**(6): p. 987-997.
74. Saint-Michel, E., et al., *Neurexin/Neuroligin Interaction Kinetics Characterized by Counting Single Cell-Surface Attached Quantum Dots.* BIOPHYSICAL JOURNAL, 2009. **97**(2): p. 480-489.
75. Enoki, S., et al., *Label-Free Single-Particle Imaging of the Influenza Virus by Objective-Type Total Internal Reflection Dark-Field Microscopy.* PLoS ONE, 2012. **7**(11): p. e49208.
76. Endesfelder, U. and M. Heilemann, *Art and artifacts in single-molecule localization microscopy: Beyond attractive images.* NATURE METHODS, 2014. **11**(3): p. 235-238.
77. Rowland, D.J. and J.S. Biteen, *Top-Hat and Asymmetric Gaussian-Based Fitting Functions for Quantifying Directional Single-Molecule Motion.* CHEMPHYSCHEM, 2014. **15**(4): p. 712-720.
78. Cheezum, M.K., W.F. Walker, and W.H. Guilford, *Quantitative Comparison of Algorithms for Tracking Single Fluorescent Particles.* BIOPHYSICAL JOURNAL, 2001. **81**(4): p. 2378-2388.
79. Small, A. and S. Stahlheber, *Fluorophore localization algorithms for super-resolution microscopy.* NATURE METHODS, 2014. **11**(3): p. 267-279.
80. Mortensen, K.I., et al., *Optimized localization analysis for single-molecule tracking and super-resolution microscopy.* Nature Methods, 2010. **7**(5): p. 377-381.
81. Sbalzarini, I.F. and P. Koumoutsakos, *Feature point tracking and trajectory analysis for video imaging in cell biology.* Journal of Structural Biology, 2005. **151**(2): p. 182-195.
82. Rolfe, D., et al., *Automated multidimensional single molecule fluorescence microscopy feature detection and tracking.* European Biophysics Journal, 2011. **40**(10): p. 1167-1186.
83. Smith, Matthew B., et al., *Interactive, Computer-Assisted Tracking of Speckle*

Trajectories in Fluorescence Microscopy: Application to Actin Polymerization and Membrane Fusion. Biophysical Journal, 2011. **101**(7): p. 1794-1804.

84. Jaqaman, K. and G. Danuser, *Computational Image Analysis of Cellular Dynamics: A Case Study Based on Particle Tracking.* Cold Spring Harbor Protocols, 2009. **2009**(12): p. pdb.top65.
85. Jaqaman, K., et al., *Robust single-particle tracking in live-cell time-lapse sequences.* NATURE METHODS, 2008. **5**(8): p. 695-702.
86. Bonneau, S., M. Dahan, and L.D. Cohen, *Single quantum dot tracking based on perceptual Grouping using minimal paths in a spatiotemporal volume.* IEEE Transactions on Image Processing, 2005. **14**(9): p. 1384-1395.
87. Dupont, A., et al., *Tracking image correlation: Combining single-particle tracking and image correlation.* Biophysical Journal, 2013. **104**(11): p. 2373-2382.
88. Woll, D., et al., *A novel method for automatic single molecule tracking of blinking molecules at low intensities.* Physical Chemistry Chemical Physics, 2013. **15**(17): p. 6196-6205.
89. Sage, D., et al., *Automatic tracking of individual fluorescence particles: application to the study of chromosome dynamics.* IEEE Transactions on Image Processing, 2005. **14**(9): p. 1372-1383.
90. Balasubramanian, S., et al. *An efficient non-linear cascade filtering algorithm for removal of high density salt and pepper noise in image and video sequence*. in *International Conference on Control, Automation, Communication and Energy Conservation, INCACEC 2009.* 2009.
91. Xu, Y., et al., *Wavelet transform domain filters: a spatially selective noise filtration technique.* IEEE Transactions on Image Processing, 1994. **3**(6): p. 747-758.
92. Esakkirajan, S., et al., *Removal of High Density Salt and Pepper Noise Through Modified Decision Based Unsymmetric Trimmed Median Filter.* IEEE Signal Processing Letters, 2011. **18**(5): p. 287-290.
93. Rudin, L.I., S. Osher, and E. Fatemi, *Nonlinear total variation based noise removal algorithms.* Physica D: Nonlinear Phenomena, 1992. **60**(1–4): p. 259-268.
94. Otterstrom, J. and A.M. van Oijen, *Visualization of membrane fusion, one particle at a time.* BIOCHEMISTRY, 2013. **52**(10): p. 1654-1668.
95. Ruigrok, R.W.H., et al., *Characterization of three highly purified influenza virus strains by electron microscopy.* Journal of General Virology, 1984. **65**(4): p. 799-802.
96. Rogers, G.N., et al., *Differential sensitivity of human, avian, and equine*

influenza a viruses to a glycoprotein inhibitor of infection: Selection of receptor specific variants. Virology, 1983. **131**(2): p. 394-408.

97. Suzuki, Y., et al., *Structural determination of gangliosides that bind to influenza A, B, and C viruses by an improved binding assay: Strain-specific receptor epitopes in sialo-sugar chains.* Virology, 1992. **189**(1): p. 121-131.
98. Suzuki, Y., et al., *Human influenza A virus hemagglutinin distinguishes sialyloligosaccharides in membrane-associated gangliosides as its receptor which mediates the adsorption and fusion processes of virus infection. Specificity for oligosaccharides and sialic acids and the sequence to which sialic acid is attached.* Journal of Biological Chemistry, 1986. **261**(36): p. 17057-17061.
99. Haywood, A.M., *Virus receptors: binding, adhesion strengthening, and changes in viral structure.* Journal of Virology, 1994. **68**(1): p. 1-5.
100. Barton, E.S., et al., *Utilization of sialic acid as a coreceptor enhances reovirus attachment by multistep adhesion strengthening.* Journal of Biological Chemistry, 2001. **276**(3): p. 2200-2211.
101. Stettner, E., et al., *Structure of serotype 1 reovirus attachment protein σ1 in complex with junctional adhesion molecule A reveals a conserved serotype-independent binding epitope.* Journal of Virology, 2015. **89**(11): p. 6136-6140.
102. Lee, D.W., et al., *Single-Particle Tracking Shows that a Point Mutation in the Carnivore Parvovirus Capsid Switches Binding between Host-Specific Transferrin Receptors.* Journal of Virology, 2016. **90**(9): p. doi:10.1128/JVI.03204-15.
103. Greiff, D., et al., *The Effects on Biological Materials of Freezing and Drying by Vacuum Sublimation: II. Effect on Influenza Virus.* The Journal of Experimental Medicine, 1954. **100**(1): p. 89-101.
104. Lakadamyali, M., et al., *Visualizing infection of individual influenza viruses.* Proceedings of the National Academy of Sciences, 2003. **100**(16): p. 9280-9285.
105. Brandenburg, B. and X. Zhuang, *Virus trafficking–learning from single-virus tracking.* Nature Reviews Microbiology, 2007. **5**(3): p. 197-208.
106. Jerri, A.J., *The Shannon sampling theorem and its various extensions and applications: A tutorial review.* Proceedings of the IEEE, 1977. **65**(11): p. 1565-1596.
107. Rust, M.J., et al., *Assembly of endocytic machinery around individual influenza viruses during viral entry.* Nature Structural +ACY- Molecular Biology, 2004. **11**(6): p. 567-573.

108. Cureton, D.K., et al., *Limited transferrin receptor clustering allows rapid diffusion of canine parvovirus into clathrin endocytic structures.* Journal of Virology, 2012. **86**(9): p. 5330-5340.
109. Kirchhausen, T., *Clathrin.* Annual Review of Biochemistry, 2000. **69**(1): p. 699-727.
110. Karatekin, E. and J.E. Rothman, *Fusion of single proteoliposomes with planar, cushioned bilayers in microfluidic flow cells.* NATURE PROTOCOLS, 2012. **7**(5): p. 903-920.
111. Cremer, P.S. and S.G. Boxer, *Formation and Spreading of Lipid Bilayers on Planar Glass Supports.* Journal of Physical Chemistry B, 1999. **103**(13): p. 2554-2559.
112. Richter, R.P. and A.R. Brisson, *Following the Formation of Supported Lipid Bilayers on Mica: A Study Combining AFM, QCM-D, and Ellipsometry.* Biophysical Journal, 2005. **88**(5): p. 3422-3433.
113. Seu, K.J., et al., *Effect of Surface Treatment on Diffusion and Domain Formation in Supported Lipid Bilayers.* Biophysical Journal, 2007. **92**(7): p. 2445-2450.
114. Greenwood, R. and K. Kendall, *Selection of Suitable Dispersants for Aqueous Suspensions of Zirconia and Titania Powders using Acoustophoresis.* Journal of the European Ceramic Society, 1999. **19**(4): p. 479-488.
115. Huertas, A. and G. Medioni, *Detection of intensity changes with subpixel accuracy using Laplacian-Gaussian masks.* IEEE Transactions on Pattern Analysis and Machine Intelligence, 1986(5): p. 651-664.
116. Böckmann, R.A., et al., *Effect of sodium chloride on a lipid bilayer.* BIOPHYSICAL JOURNAL, 2003. **85**(3): p. 1647-1655.
117. Sauter, N.K., et al., *Binding of influenza virus hemagglutinin to analogs of its cell-surface receptor, sialic acid: analysis by proton nuclear magnetic resonance spectroscopy and x-ray crystallography.* Biochemistry, 1992. **31**(40): p. 9609-9621.
118. Takemoto, D.K., J.J. Skehel, and D.C. Wiley, *A Surface Plasmon Resonance Assay for the Binding of Influenza Virus Hemagglutinin to Its Sialic Acid Receptor.* Virology, 1996. **217**(2): p. 452-458.
119. Takahashi, T., et al., *Binding kinetics of sulfatide with influenza A virus hemagglutinin.* Glycoconjugate Journal, 2013. **30**(7): p. 709-716.
120. Hu, J., R. Lipowsky, and T.R. Weikl, *Binding constants of membrane-anchored receptors and ligands depend strongly on the nanoscale roughness of membranes.* Proceedings of the National Academy of Sciences, 2013. **110**(38): p. 15283-15288.

121. Witt, H., et al., *Size, Kinetics, and Free Energy of Clusters Formed by Ultraweak Carbohydrate-Carbohydrate Bonds.* BIOPHYSICAL JOURNAL, 2016. **110**(7): p. 1582-1592.
122. Kanaseki, T., et al., *Structural features of membrane fusion between influenza virus and liposome as revealed by quick-freezing electron microscopy.* The Journal of Cell Biology, 1997. **137**(5): p. 1041-1056.
123. Sieben, C., et al., *Influenza virus binds its host cell using multiple dynamic interactions.* Proceedings of the National Academy of Sciences, 2012.
124. Nieba, L., A. Krebber, and A. Plückthun, *Competition BIAcore for Measuring True Affinities: Large Differences from Values Determined from Binding Kinetics.* Analytical Biochemistry, 1996. **234**(2): p. 155-165.
125. Hsu, H., et al., *Viral Fusion Efficacy of Influenza Virus H3N2 Reassortment Combination to the Suppoered Lipid Layer.* Biophysical Journal, 2017. **112**(3): p. 78a-79a.
126. Sandman, P.M. and J. Lanard, *Bird flu: communicating the risk.* Perspectives in health, 2005. **10**(2): p. 1-6.
127. Taubenberger, J.K. and D.M. Morens, *1918 Influenza: the mother of all pandemics.* Rev Biomed, 2006. **17**: p. 69-79.
128. Dawood, F.S., et al., *Estimated global mortality associated with the first 12 months of 2009 pandemic influenza A H1N1 virus circulation: a modelling study.* The Lancet infectious diseases, 2012. **12**(9): p. 687-695.
129. Sorrell, E.M., et al., *Minimal molecular constraints for respiratory droplet transmission of an avian–human H9N2 influenza A virus.* Proceedings of the National Academy of Sciences, 2009. **106**(18): p. 7565-7570.
130. Kimble, J.B., et al., *Compatibility of H9N2 avian influenza surface genes and 2009 pandemic H1N1 internal genes for transmission in the ferret model.* Proceedings of the National Academy of Sciences, 2011. **108**(29): p. 12084-12088.
131. Huang, A.S., et al., *Pseudotype formation between enveloped RNA and DNA viruses.* 1974.
132. Witte, O.N. and D. Baltimore, *Mechanism of formation of pseudotypes between vesicular stomatitis virus and murine leukemia virus.* Cell, 1977. **11**(3): p. 505-511.
133. Mashaghi, S. and A.M. van Oijen, *A versatile approach to the generation of fluid supported lipid bilayers and its applications.* Biotechnology and bioengineering, 2014. **111**(10): p. 2076-2081.
134. Diaz, A.J., et al., *Double cushions preserve transmembrane protein mobility in supported bilayer systems.* Langmuir, 2008. **24**(13): p. 6820-6826.

135. Lee, D.W., et al., *Stochastic Fusion Simulations and Experiments Suggest Passive and Active Roles of Hemagglutinin during Membrane Fusion.* Biophysical journal, 2014. **106**(4): p. 843-854.
136. Bosch, V., et al., *Inhibition of release of lentivirus particles with incorporated human influenza virus haemagglutinin by binding to sialic acid-containing cellular receptors.* Journal of General Virology, 2001. **82**(10): p. 2485-2494.
137. Su, B., et al., *Enhancement of the influenza A hemagglutinin (HA)-mediated cell-cell fusion and virus entry by the viral neuraminidase (NA).* PLoS One, 2009. **4**(12): p. e8495.
138. Galloway, S.E., et al., *Influenza HA subtypes demonstrate divergent phenotypes for cleavage activation and pH of fusion: implications for host range and adaptation.* PLoS Pathog, 2013. **9**(2): p. e1003151.
139. Danieli, T., et al., *Membrane fusion mediated by the influenza virus hemagglutinin requires the concerted action of at least three hemagglutinin trimers.* The Journal of cell biology, 1996. **133**(3): p. 559-569.
140. Air, G.M. and W.G. Laver, *The neuraminidase of influenza virus.* Proteins: Structure, Function, and Bioinformatics, 1989. **6**(4): p. 341-356.
141. Palese, P., et al., *Characterization of temperature sensitive influenza virus mutants defective in neuraminidase.* Virology, 1974. **61**(2): p. 397-410.
142. Ohuchi, M., et al., *Roles of neuraminidase in the initial stage of influenza virus infection.* Microbes and infection, 2006. **8**(5): p. 1287-1293.
143. Wagner, R., M. Matrosovich, and H.D. Klenk, *Functional balance between haemagglutinin and neuraminidase in influenza virus infections.* Reviews in medical virology, 2002. **12**(3): p. 159-166.
144. Rudneva, I., et al., *Influenza A virus reassortants with surface glycoprotein genes of the avian parent viruses: effects of HA and NA gene combinations on virus aggregation.* Archives of virology, 1993. **133**(3-4): p. 437-450.
145. Otterstrom, J.J., et al., *Relating influenza virus membrane fusion kinetics to stoichiometry of neutralizing antibodies at the single-particle level.* Proceedings of the National Academy of Sciences, 2014. **111**(48): p. E5143-E5148.
146. Mashaghi, S. and A.M. van Oijen, *External control of reactions in microdroplets.* Scientific reports, 2015. **5**.
147. Mashaghi, S. and A.M. van Oijen, *Droplet microfluidics for kinetic studies of viral fusion.* Biomicrofluidics, 2016. **10**(2): p. 024102.
148. Chernomordik, L.V., et al., *The pathway of membrane fusion catalyzed by influenza hemagglutinin: restriction of lipids, hemifusion, and lipidic fusion pore formation.* The Journal of cell biology, 1998. **140**(6): p. 1369-1382.

149. Straus, M.R. and G.R. Whittaker, *A peptide-based approach to evaluate the adaptability of influenza A virus to humans based on its hemagglutinin proteolytic cleavage site.* PloS one, 2017. **12**(3): p. e0174827.
150. Domanska, M.K., D. Wrona, and P.M. Kasson, *Multiphasic effects of cholesterol on influenza fusion kinetics reflect multiple mechanistic roles.* Biophysical journal, 2013. **105**(6): p. 1383-1387.
151. Wang, T.T., M.K. Parides, and P. Palese, *Seroevidence for H5N1 influenza infections in humans: meta-analysis.* Science, 2012. **335**(6075): p. 1463-1463.
152. Shinya, K., et al., *Avian flu: influenza virus receptors in the human airway.* Nature, 2006. **440**(7083): p. 435.
153. Garten, R.J., et al., *Antigenic and genetic characteristics of swine-origin 2009 A (H1N1) influenza viruses circulating in humans.* science, 2009. **325**(5937): p. 197-201.
154. Nicholls, J.M., et al., *Sialic acid receptor detection in the human respiratory tract: evidence for widespread distribution of potential binding sites for human and avian influenza viruses.* Respiratory research, 2007. **8**(1): p. 73.
155. Pritchett, T. and J. Paulson, *Basis for the potent inhibition of influenza virus infection by equine and guinea pig alpha 2-macroglobulin.* Journal of Biological Chemistry, 1989. **264**(17): p. 9850-9858.
156. Matrosovich, M., et al., *Avian influenza A viruses differ from human viruses by recognition of sialyloligosaccharides and gangliosides and by a higher conservation of the HA receptor-binding site.* Virology, 1997. **233**(1): p. 224-234.
157. Johnson, N.P. and J. Mueller, *Updating the accounts: global mortality of the 1918-1920" Spanish" influenza pandemic.* Bulletin of the History of Medicine, 2002. **76**(1): p. 105-115.
158. Baumann, J., et al., *H1N1 swine influenza viruses differ from avian precursors by a higher pH optimum of membrane fusion.* Journal of virology, 2016. **90**(3): p. 1569-1577.
159. Cotter, C.R., H. Jin, and Z. Chen, *A single amino acid in the stalk region of the H1N1pdm influenza virus HA protein affects viral fusion, stability and infectivity.* PLoS pathogens, 2014. **10**(1): p. e1003831.
160. Reed, M.L., et al., *The pH of activation of the hemagglutinin protein regulates H5N1 influenza virus pathogenicity and transmissibility in ducks.* Journal of virology, 2010. **84**(3): p. 1527-1535.
161. Zaraket, H., O.A. Bridges, and C.J. Russell, *The pH of activation of the hemagglutinin protein regulates H5N1 influenza virus replication and pathogenesis in mice.* Journal of virology, 2013. **87**(9): p. 4826-4834.

162. Russell, C.J., *Acid-induced membrane fusion by the hemagglutinin protein and its role in influenza virus biology*, in *Influenza Pathogenesis and Control-Volume I*. 2014, Springer. p. 93-116.
163. DuBois, R.M., et al., *Acid stability of the hemagglutinin protein regulates H5N1 influenza virus pathogenicity.* PLoS Pathog, 2011. **7**(12): p. e1002398.
164. Mair, C.M., et al., *Receptor binding and pH stability—how influenza A virus hemagglutinin affects host-specific virus infection.* Biochimica et Biophysica Acta (BBA)-Biomembranes, 2014. **1838**(4): p. 1153-1168.
165. *Summary of Influenza Risk Assessment Tool (IRAT) Results*. 2017; Available from: https://www.cdc.gov/flu/pandemic-resources/monitoring/irat-virus-summaries.htm.
166. Su, S., et al., *Epidemiology, evolution, and recent outbreaks of avian influenza virus in China.* Journal of virology, 2015. **89**(17): p. 8671-8676.
167. García-Sastre, A. and M. Schmolke, *Avian influenza A H10N8--a virus on the verge?* The Lancet, 2014. **383**(9918): p. 676-677.
168. Zhang, H., et al., *Characterization of an H10N8 influenza virus isolated from Dongting lake wetland.* Virology journal, 2011. **8**(1): p. 1.
169. Chen, H., et al., *Clinical and epidemiological characteristics of a fatal case of avian influenza A H10N8 virus infection: a descriptive study.* The Lancet, 2014. **383**(9918): p. 714-721.
170. Hsu, H.-L., et al., *Viral fusion efficacy of specific H3N2 influenza virus reassortant combinations at single-particle level.* Scientific reports, 2016. **6**.
171. Albrecht, T., et al., *Effects on cells.* 1996.
172. Millet, J.K. and G.R. Whittaker, *Host cell entry of Middle East respiratory syndrome coronavirus after two-step, furin-mediated activation of the spike protein.* Proceedings of the National Academy of Sciences, 2014. **111**(42): p. 15214-15219.
173. Klenk, H.-D., et al., *Activation of influenza A viruses by trypsin treatment.* Virology, 1975. **68**(2): p. 426-439.
174. Burns, J.C., et al., *Vesicular stomatitis virus G glycoprotein pseudotyped retroviral vectors: concentration to very high titer and efficient gene transfer into mammalian and nonmammalian cells.* Proceedings of the National Academy of Sciences, 1993. **90**(17): p. 8033-8037.
175. Wool-Lewis, R.J. and P. Bates, *Characterization of Ebola virus entry by using pseudotyped viruses: identification of receptor-deficient cell lines.* Journal of virology, 1998. **72**(4): p. 3155-3160.
176. Millet, J.K., et al., *A camel-derived MERS-CoV with a variant spike protein*

cleavage site and distinct fusion activation properties. Emerging Microbes & Infections, 2016. **5**(12): p. e126.

177. Millet, J.K. and G.R. Whittaker, *Murine Leukemia Virus (MLV)-based Coronavirus Spike-pseudotyped Particle Production and Infection.* Bio-protocol, 2016. **6**(23).
178. Mercer, J., M. Schelhaas, and A. Helenius, *Virus entry by endocytosis.* Annual review of biochemistry, 2010. **79**: p. 803-833.
179. Fischer, H., J.H. Widdicombe, and B. Illek, *Acid secretion and proton conductance in human airway epithelium.* American Journal of Physiology-Cell Physiology, 2002. **282**(4): p. C736-C743.
180. Ramos, I., et al., *Hemagglutinin receptor binding of a human isolate of influenza A (H10N8) virus.* Emerging infectious diseases, 2015. **21**(7): p. 1197.
181. Avital Percher, H., Hang, *characterization and reconstitution of s-palmitoylated ifitm3 antiviral activity.* Phd Dissertaion, 2018.
182. MacMicking, J.D., *Interferon-inducible effector mechanisms in cell-autonomous immunity.* Nature Reviews Immunology, 2012. **12**(5): p. 367.
183. Puschnik, A.S., et al., *A CRISPR toolbox to study virus–host interactions.* Nature Reviews Microbiology, 2017. **15**(6): p. 351.
184. Bailey, C.C., et al., *IFITM-family proteins: the cell's first line of antiviral defense.* Annual review of virology, 2014. **1**: p. 261-283.
185. Brass, A.L., et al., *The IFITM proteins mediate cellular resistance to influenza A H1N1 virus, West Nile virus, and dengue virus.* Cell, 2009. **139**(7): p. 1243-1254.
186. Feeley, E.M., et al., *IFITM3 inhibits influenza A virus infection by preventing cytosolic entry.* PLoS Pathog, 2011. **7**(10): p. e1002337.
187. Amini-Bavil-Olyaee, S., et al., *The antiviral effector IFITM3 disrupts intracellular cholesterol homeostasis to block viral entry.* Cell Host Microbe, 2013. **13**(4): p. 452-64.
188. Zhao, K. and N.D. Ridgway, *Oxysterol-Binding Protein-Related Protein 1L Regulates Cholesterol Egress from the Endo-Lysosomal System.* Cell Rep, 2017. **19**(9): p. 1807-1818.
189. Desai, T.M., et al., *IFITM3 restricts influenza A virus entry by blocking the formation of fusion pores following virus-endosome hemifusion.* PLoS Pathog, 2014. **10**(4): p. e1004048.
190. Andersen, K.R., N.C. Leksa, and T.U. Schwartz, *Optimized E. coli expression strain LOBSTR eliminates common contaminants from His-tag purification.* Proteins, 2013. **81**(11): p. 1857-61.
191. Weber, T., et al., *SNAREpins: minimal machinery for membrane fusion.* Cell,

1998. **92**(6): p. 759-72.
192. Tsurudome, M., et al., *Lipid interactions of the hemagglutinin HA2 NH2-terminal segment during influenza virus-induced membrane fusion.* Journal of Biological Chemistry, 1992. **267**(28): p. 20225-20232.

APPENDIX A

SINGLE PARTICLE TRACKING ASSAY OF ANTIVIRAL MEDICINE EFFECT ON INFLUENZA VIRUS MEMBRANE FUSION

0. Acknowledgement

This appendix is an ongoing work in collaboration with Prof. Hang at the Rockefeller University. In the thesis, I include part of the materials from Dr. Percher's dissertation to facilitate reader's understanding [181]. Emma Garst from the Rockefeller University, who mainly collaborates with us, provided all proteoliposome samples for making supported lipid bilayers in the SPT assay.

1. Introduction

Genetic and proteomic screens have found various candidate immune receptors, regulators and effectors [182, 183], however, the cellular and biochemical mechanisms of these host factors are most unclear. Among these factors. interferon-induced transmembrane proteins (IFITMs,) 1, 2, and 3 have been shown to

inhibit pathogen infection in vertebrates [184]. Particularly, IFITM3 attracts our attention because it was shown to mediate cellular resistance to influenza A virus (IAV) infection in mammalian cells[185]. As the IFITM family is the first ISG known to interfere with viral fusion and content entry, considerable interest has emerged in understanding their characterization and mechanism.

IFITM3 restriction of viral infection occurs at the stage of viral fusion and content delivery[186]. Although it's well know that AIV utilizes sialic acid as the receptor for binding and fusion, the mechanism of IFITM3's antiviral activity is still unknown. An unbiased conjecture of possible mechanisms include (1) an indirect mechanism whereby IFITM3 recruits a yet unknown protein/cofactor responsible for the alternation of the fusion environment, either by changing membrane properties, or by altering the maturation pathway of the endosomal vesicle, (2) a direct mechanism in which IFITM3 alters the endosomal membrane's biophysical properties such as membrane fluidity or curvature capacity, (3) the maturation of the endosomal vesicle, directing the viral particle to an incompatible environment, or (4) IFITM3 directly interacts with the viral particle, interfering with the completion of fusion to unveil the antiviral mechanism of IFITM3.

Currently, there are two models for IFITM3's antiviral behavior. It can interfere with hemifusion or interfere with pore formation. In 2013, Amini-Bavil-Olyaee *et al*. proposed that IFITM3 interferes with viral entry by disrupting cholesterol export from the late endosome[187]. They found that IFITM3 inhibits vesicle associated membrane protein-A (VAP-A), which plays a role in the cholesterol export pathway mediated by NPC-2/1 and ORP family proteins[188]. As IFITM3 inhibits VAP-A protein, they hypothesized that it will cause an increase of cholesterol in late endosomes and this increase makes the endosomal membranes stiffer. A stiff

membrane will impede viral hemifusion until the virus particle is degraded in the lysosome. However, Desai et al.[189] proposed that instead of interfering the hemifusion step, IFITM3 interferes with the pore formation step. They performed virus-cell fusion assay to image a single virus in live cells. On the other hand, our collaborator, Professor Hang's group at Rockefeller University, used bulk fusion assay to study the impact of IFITM3 on H1N1 (PR8) entry. They found that by reconstituting IFITM3 proteins into GD1a liposome, IFITM3 seems to be able to decrease the hemifusion between viruses and proteoliposomes.

To further clarify the inhibitory mechanism of IFITM3 in influenza infection, I employed single particle tracking (SPT) techniques, which is a useful tool that can easily decouple viral binding, hemifusion, and pore formation, and quantify the data at a single-particle level. In this appendix, we compare the binding and hemifusion kinetics of influenza A H1N1 (PR8) to various proteoliposomes, including a negative protein control, VAMP, IFITM3, and the loss-of-function IFITM3 mutants. We also compare the SPT results with Professor Hang's unpublished bulk fusion data. The results will be able to shed some light on the IFITM3 inhibitory mechanism against influenza A virus.

2. Materials and Methods

2.1. Induction and Enrichment of IFITM3 [181]

The Sumo-IFITM3 construct was transformed into the BL-21 LOBSTR cell line[190] containing the RIL plasmid (BL21-CodonPlus-RIL strain, Agilent) for increased copies of tRNA *argU* (AGA, AGG), *ileY* (AUA), leuW (CUA). Single colonies were grown overnight in LB media containing kanomycin (50 μg / mL) and chloramphenicol (25 μg / mL). The following day, overnight cultures were diluted 1:30 in 1 L LB with kanomycin, and incubated at 37 °C to an O.D. of 0.6 the culture

was then transferred to 18 °C, induced with 0.5 μM IPTG, and incubated overnight for 16 – 20 h. The following day, aliquots of 500 mL of cultures were spun down at 4,000 g for 15 min, and the bacterial pellet were snap frozen in liquid nitrogen for future use. On the day of purification, a 500 mL bacterial pellet was thawed on ice, and resuspended in 40 mL **Buffer A** (25 mM HEPES, 100 mM KCl, pH 7) with 2% w/v Triton-X 100, and 1x protease inhibitor mixture (Roche). If the purified protein contained any cysteines, 1 mM β-mercaptoethanol (Sigma) was added. The resuspended pellet was incubated at room temperature (RT) with 10 mg lysozyme, then sonicated (Sonic Dismembrator Model 500, Fisher Scientific) for one minute (30% power, 1 second on, 1 second off). The sample was inverted several times to ensure mixture of lysate. Sonication was repeated twice more to ensure complete lysis. After sonication, the sample was diluted 2.5 fold in Buffer A without Triton-X 100 (final volume 100 mL, 0.8% Triton-X 100), and spun down at 40,000 g for 45 min (Beckman Coulter Optima XL-100K Ultracentrifuge).

During centrifugation, 12 mL of resuspended cobalt beads ('Talon metal affinity resin' Clontech) were washed once with water, and twice with Buffer A. Post spin, the supernatant was collected and the cobalt beads added for two hours with nutation at 4 °C. The beads were then collected in an XK16/20 Column (Akta), and eluted using an AKTAFPLC chromatography system. It is during this stage that the detergent was switched from TritonX-100 to 1% octyl glucoside (Anatrace). Using a two pump protocol, the beads were treated stepwise with varying ratios of two different buffers: **Buffer B** (25 mM HEPES, 100 mM KCl, 1% octyl glucoside, pH 7), and **Buffer B-imid,** identical to Buffer B but containing 400 mM imidazole. If a construct with a cysteine was present, both buffers contained 1 mM neutralized TCEP (Thermo). BME contains a thiol, which interferes with the future step of coupling the palmitate. The

beads were washed with 20 mL buffer B, then 20 mL of 90% Buffer B, 10% Buffer B-imid. Finally, the protein was eluted with 20 mL Buffer B-imid**,** and collected in two mL fractions. After the elution, fractions corresponding with the peak of the protein were incubated overnight with nutation and ULP1 (1 mM TCEP was added if apoIFITM3 was being purified), and analyzed the following day by SDS-PAGE. After cleavage of the SUMO domain was confirmed, the appropriate fractions were collected and mixed, and 2 mL fractions were snap frozen in a dry-ice ethanol bath. *Note: Reducing agents such as TCEP or DTT are necessary for ULP1 activity.* If the sample did not require alkylation with maleimide-palmitate (i.e. apoIFITM3), then the SUMO domain was separated from the native IFITM3 by size exclusion chromatography (SEC) in Buffer B (10/300 GL, AKTA). In our hands, the SUMO domain consistently elutes after the IFITM3, making size exclusion a useful method to both remove background proteins as well as the enrichment tag.

2.2. Generation of proteoliposome through the rapid dilution method. (Dr. Percher's work)

Modified from Weber et al. [191]. All chloroform solutions were stored in appropriate borosilicate glass with PTFE lined caps (VWR). Phosphatidylcholine and phosphatidylethanolamine suspended in chloroform were purchased from Avanti Lipids. 10 mg cholesterol (Sigma) was resuspended in 1 mL HPLC grade chloroform (Sigma), for a final concentration of 25.88 mM. GD1a (Sigma) was resuspended in a 1:2 methanol:chloroform solution, for a final concentration of 0.544 mM (MW 1882).

For a final total concentration of 1 mM lipid (cholesterol included), appropriate volumes of each lipid were added to a 13 x 100 mm glass vial, and dried under a gentle argon stream (a clear reside is observable from the bottom of the vial).

The sample was then placed under vacuum for at least 2 hours. The dried lipid was resuspended in 1/4 the final total volume by adding Buffer A containing 1% OG, followed by horizontal shaking (gentle agitation can also be used). Higher resuspension concentrations will result in an opaque solution. The resuspended lipid was then aliquoted to other glass vials according to the number of conditions planned. After the addition of protein (the volume of protein + lipid cannot exceed 1/3 final volume), the lipid-protein solutions were left at RT for several minutes, Afterwards, the solution was rapidly diluted. by pressing the glass vial down with one hand on a table top vortex machine turned to high, and using the other hand to add 2-3x the volume of the solution, buffer A *without* detergent (depending on starting volume). This dilutes the OG below the CMC of 0.5% (final 0.25 – 0.3 %), driving the formation of liposomes.

To dialyze out the remainder detergent, the entire liposome solution was added to pre-primed Slide-A-Lyzer MINI Dialysis wells (Thermo, 10k MWCO). Different sized wells were used depending on the volume of the solution (0.5 mL wells for 4-500 µL volumes, 3 mL wells for 1-2 mL volumes). The wells were then shaken horizontally at RT for 1 hr, followed by a buffer exchange and dialysis with horizontal shaking for 6 hr at 4 °C. Finally, an additional buffer exchange was done, and incubated overnight at 4 °C with horizontal shaking. The next day, the samples were transferred to Eppendorf tubes with a pipette, and used for the described assays. Samples were kept for a maximum 1 week at 4 °C.

2.3. Surface preparation

Glass microscope coverslips (25 mm × 25 mm; No. 1.5) from VWR were cleaned in piranha solution (45 mL 50% hydrogen peroxide and 105 mL 70% sulfuric acid) for 10 min, then rinsed 30 min with deionized water with a minimum resistance of 18.2

MΩ cm (Siemens Purelab Ultra water purification system). Glass slides were flushed by deionized water again and dried by a stream of ultra-pure nitrogen gas prior to plasma cleaning.

2.4. Microfluidic device fabrication

Microfluidic device fabrication procedure for hemifusion experiments was described in the previous chapters.

5.2.5. Virus membrane labeling and purification

Influenza A virus (A/Puerto R8/1934/H1N1)(PR8) was purchased from Charles River. 5 μL PR8 was added into 250 μL PBS buffer, and 0.5 μL of 0.1 mg/mL octadecyl rhodamine B (R18) was added into the virus solution. The solution then was sonicated gently in a water bath for 55 minutes. The free R18, which did not insert into the viral membrane, was removed from labeled virus using a G-25 spin column for two minutes at 3000 rpm. The supernatant containing the purified viruses was diluted with 750 μL PBS buffer before use.

2.6. Single-virion hemifusion assay

The procedure of performing single-virion hemifusion assay was described in the previous chapters. The only difference is the temperature was maintained at 32 °C during the assay.

3. Result & discussion

3.1. Using SPT to test the impact of IFITM3 on PR8 hemifusion kinetics

When optimizing the technique for H1N1 (PR8), we found that it is not easy to obtain hemifusion events at room temperature (22 °C), but our control case, influenza H3N2 (X-31) can fuse at room temperature under the same bilayer and environmental conditions. Moreover, Tsurudome et al. found that the function of fusion peptide of PR8 is affected by temperature, but the function of fusion peptide of X-31 is

temperature independent[192]. Hence, we characterized the hemifusion behavior of H1N1 (PR8) at pH 4.5 and 32 °C (**fig. 28**). For preliminary testing, we chose 1:5000 and 1:20,000 protein to lipid molecule dilution because we want to understand the impact of protein concentration on the antiviral activity. We found that PR8 virus binding numbers are not significantly different when bound to GD1a liposomes with reconstituted IFITM3 or VAMP or when bound to GD1a control liposomes. However, we found that the presence of IFITM3 or VAMP drastically decreases the fusion extent of PR8 by 2/3 when compared to GD1a control liposomes. Furthermore, after plotting the hemifusion kinetics, it is shown that the presence of VAMP does not affect the rate of hemifusion, whereas the presence of IFITM3 proteoliposomes slows down the hemifusion rate at pH 4.5. To fully understand the IFITM3 inhibitory mechanism, we will need to obtain more hemifusion events to ensure the results are statistically significant and to test more acidic pH values because it may be possible that IFITM3 exhibits different function or activity at different pH values.

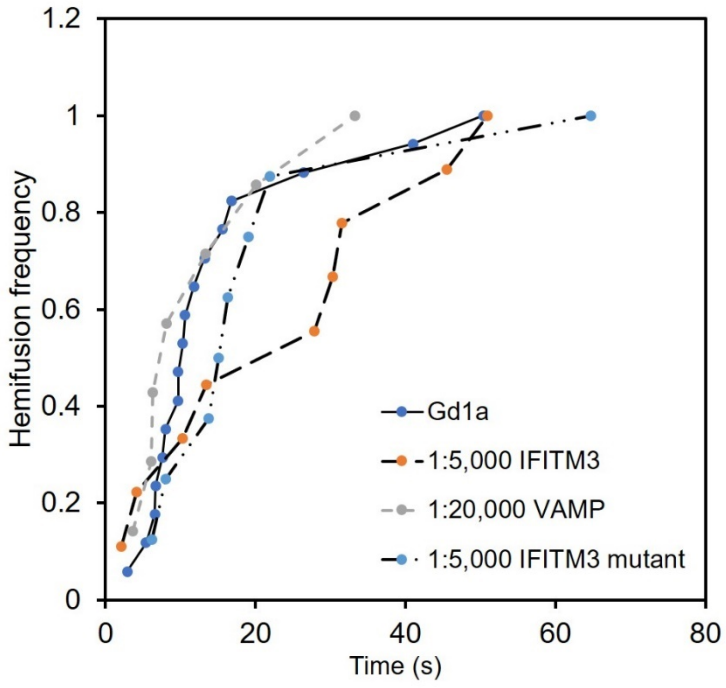

Figure 28. Hemifusion kinetics of H1N1 (PR8) to various proteoliposomes with

GD1a receptor.

The observation in SPT technique can explain the findings in bulk fusion done by Dr. Percher [181]. Moreover, SPT data suggests that the decrease of fusion extent from utilizing IFITM3 proteoliposomes may be because the hemifusion kinetics is impeded, when compared to using VAMP proteoliposomes.